Structural and Electronic Properties of Organic Molecules on Monolayer Molybdenum Disulfide on Ag(111)

Dr. rer. nat. Asieh Yousofnejad

im Fachbereich Physik
der Freien Universität Berlin
eingereichte Dissertation

Berlin, 2021

Diese Arbeit entstand in der Arbeitsgruppe von Prof. Dr. Katharina J. Franke am Fachbereich Physik der Freien Universität Berlin.

A scientist in his laboratory is not a mere technician: he is also a child confronting natural phenomena that impress him as though they were fairy tales.

— *Marie Curie (1934-1986)*

Abstract

Molecular charge transfer complexes are an interesting class of materials due to their promising applications in molecular electronic devices. Understanding the charge transfer between donor and acceptor molecules at the nanoscale is crucial for the ongoing development and optimization of those devices. In this thesis, we investigate charge-transfer processes within prototype mixed molecular systems on the single-layer molybdenum disulfide (SL-MoS$_2$) on Ag(111). The characterization of molecules on SL-MoS$_2$ is motivated by the fact that SL-MoS$_2$ electronically decouples molecules from the metal substrate and enables us to resolve the electronic properties (vibronic states and charge transfer processes) of an almost isolated molecule. Spectroscopic measurements of SL-MoS$_2$ on Ag(111) reveal the semiconducting bandgap. We also observe a moiré pattern due to the lattice mismatch between SL-MoS$_2$ and Ag(111). The decoupling properties of MoS$_2$/Ag(111) are challenged for tetracyanoquinodimethane (TCNQ) molecules. Deposition of TCNQ molecules on MoS$_2$/Ag(111) results in the formation of self-organized molecular islands. STS measurements reveal that the lowest unoccupied molecular orbital (LUMO) is significantly narrower than on a metal substrate. The LUMO is accompanied by additional characteristic spectroscopic features which are identified as vibronic states with strong electron-phonon coupling using Franck-Condon picture.

After investigating the electron acceptor TCNQ, an electron donor counterpart tetrathiafulvalene (TTF) is added to the system. The deposition of both TTF and TCNQ on MoS$_2$/Ag(111) leads to the formation of a mixed monolayer. Local STS measurements show electronic modifications in the mixed structure. The onset of conductance is closer to the Fermi level compared to the pure molecular islands. The modification is attributed to a charge-transfer process between TTF and TCNQ. Additionally, one can charge/discharge the molecules by gating them with the STM tip. Subsequently, we characterize another kind of charge transfer complex consisting of dicyanovinyl-quinquethiophenes (DCV5T-Me$_2$) and C$_{60}$. Deposition of DCV5T-Me$_2$ leads to the formation of two types of islands with different packing densities. Spectroscopic measurements within the more densely packed island reveal a smaller HOMO-LUMO gap due to the stronger screening effect. Screening effects lead to a smaller HOMO-LUMO gap for C$_{60}$ molecule surrounded by other molecules. Depositing both molecules on MoS$_2$ still leads to homo-molecular islands. At the interface, some C$_{60}$ molecules locate on DCV5T-Me$_2$ molecules. For those C$_{60}$, a modified electronic structure indicates an influence of the underlying DCV5T-Me$_2$ molecule with partial charge transfer or screening effect.

Kurzfassung

Molekulare Ladungs-Transfer-Komplexe sind eine interessante Klasse von Materialien aufgrund ihrer Anwendungsmöglichkeiten in molekularen elektrischen Bauteilen. Ausschlaggebend für die Weiterentwicklung dieser Bauteile ist das Verständnis der zugrunde liegenden Ladungs-Transfer-Prozesse auf der Nanoskala. In dieser Arbeit untersuchen wir den Ladungsaustausch zwischen zwei Prototyp-Molekülen auf einer Molybdän-Disulfid (MoS_2) Monolage (ML) auf Silber(111). Die Charakterisierung der Moleküle auf ML-MoS_2 erfolgt aufgrund der guten elektronischen Entkopplung der Moleküle vom Metallsubstrat. Dies hat zur Folge, dass die elektronischen Zustände (z. B. Ladungsaustausch oder vibronische Übergänge) der Moleküle nahezu denen isolierter Moleküle entsprechen. Wir charakterisieren zunächst die von uns gewachsene MoS_2-Schicht auf Ag(111): Sie weist eine Bandlücke und ein Moire-Muster auf, das durch leichte Unterschiede zwischen den Gitterkonstanten von MoS_2 und Ag hervorgerufen wird. Die Entkopplungeigenschaften des MoS_2 betrachten wir zuerst für Tetracyanoquinodimethan (TCNQ). Die Moleküle bilden durch Selbstorganisation Inseln und wir beobachten, dass das niedrigste unbesetzte Molekülorbital (LUMO) wesentlich schärfer erscheint als auf einem Metallsubstrat. STS Messungen zeigen, dass neben dem LUMO weitere Resonanzen auftreten. Mithilfe des Franck-Condon-Prinzips können wir diese als vibronische Zustände mit starker Elektron-Phonon-Wechselwirkung identifizieren. Zusätzlich zum Elektronenakzeptor TCNQ untersuchen wir den Elektronendonor Tetrathiafulvalen (TTF). Gleichzeitiges Aufdampfen der beiden Moleküle führt zur Ausbildung von gemischten Inseln, was sich in einer Modifikation der elektronischen Struktur widerspiegelt. Die Bandlücke ist kleiner und näher am Fermilevel als für die separaten Molekülinseln. Die Veränderung interpretieren wir als Ladungsaustausch zwischen TTF und TCNQ. Darüber hinaus können die Moleküle durch die Spitze des STM geladen und entladen werden. Zusätzlich haben wir ein weiteres Beispiel für Ladungs-Transfer-Komplexe untersucht, bestehend aus Dicyanovinyl-Quinquethiophen (DCV5T-Me_2) und C_{60}. Hierbei zeigt das DCV5T-Me_2 zwei verschiedene Inselarten mit unterschiedlicher Packungsdichte. Durch eine stärkere Ladungsabschirmung in der dichteren Packung zeigt diese eine kleinere HOMO-LUMO Energielücke. Ähnliches ist beobachtbar bei C_{60}, wo wir die höchste Ladungsabschirmung für Moleküle feststellen, die von sechs weiteren C_{60} Molekülen umgeben sind. Die gemeinsame Deponierung von DCV5T-Me_2 und C_{60} führt nicht zu gemischten Inseln, sondern zu homogenen Inseln, wobei sich teils C_{60} Moleküle auf den DCV5T-Me_2 Inseln anlagern. Diese C_{60} zeigen eine modifizierte elektronische Struktur, die auf einen Einfluss der zugrundeliegenden DCV5T-Me_2 Moleküle hindeuten, mit partiellem Ladungstransfer oder Abschirmungseffekten.

Acronyms

Au	Gold
Ag	Silver
CB	Conduction band
CBM	Conduction band minimum
DCV5T-Me$_2$	dicyanovinyl-quinquethiophenes
DFT	Density functional theory
DoS	Density of states
FWHM	Full width half maximum
Hcp	Hexagonal closed-packed
HOMO	Highest occupied molecular orbital
LUMO	Lowest unoccupied molecular orbital
Mo	Molybdenum
S	Sulfur
SOMO	Singly occupied molecular orbital
STM	Scanning tunneling microscopy/microscope
STS	Scanning tunneling spectroscopy
SUMO	Singly unoccupied molecular orbital
TCNQ	7,7,8,8-tetracyanoquinodimethane
TTF	tetrathiafulvalene
TMDC	Transition metal dichalcogenide
UHV	Ultra high vacuum
VB	Valence band
VBM	Valence band maximum

Contents

CHAPTER 1

Introduction

More than 50 years ago, Gordon Moore predicted that the number of transistors on a microchip doubles every two years [1]. Ever since, scientists were motivated to "miniaturize" electronic devices and search for technological structure to reach even smaller scales. One alternative approach to conventional Si-based technologies is molecular electronics. In 1974, Aviram and Ratner proposed an electronic device, a rectifier, based on utilizing an organic single molecule [2]. Since then a lot of effort has been done to use organic molecules in electronic devices. Over the years, organic electronic devices such as organic light-emitting diodes (OLEDs) [3, 4], organic solar cells (OSCs) [5, 6] and organic thin film transistors [7, 8] have been developed. Organic electronic devices have some advantages compared to inorganic semiconductors such as easy processing, high flexibility and low-cost fabrication [9]. However, the maximum efficiency of organic solar cells (12 %) is still much lower than the efficiency of inorganic solar cells, e.g. GaAs thin film solar cells (29 %) [10].

The motivation to study single molecules is that they are "building blocks" of any molecular-sized electronic device. Therefore, it is crucial to understand the fundamentals of the interaction of single molecules with their environment (substrate and neighbors) and the influence of this interaction on electronic and structural properties of molecules. Beyond characterizing single molecules' properties, the interaction between molecules in the form of charge transfer (CT) has attracted attention due to their prospective applications in molecular electronics [11, 12]. The charge transfer between the donor and the acceptor molecules in molecular charge transfer complexes (CTCs) gives rise to new electronic features which are different from those of the parent compounds. Another important aspect is to understand vibrational phenomena of single molecules in molecular assemblies. The vibration induces energy dissipation to the system that subsequently reduces the lifetime of the electronic devices and their stability [13–15].

Scanning tunnelling microscopy (STM) is a versatile and powerful tool to study molecules on surfaces. It is capable of investigating atomic-scale structures in real space, in particular to study single molecule junctions [16, 17], to measure vibrational states of single molecules [18, 19] or to manipulate single molecules [20, 21]. STM also allows to study the charge transfer (CT) interaction between molecules. One

drawback of STM is the necessity of using a conducting substrate which subsequently affects the electronic properties of the adsorbates. Adsorbing molecules on metal surfaces obscures their intrinsic electronic states due to hybridization, charge transfer and screening, which broaden and shift the molecular resonances [22–26]. The charge transfer between electron donor and acceptor are also modified by the interaction with the underlying metal surface. To reduce the influence of the substrate, the electronic properties of the adsorbates is needed to be electronically separated from the metal surface. For that, an isolating or semiconducting layer is employed to facilitate investigating CT processes. These decoupling layers not only make investigating CT possible, they also enable to study vibronic states which we presented in this work as well.

A wide range of thin layer materials have been used as a spacer between the adsorbate and the metal surface. Decoupling layers such as graphene [27, 28], MgO [29, 30] and hBN [31, 32] have been presented over the years. A few breakthroughs have been achieved by using decoupling layers. A NaCl layer have employed to image the molecular orbital of pentacene molecules by Repp *et al.* [33] . The vibronic states of copper phthalocyanine molecules have been observed using an Al_2O_3 layer by Qiu *et al.* [18]. More recently, Krane *et al.* [19] introduced single-layer molybdenum disulfide (SL-MoS_2) on Au(111), a member of the transition metal dichalcogenide (TMDC) family, as a decoupling layer. The SL-MoS_2 has advantages over other candidates, such as having three-atomic layers and being non-ionic. With that system, Krane *et al.* obtained a quite remarkable energy resolution for the vibronic signature of 2,5-bis(3-dodecylthiophen-2-yl)thieno[3,2-b]thiophene (BTTT) molecules, which enables to distinguish between different rotamers (isomer with different bound rotation) of the molecule.

In this work, a low-temperature scanning tunnelling microscope (STM) was used to study different molecular adsorbates on SL-MoS_2/Ag(111) with high resolution.

This thesis is structured as follows :
In **chapter 2**, an introduction is given to scanning tunnelling microscopy and the theoretical background underlying the methods used in this work is briefly described. The details of the experimental setup are provided, also sample and tip preparation procedures used in our experiments are described.
In **chapter 3**, we focus on the physics of molecular adsorbates and how their properties are influenced by the environment. The interaction between molecule and substrate as well as the interaction between molecule and their neighbours in the assembly are considered. We also explain the charge transfer process in the donor-acceptor molecular assemblies and explain how the voltage drop in the DBTJ gives rise to charging the adsorbate. In our work, double barrier tunnelling junction (DBTJ) consists of the vacuum barrier and the decoupling layer (SL-MoS_2). Eventually, we explain the Franck-Condon model which we use to simulate dI/dV spectra and investigate the vibronic states of different molecules on MoS_2/Ag(111).

In **chapter 4**, we introduce the general structural and electronic properties of MoS_2. In **chapter 5**, we report the growth of $SL-MoS_2$ on Ag(111). We study its structural and electronic properties by means of scanning tunnelling microscopy and spectroscopy. For a $SL-MoS_2$ on Ag(111) we observe a moiré pattern. The electronic properties on different moiré sites are investigated by STS. Furthermore, $SL-MoS_2$ is suggested as an effective decoupling layer on Ag(111).

In **chapter 6**, we investigate 7,7,8,8-tetracyanoquinodimethane (TCNQ) molecules on $MoS_2/Ag(111)$. We show that the electronic coupling with the metal surface is significantly suppressed by the decoupling properties of $SL-MoS_2$. TCNQ molecules show a vibronic fingerprint within the MoS_2 band gap, which was found in good agreement with DFT calculations based on the Franck-Condon model.

In **chapter 7**, we investigate charge transfer (CT) in the mixed structure of tetrathiafulvalene (TTF) and TCNQ molecules. First, we investigate the electronic properties of TTF molecules in pure TTF islands. Next, we deposit both molecules on $MoS_2/Ag(111)$ and obtain the charge transfer complex (CTC). In the mixed structure we find modified electronic features that were not seen neither on the pure TTF nor on the pure TCNQ molecular assemblies. Two different charge transfer mechanisms are considered in order to explain the particularity of the TTF-TCNQ electronic structure.

In **chapter 8**, we divide the experiment into three parts. We examine the structural and electronic properties of methyl-substituted dicyanovinyl- quinquethiophenes ($DCV5T-Me_2$) and C_{60} molecular islands on $MoS_2/Ag(111)$. $DCV5T-Me_2$ form two types of molecular island on MoS_2. We compare the two types of molecular islands structurally and electronically. The electronic properties of the islands are measured with STS and compared to the isolated molecules to inspect the influence of intermolecular interactions via screening effects on the molecular states. We investigate the adsorption, assembly and the electronic properties of C_{60} on MoS_2. Finally, we study the electronic features at a $DCV5T-Me_2/C_{60}$ interface.

In **chapter 9**, we summarize the results presented in this thesis.

Theoretical and Experimental Background

The Scanning Tunnelling Microscope (STM) was introduced for the first time in 1981 by Binning and Rohrer as a new way to study surfaces with atomic resolution in real space and, more importantly, the local electronic properties [34, 35]. One year after its invention, Binning and Rohrer solved one of the most intriguing problems in surface science. They reported the first *real space* image of a Si(111)-7×7 surface [36]. This striking innovation granted them the physics Nobel prize in 1986, which was shared with Ernst Ruska who designed the first electron microscope. As a versatile tool, STM evolved over time into other techniques such as spin-polarized STM (SPSTM) [37], STM induced light emission [38] and vibrational spectroscopy [39]. STM is also capable of manipulating single atoms and molecules in order to create and investigate artificial structures [40, 41].

In this chapter, the working principle of the STM followed by the theoretical background of the tunnelling process will be introduced. Additionally, conductance spectroscopy will be explained which allows us to probe the local density of states (LDOS) of the sample. In the last part, the experimental set up and sample preparation will be presented.

2.1 Working Principle of STM

The working principle of STM is based on the quantum mechanical tunnelling effect, in which a particle can tunnel through a (classically forbidden) potential barrier. Fig. 2.1 depicts a schematic set up of an STM. A voltage is applied between the sharp metal tip and the conducting sample. A (tunnelling) current can be detected when the tip approaches the sample sufficiently close. Classically, current cannot flow between tip and sample if the potential barrier of the vacuum gap is larger than the energy of the electrons. However, in the quantum mechanical picture particles have a certain probability to cross the potential barrier (quantum tunnelling effect). Fig. 2.2a shows the energy diagram of the system of tip-vacuum-sample and Fig. 2.2b shows the one-dimensional wave function for a rectangular potential barrier. The
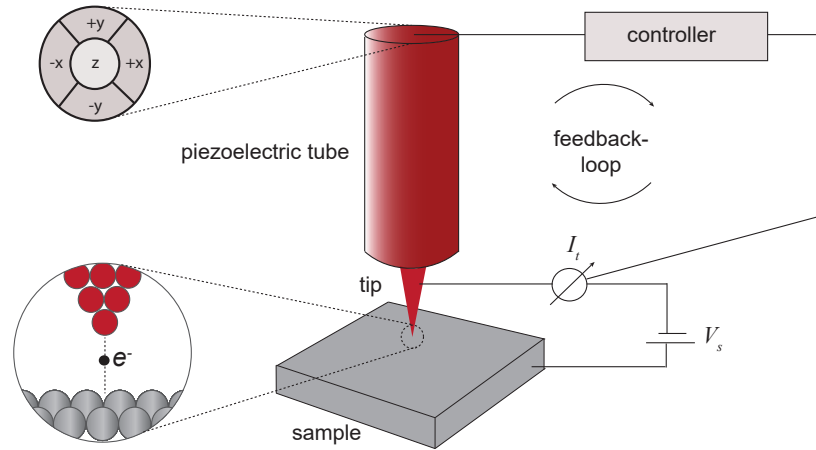
Figure 2.1: Working mechanism of the STM. A sharp metallic tip is brought close to the sample, by applying a bias voltage between them a current flows between tip and sample. The movement of the tip is controlled in xy as well as z direction by means of a piezoelement. The inset shows the close-up tunnelling junction in the STM. The feedback-loop controls the tip-sample distance to keep the current constant.

tunnelling current depends exponentially on the tip-sample distance and is typically in the range of pA to nA. For a rectangular barrier the tunnelling current (for small voltages and temperatures) is given by [42]:

$$I_t \propto exp(-2\kappa d); \kappa = \sqrt{\frac{2m\phi}{\hbar^2}}, \tag{2.1}$$

where d is the barrier width (tip-sample distance), κ is the decay constant, m the mass of the electron and ϕ the effective local work function $\phi=1/2(\phi_s+\phi_t)$, ϕ_s and ϕ_t are the work functions of the sample and the tip, respectively.

The origin of the formula will be elaborated in detail in the following section. When the tip-sample distance is increased by one Å the tunnelling current is reduced by one order of magnitude. The remarkable resolution achievable with STM is based on this strong dependence of the tunnelling current on the tip-sample separation.

When the tip scans over the sample surface line by line, the topographic STM image is recorded. A piezoelectric tube is attached to the tip and acts as an actuator to control the tip-surface distance. When a bias voltage is applied to the sample, the tunnelling current flows through the junction. Due to the small tunnelling currents in STM, an I-V converter is an essential element to amplify and convert it to a voltage that can be measured more precisely. A feedback mechanism also constantly controls the tip height by approaching or retracting the tip from the surface to keep the current constant.

In order to acquire topographic images of a surface, STM can operate in two modes, visualized in Fig. 2.3. In **constant-current mode** (see Fig. 2.3a) the tunnelling
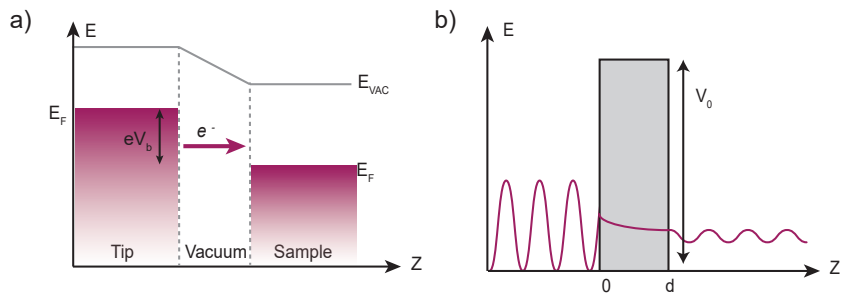
Figure 2.2: **a)** Schematic energy diagram of the tip-vacuum-sample tunnelling junction. The voltage (V_b) is applied to the sample and enables electrons to tunnel from tip to sample in the energy range between E_F and E_F+eV_b. **b)** Real part of the particle wave function in one dimension, for a rectangular tunnelling barrier of width d and height V_0. The particle is traveling from left to right.

current is kept constant while the tip height is adjusted by the aforementioned feedback loop. The recorded image consists of the feedback signal as a function of the lateral position and reflects the convolution of topography of the surface and LDOS. When the tip laterally approaches an edge at the surface the tunnelling current increases due to the reduction of the tip-surface distance. Consequently, the feedback loop retracts the tip to maintain the constant tunnelling current.

Alternatively in the **constant-height mode** (see Fig. 2.3) the tip scans the surface at a constant height (the feedback is switched off) while recording the current. The
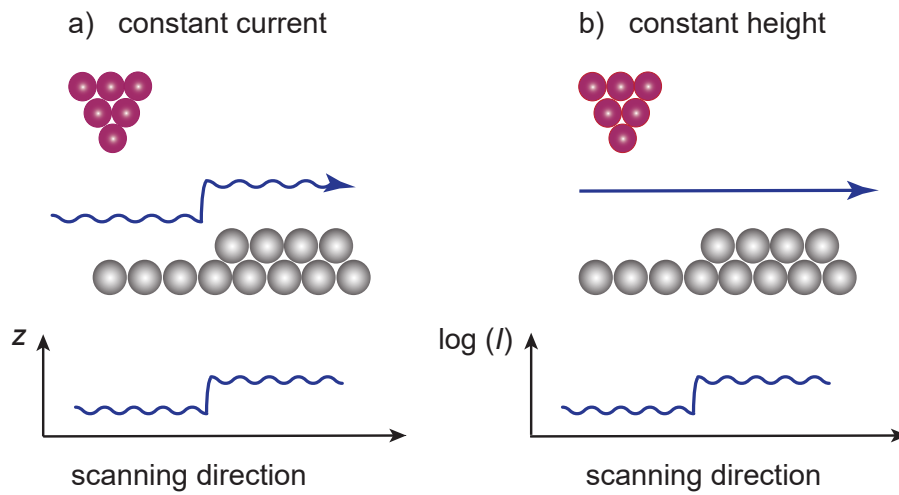

Figure 2.3: Schematic illustration of constant-height and constant-current topography modes, where the apparent height and the tunnelling current are recorded, respectively.

Figure 2.4: In the Tersoff-
Hamann approximation, the
STM tip is modeled as locally
spherical with a radius R cen-
tered at r_0. The separation
surface S (within the vacuum
barrier) is indicated by the red
dashed line [44].
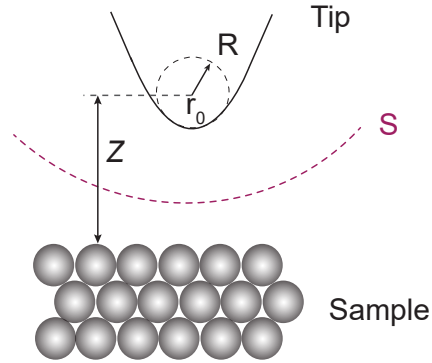
recorded image reflects the changes in the tunnelling current.

As the feedback loop is disabled in the constant-height mode, this mode is only used when the scanning area is sufficiently flat and the conditions are stable. For instance, small thermal drift or piezo creep can cause the tip to go out of tunnelling contact or into contact with the surface. Accordingly, the constant-current mode is the preferred operation mode because it provides safer operation of the STM as it avoids unintentional tip-surface contact.

2.2 Theory of Tunnelling Current in STM

In 1961 and prior to the invention of the STM, the theory of tunnelling current was published by Bardeen [43]. His theory, which was based on a metal-insulator-metal junction, was used by Tersoff and Hamann in 1983 to describe the tunnelling process in an STM [44]. In their model the STM tip is considered as a spherical s-wave with the radius R, centered at a position r_0 with a distance z from the surface. Fig. 2.4 illustrates the corresponding model.

The tunnelling current in first-order perturbation theory is given by [44]:

$$I_t(V) = \frac{2\pi e}{\hbar} \sum_{\mu,\nu} f(E_\mu)[1 - f(E_\nu + eV)]|M_{\mu\nu}|^2 \delta(E_\mu - E_\nu), \qquad (2.2)$$

where $f(E_\mu)$ and $f(E_\nu)$ are the Fermi functions of the tip and sample, V is the applied bias voltage and $M_{\mu\nu}$ is the tunnelling matrix element which describes the probability of transmission between the tip eigenstate (ψ_μ) and the sample eigenstate (ψ_ν) with $E_{\mu,\nu}$ the corresponding energies. Assuming small voltages and low temperatures, equation (2.2) gives us:

$$I_t(V) = \frac{2\pi e^2 V}{\hbar} \sum_{\mu,\nu} |M_{\mu\nu}|^2 \delta(E_\nu - E_F)\delta(E_\mu - E_F), \qquad (2.3)$$

Figure 2.5: Schematic energy diagram of the WKB approximation potential. For positive sample bias voltages, tunnelling occurs from tip to sample. ϕ_t and ϕ_s are the work function of tip and sample, respectively. The trapezoidal barrier shape is approximated by a rectangle of height ϕ+eV/2, with ϕ=1/2(ϕ_s+ϕ_t).
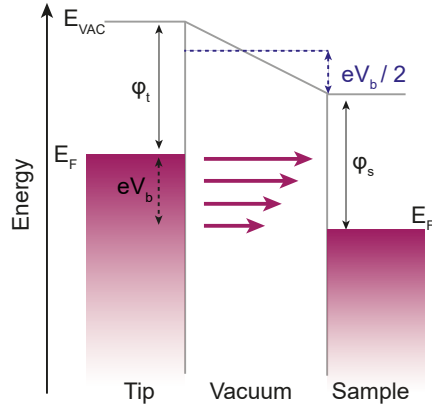
where E_F is the Fermi level and $M_{\mu\nu}$ is expressed by Bardeen's theory as [43]:

$$M_{\mu\nu} = -\frac{\hbar^2}{2m_e} \int d\vec{S}.(\psi_\mu^* \nabla \psi_\nu - \psi_\nu \nabla \psi_\mu^*). \qquad (2.4)$$

The quantity in the parentheses is the current operator and the integral is taken over the surface $(\vec{S})$ which is entirely within the vacuum barrier (see Fig. 2.4). To evaluate the matrix element $M_{\mu\nu}$, we consider the spherical s-wave tip from the Tersoff-Hamann approximation and the semiclassical Wentzel-Kramers-Brillouin (WKB) approximation which considers a general shape of the potential barrier. In the simplified case, a trapezoidal shape of the barrier is approximated by a rectangle of height ϕ+eV/2 (see Fig. 2.5) and we obtain:

$$|M_{\mu\nu}|^2 \propto \exp\left[-2z\sqrt{\frac{2m_e}{\hbar^2}}\sqrt{\phi - E + eV/2}\right], \qquad (2.5)$$

where ϕ is the average work function of the tip and the sample. This equation shows the striking feature of the tunnelling current which is its exponential dependence on the tip-surface distance. The schematic energy window in the STM junction is depicted in Fig. 2.6. For small bias voltages and temperatures the tunnelling current will be:

$$I_t(V) = \frac{2\pi e}{\hbar} \int_{E_F}^{E_F+eV} dE \rho_t(E - eV)\rho_s(E)|M_{\mu\nu}|^2, \qquad (2.6)$$

where ρ_t and ρ_s stand for the tip and surface density of states, respectively. Equation 2.6 indicates the relation of tunnelling current to the tip and surface DOS and also indicates the dependence on the energy window defined by the bias voltage. If we consider the first approximation in which ρ_t is constant, the tunnelling current is proportional to the density of states of the surface.

9

2.3 Scanning Tunnelling Spectroscopy (STS)

We have explained in the previous part that the tunnelling current contains information about the DOS of the surface. Therefore, scanning tunnelling spectroscopy is a powerful method to study the electronic properties of the surface or adsorbates on the surface by directly measuring the energy dependence of the LDOS [45]. One can record the differential tunnelling conductance dI/dV by measuring the tunnelling current when the bias voltage is ramped at a fixed tip height.

The derivation of the tunnelling current (Eq. 2.6) with respect to the bias voltage yields:

$$
\begin{aligned}
\frac{dI}{dV} &\propto \rho_t(E_F)\rho_s(E_F + eV)|M_{\mu\nu}|^2 \\
&+ \int_0^{eV} dE\rho_t(E - eV)\rho_s(E)\frac{d|M_{\mu\nu}|^2}{dV} \\
&+ \int_0^{eV} dE\rho_t(E)\frac{d\rho}{dE}|M_{\mu\nu}|^2,
\end{aligned}
\tag{2.7}
$$

We have considered a simple approximation where the tip density of state is voltage independent. Additionally, we assume a small bias voltage in which the tunnelling matrix element (transmission coefficient) is constant. We obtain:

$$
\frac{dI}{dV} \propto \rho_s(E_F + eV).
\tag{2.8}
$$

Therefore, by measuring the dI/dV we will get information of the density of state of the surface.

2.3.1 Lock-in Amplifier

We obtain the dI/dV signal by using the lock-in amplifier method. A lock-in amplifier adds a sinusoidal voltage ($V_{mod}\sin(\omega t)$) to the DC voltage bias. This sinusoidal voltage has a few millivolts amplitude and a frequency of some hundreds of Hertz. This will subsequently modulate the tunnelling current as:

$$
I(V + V_{mod}\sin(\omega t)) \propto \int_0^{e(V + V_{mod}\sin(\omega t))} \rho_s(E)dE,
\tag{2.9}
$$

which for small V_{mod} can be written in the form of a Taylor expansion:

$$
I(V + V_{mod}\sin(\omega t)) \propto I(V) + \frac{dI}{dV}V_{mod}\sin(\omega t) + \frac{d^2I}{dV^2}V_{mod}^2\sin^2(\omega t) + \mathcal{O}(V_{mod}^3), \tag{2.10}
$$

The first term is referred as the zero-order component and is proportional to the tunnelling current. The second term is proportional to the differential conductance
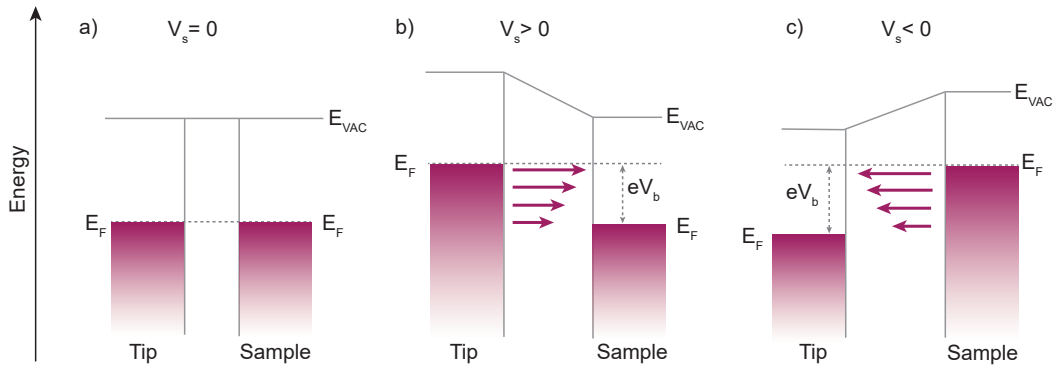
Figure 2.6: Schematic energy diagram of STM junctions. **a)** No bias voltage is applied hence the Fermi level of tip and sample are aligned. **b)** At positive sample bias electrons tunnel from the tip into unoccupied states of the sample. **c)** Oppositely, at negative sample bias electrons tunnel from occupied states of the sample into the tip. The length of the arrows represents the higher tunnelling probability of the electrons with higher energies.

and hence to the LDOS. Therefore, by mixing the input signal with a reference signal, we can filter and extract the signal with the frequency ω which is proportional to the dI/dV and so the LDOS. As this method filters out the majority of the frequencies (except around ω), we obtain a better signal-to-noise ratio than by taking the numerical derivative of the current.

The described technique provides access to another spectroscopic mode called **dI/dV map**. This map is acquired when the STM tip scans the area of interest while the dI/dV signal from the lock-in amplifier is recorded. In contrast to the topographic image where all states between E_F and E_F+V contribute, dI/dV maps only depict the DOS of the scanned region at a certain energy [46].

In the following chapters, we visualize frontier molecular orbitals via dI/dV maps. We compare the experimental dI/dV maps with the simulated frontier molecular orbitals. All simulations presented in this thesis are obtained by DFT calculations for the molecule in gas phase, using GAUSSIAN09 package with the B3PW91 functional and the 6-31g(d,p) basis set [47]. Using DFT, we calculate the molecule's wave function and the distribution of the squared tunnelling matrix element ($|M_{\mu\nu}|^2$, following eq. 2.4) along the planar molecule. The tip wave function (s-wave) is defined by a spherical function $\propto (\kappa |\vec{r}\text{-}\vec{r_0}|)^{-1} \exp(\text{-}\kappa |\vec{r}\text{-}\vec{r_0}|)$ [44] with decay constant $\kappa=\sqrt{2m\phi}/\hbar$. The overlap of the tip and molecule wave functions depends on the tip height z, which is the distance between the center of the s-wave tip and the center of the flat-lying molecule.

2.4 Experimental Setup

2.4.1 Preparation and STM Chambers

In this thesis all the measurements are carried out with a CreaTec STM based on a design by Gerhard Meyer [20]. The experimental system consists of two UHV chambers; a preparation chamber and a measurement (STM) chamber which are separated by a gate valve. To avoid undesirable contamination, all preparations and measurements are done in the UHV chambers.

To maintain the low pressure condition of $\sim 10^{-10}$ mbar in the preparation chamber several pumps including two ion pumps, a turbomolecular pump, a titanium-sublimation pump (TSP) and a cryo pump (cold trap) are mounted to the chamber. The preparation chamber is also equipped with additional tools like a mass-spectrometer, a sputter gun and slots to mount molecular or metal UHV evaporators.

A movable manipulator transfers the sample between two chambers. The manipulator is able to move in three directions (x,y,z) independently and rotate around its axis. In order to anneal the sample, the manipulator is equipped with thermo-couples and heating filaments. It can also be pre-cooled with liquid helium to transfer the sample into the STM chamber. The preparation process of the samples will be explained in the following section.

The STM chamber includes of the STM scanning head which is in contact with a liquid helium bath at an equilibrium temperature of 4.2 K. In order to reach and maintain low temperature, two cylindrical shields surround the measuring stage and
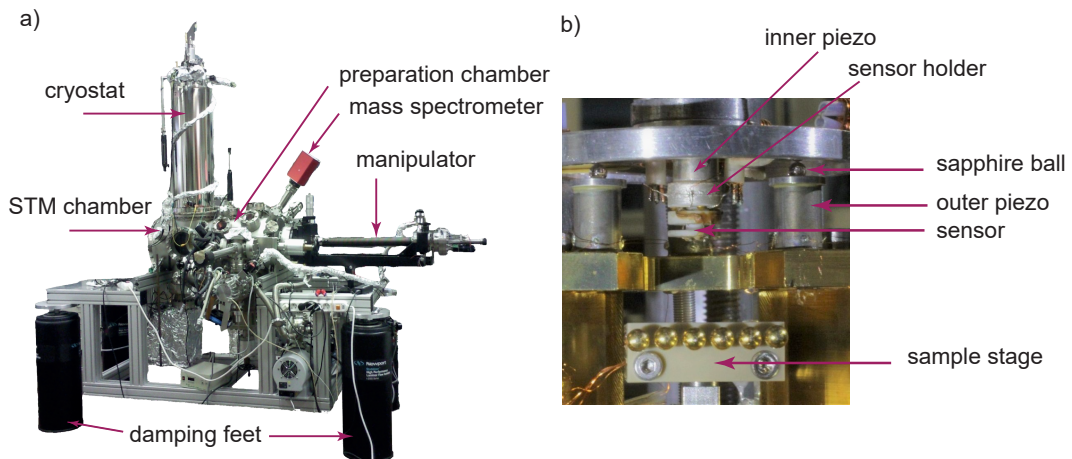

Figure 2.7: **a)** Image of the STM which consists of two UHV chambers: preparation and STM chamber, cryostat all on four air dumpers. **b)** Photo of the Besocke-type STM head. Three outer piezos with sapphire balls are connected to the copper ramp. The inner piezo at the center holds the sensor a sample stage holds the sample. The pictures are adapted and modified from [48].
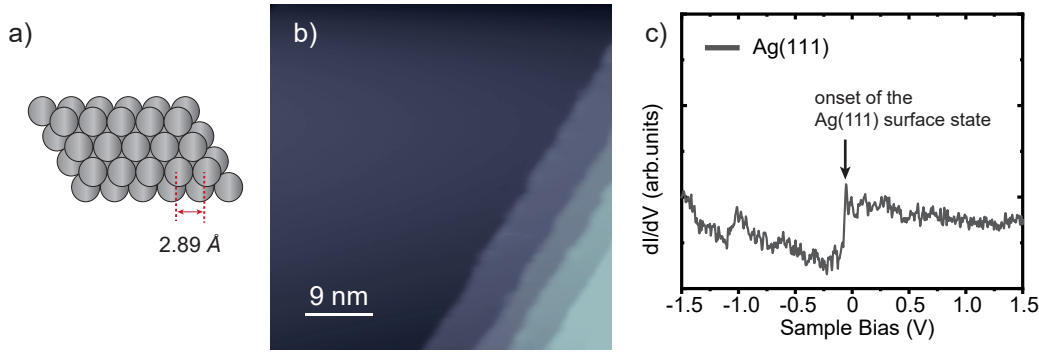
Figure 2.8: **a)** Schematic representation of the fcc Ag(111) surface with 2.89 Å neighbouring atom distance. **b)** STM image of clean Ag(111) showing several terraces and a large flat terrace, the image is recorded at 1V and 25 pA. **c)** dI/dV spectrum acquired with open feedback (set point: I = 100 pA and V = 2.5 V, V_{mod}=10mV) on a bare Ag(111) surface, showing the onset of the Ag(111) surface state at -60 mV.

the cryostat, the outer one provides 70 K shielding and the inner one provides 5 K shielding with liquid nitrogen and helium, respectively.

2.4.2 STM Head

The head of the STM is designed by Karl Besocke (so-called beetle design) and developed by Gerhard Meyer and Sven Zöphel at FU Berlin [49, 50]. This design has high mechanical and thermal stability and works in the temperature range of 4.5 K to 300 K. As shown in Fig. 2.7b, the STM head consists of a base plate where the sample stage is mounted. Three outer piezo in contact with spherical sapphires hold the three-fold copper ramp. By applying saw tooth-shaped voltage pulses to the electrodes of the piezo elements, the ramp moves laterally and rotationally which leads to the change of the tip position in vertical as well as horizontal direction. The maximum lift height is 0.6 mm. In the center of the ramp the scanner piezo holds the scanning sensor and the tip. One disadvantage of the beetle design is the slightly coupled movement in z and xy. When the ramp is moving down in z direction to approach the sample there will be a slight unintentional shift in the xy direction and vise versa. Another disadvantage is the lack of a fixed reference frame in xy because of the rotation of the ramp.

In order to damp low frequency vibrations, four pneumatic feet are used to lift the whole chamber during measurement (see Fig. 2.7a). Moreover, an eddy-current damping system is implemented by springs on which the STM head is hanging.

The data was analyzed using the following softwares: SpectraFox[51], WSxM [52], OriginPro and Igorpro.

Figure 2.9: Schematic tungsten tip etching in NaOH. The etching process occurs near the surface of NaOH [55].
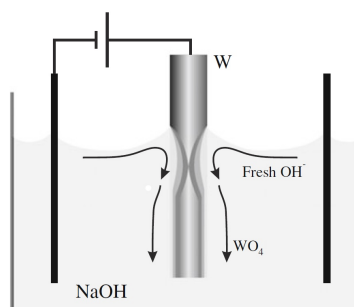
2.5 Sample and Tip Preparation

To investigate single molecules or self-assembled molecular islands we need an atomically clean substrate. In this thesis we exploit Ag as a substrate which is polished in the (111) direction. Ag(111) is a weak interacting substrate and can form flat and large terraces. The silver lattice crystallizes in face centered cubic (fcc) with a lattice parameter of 4.085 Å [53]. Therefore, the neighbouring distance in the close-packed (111)-plane will be 2.89 Å as illustrated in Fig. 2.8a. An STM image of the Ag surface in Fig. 2.8b shows several terraces as well as a large and flat surface. To clean the surface, repeated cycles of sputtering and annealing are performed. For sputtering, the noble gas Ne is ionized and accelerated toward the sample (with an energy of 1 kV for 20 min at 10^{-5} mbar). Subsequently the sample is annealed at 800 K for a few minutes to obtain larger terraces. The preparation of an atomically clean sample is adapted from Musket *et al.* [54]. Following the cleaning procedure, single-layer MoS_2 is grown on the Ag surface (the details will be explained in chapter 5). Afterwards, different molecules (adsorbates) are evaporated on the clean sample. The sample is pre-cooled before transferring into the STM chamber. The detailed preparation of each system will be explained in their corresponding chapters.

2.5.1 Tip Preparation

The preparation of the tip defines the resolution and the quality of the STM images. We chemically etched a tungsten (W) tip in a sodium hydroxide (NaOH) solution in order to obtain a microscopically sharp tip apex. Fig. 2.9 illustrates the etching process.

Another preparation technique can be applied during the measurement to regain the metallic tip after a contamination. The tip is indented into the clean surface for by few Ångstroms while a few volts are applied. The quality of the tip can be examined by STS measurements on the clean surface. The dI/dV spectrum on bare Ag(111) in Fig. 2.8c reveals a surface state at $\sim$ -60 mV [56, 57]. This processes can be repeated until the desired tip obtain.

Molecules on Surfaces

STM is a powerful tool to study molecular adsorbates on surfaces. Numerous STM studies have been carried out, investigating various molecular properties such as electronic, optoelectronic [58, 59] and magnetic properties [37, 60], as well as molecular vibrations [61, 62] and charge transfer [22, 63]. As mentioned in the introduction chapter, while using single atoms and molecules as "building blocks" of electronic devices is a long-term goal, STM studies are of great importance to characterize theses "building blocks". One important aspect is how the molecular properties are modified upon adsorption on a surface.

In this chapter, I present the basics about the particular properties of molecules adsorbed on surfaces that are essential to understand and interpret the experimental results that will be presented later on.

3.1 Molecular Energy Levels on Surface

It was mentioned in the previous chapter that the working principle of the STM is based on a conducting substrate. Metal surfaces are known to modify the electronic properties of the molecules due to screening and hybridization effects which lead to energy-level shifting and energy-level broadening, respectively.

Depending on the nature of the molecule and the substrate, their interaction is categorized into two types: physisorption and chemisorption. The adsorption types are distinguished by their the adsorption energy. In the physisorption, molecules are bound to the surface by weak van der Waals forces, whereas in chemisorption, molecules are covalently bound to the surface. The modification of the electronic features due to hybridization is much weaker for physisorption compared to chemisorption.

During the tunnelling process in STS measurements, the adsorbate becomes transiently charged either positively or negatively depending on the polarity of the bias voltage. Thus, the observed states are not of the neutral molecule, but the cationic and anionic states. The energy of these states are related to the electron affinity (EA) and ionization potential (IP), and are also referred to as negative ion resonance (NIR) or positive ion resonance (PIR) in tunnelling spectroscopy. Due to the additional
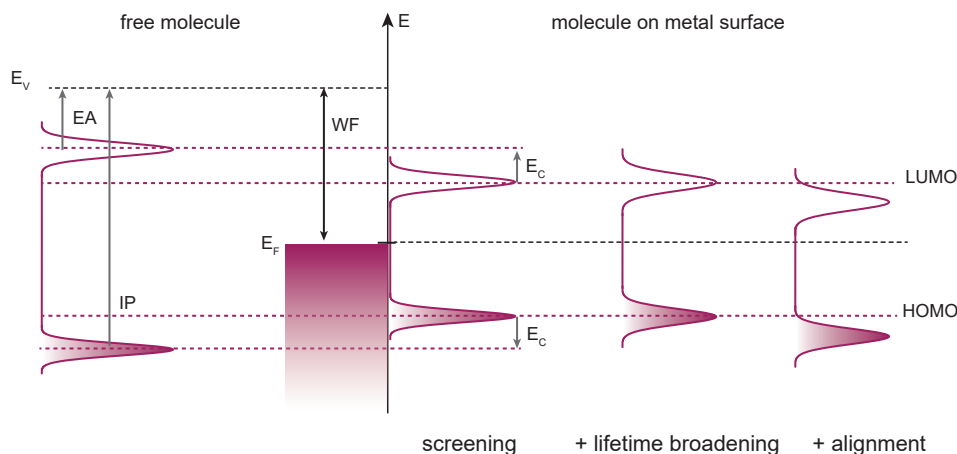
Figure 3.1: Schematics of shifting and lifetime broadening of the molecular levels upon adsorption on a metal surface. In the gas phase (left), the molecule shows energetically discrete and localized peaks at the energetic positions of the electron affinity (EA) and ionization potential (IP). When the molecule is brought on the metal surface the Coulomb energy (Ec) is reduced as a consequence of the screening effect. Thus the charge states shift toward the Fermi level (close to LUMO and HOMO). Another effect is the energy level broadening due to the shorter lifetime of the electronic states when coupled strongly to the metal surface. The right end panel shows the energy level alignment due to the charge transfer between molecule and the surface. This causes a rigid shift of the molecular level with respect to the Fermi level.

charging energy, STS probes the states at larger energies than the highest occupied molecular orbital (HOMO) and the lowest unoccupied molecular orbital (LUMO).

Screening reduces the IP-EA gap, when the molecule is brought into contact with a metal substrate. The charge of the molecule at the interface creates an image charge in the surface. The interaction between the positively or negatively charged molecule and the negative or positive image charge in the surface increases the EA and reduces the IP [64, 65]. In other words, the Coulomb repulsion energy (Ec) is reduced and molecular resonances shift closer to the Fermi level as depicted in Fig. 3.1.

Another screening mechanism arises due to the polarizability of the neighbouring molecules in a self-assembled molecular island. The charge carriers in the neighbourhood screen the added or removed charge, which decreases the Coulomb repulsion even more [66].

Moreover, due to the charge transfer (CT) between the molecule and the surface, the energy levels of the molecule realign (shift) with respect to the Fermi level of the surface as sketched in Fig. 3.1 (right panel) where the HOMO-LUMO gap shifts.

3.2 Decoupling Layers and Energy Broadening

In contrast to the free molecule, when the molecule is deposited on a metal surface, the tunnelling electron quickly leaves the molecular state into the metal within the timescale of femtoseconds. This results in a lifetime broadening up to hundreds of millielectronvolts (meV) of the molecular states.

As a consequence of this broadening, the intrinsic electronic properties (fine electronic structures within the energy scale of few meV to hundreds meV) are obscured and cannot be detected in tunnelling spectroscopy. To reduce this effect a thin decoupling layer between molecule and metal substrate is introduced. This additional layer between the adsorbate and the surface acts as a second tunnelling barrier, which reduces the overlap between molecular orbitals and the substrate's metallic states and thus hybridization and lifetime broadening. Having a certain thickness, a decoupling layer also provides an adequate large vertical distance between the adsorbate and the substrate.

Vibrational excitations are usually hidden in the broad resonances and cannot be detected when a molecule is deposited on a metal surface. Using different types of decoupling layers the vibronic states of several molecules were observed in former works [18, 27, 28, 33, 67–70]. However, to study vibronic properties of molecules, the different decoupling layers are not equivalent. For example, it was reported for STS studies of molecules on NaCl decoupling layer, that the strong electron-phonon coupling within the ionic lattice upon electronic excitation of the molecule provokes an energetic broadening of the molecular resonances [71]. This should be considered when ionic lattices such as NaCl and Al_2O_3 are acting as a decoupling layer. Molybdenum disulfide is suggested as a promising non-ionic decoupling layer. In the following chapter we will investigate its structural and electronic properties.

3.3 Double Barrier Tunneling Junction and Charging Effect

In this thesis, we investigate the intrinsic electronic properties of adsorbates. We have explained in the previous section that a non-conducting spacer inserted between adsorbate and metal surface may act as decoupling layer. Such a decoupling layer behaves as a second tunnelling barrier for the STM junction, which is thus called a double-barrier tunnelling junction (DBTJ). In this junction the applied voltage drops between tip and molecule and also between molecule and metal substrate. The ratio of the voltage drop (α) between tip and molecule to the voltage drop between molecule and metal depends on the double barrier capacitance and changes with the tip-surface (vertical) distance. Therefore, the voltage drop is divided between the two tunnelling barriers and molecular energy levels are not fixed and can shift with respect to the Fermi levels of the tip and sample depending on the applied bias voltage.
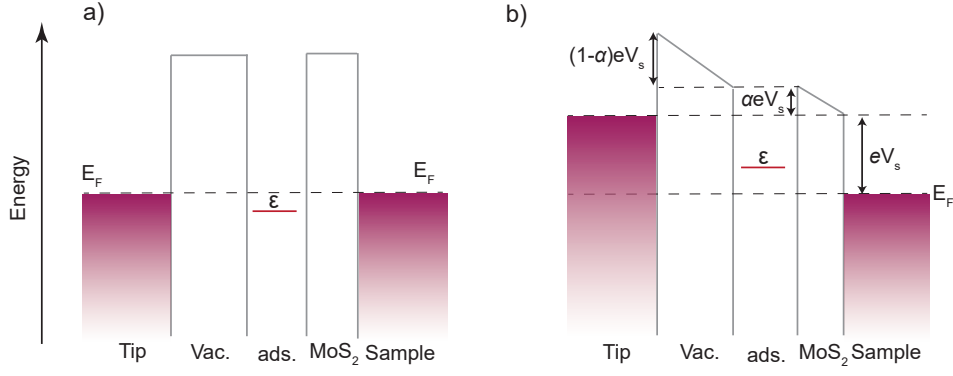
Figure 3.2: **a)** Energy level diagram at zero bias where the Fermi levels of sample and tip are aligned. The adsorbate electronic state is shown as ϵ. **b)** At higher bias, the voltage drop across MoS$_2$ and vacuum barriers are displayed as αV_s and $(1-\alpha)V_s$. At positive sample bias, when the tip's Fermi level shifts up, molecular state (ϵ) is also pulled up with respect to the Fermi level of the surface.

One important consequence is that a molecular level can cross the Fermi level of the sample and thereby changing the charge state of the molecule (charging effect) [63, 72].

When the bias voltage is zero the Fermi levels of tip and sample are aligned as depicted in Fig. 3.2a. Here, ϵ is the molecular state in the unbiased junction with respect to the Fermi levels of the tip and surface. By applying a bias voltage V$_s$, the voltage drop is divided between vacuum and the decoupling layer (see Fig. 3.2b). αV_s corresponds to the voltage drop across the decoupling layer and an empty molecular state. Tunnelling through the molecular state (ϵ) occurs when:

$$|V_s| = |\frac{\epsilon}{e(\alpha - 1)}| \tag{3.1}$$

When the molecular level is pulled across the Fermi level of the substrate, the molecule is charged. We consider the molecular state filled and charging occurs at:

$$V_s = \frac{\epsilon}{e\alpha}. \tag{3.2}$$

Generally, charging of a molecule occurs when two requirements are met. First having a double barrier tunnelling junction and second a molecular state near the Fermi level as in Fig. 3.2. In this case (see Fig. 3.2b), the tip Fermi energy is shifted up with respect to the molecular resonance (ϵ) by an applied positive bias. Consequently, the molecular resonance shifts with respect to the sample states due to the small barrier between molecule and sample. Subsequently, the electron in state ϵ is transferred to the sample. This event is observed as a sharp resonance in the dI/dV spectrum (so-called *charging peak*).
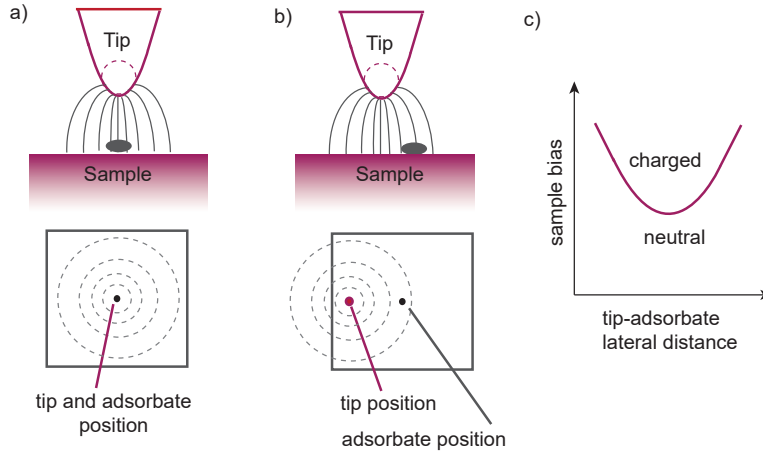
Figure 3.3: Electric field induced by the bias in the STM junction. **a)** The tip is located above the adsorbate and the electric field lines are shown as perpendicular lines to the surface (top panel). From top view, the field lines are shown as rings centered at the projected position of the tip (lower panel). **b)** As the tip is moved laterally away from the adsorbate, the position of the resonance in dI/dV shifts to higher energies. In other words, this shift has a parabolic dispersion with the lateral position of the tip. **c)** In a constant height line above the adsorbate, when the bias sweeps the dispersion of the tip field at the adsorbats appear in parabolic. As the tip moves laterally away from the adsorbate for a given electric field more bias is needed to apply.

The charging events can also be detected in constant-height dI/dV maps as a *charging ring* [72–74] and in constant-height dI/dV line spectra as a *parabola* [63, 75, 76]. The observation of the charging rings or parabolas is due to an inhomogeneous electric field in the junction. To explain the origin of these effects, we sketch this *tip-induced effect* in Fig. 3.3. Considering the inhomogeneous junction, the iso-contours of the electric field at the surface appear as circles. When the tip is placed above the adsorbate as in Fig. 3.3a (top panel), the field is strongest at the adsorbate. When the tip moves away (Fig. 3.3b) from the projected tip location, the field is weaker (smaller) at the adsorbate. As the electric field is inversely proportional to the total distance between tip and adsorbate, the adsorbate still can be charged even when the tip is further away from the adsorbate at an adequate bias voltage. This event can be detected as a *ring* in dI/dV map and as a *parabola* in dI/dV line spectroscopy (Fig. 3.3c). We explain charging and the observation of charging peaks and parabolas in chapter 7.

In this thesis (the presented experiments), the value of the voltage drop across the decoupling layer (single-layer MoS_2) is considered $\sim (10\text{-}15)\%$ [19, 77] when the tip is at a distance of typical tunnelling conditions. This value was found first by Krane *at al.* [77] as they identified a shift of the resonances for 2,5-bis(3-dodecylthiophen-2-yl)thieno[3,2-b]thiophene (BTTT) molecule adsorbed on $MoS_2/Au(111)$. We also

obtain the same values in our data in chapter 7 when we observe charging in the mixed structure of tetrathiafulvalene (TTF) and 7,7,8,8-tetracyanoquinodimethane (TCNQ) molecules.

3.4 Charge Transfer Complexes

Charge transfer complexes in organic materials have attracted attention due to the various potential applications in organic electronics [11, 12], storage devices [78, 79] and organic photovoltaic cells [80, 81].

Charge transfer complexes (CTC) are generally based on the interaction between an electron donor (D) and an electron acceptor (A) species. The donor molecule with a small ionization potential (IP) interacts with an acceptor counterpart with a large electron affinity (EA). Thus the donor can be oxidized by the loss of charge and the acceptor is reduced by gaining charge. The reaction for a charge transfer salt is described by [82]:

$$D_m + A_n \rightarrow [D_m]^{+\delta} + [A_n]^{-\delta},$$ (3.3)
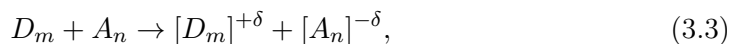
with m and n as integers and δ as the charge-transfer ratio. This reaction requires the condition

$$\Delta E = IP - EA - C < 0.$$ (3.4)

where C contains of the Coulomb, polarization, and exchange energy [83]. The IP of the donor provides the energy needed to remove an electron from the HOMO and the EA of the acceptor describes the energy obtained in filling the LUMO.

In chapter 7, we investigate a charge-transfer film composed of the electron donor TTF and electron acceptor TCNQ on a single-layer $MoS_2/Ag(111)$.

3.5 Vibronic States

The simultaneous excitation in the electronic and vibrational energy level of a molecule is responsible for a vibronic transition. Vibronic excitations are described by the Franck-Condon model [84, 85] which explains the relative intensities of vibronic transitions by relating the probability of a vibrational transition to the overlap of the vibrational wave functions.

The probability of the transition between a ground state ψ and an excited state ψ' with Hamiltonian H is given by:

$$P = \big| <\psi'|H|\psi> \big|^2.$$ (3.5)

Due to the fact that the electron moves much faster than the nuclei we are allowed to separate the electron and the nuclei motions. The Born-Oppenheimer approximation suggests to consider the total wave functions (ψ) as $\psi_e.\psi_\nu$, where ψ_e is the electron
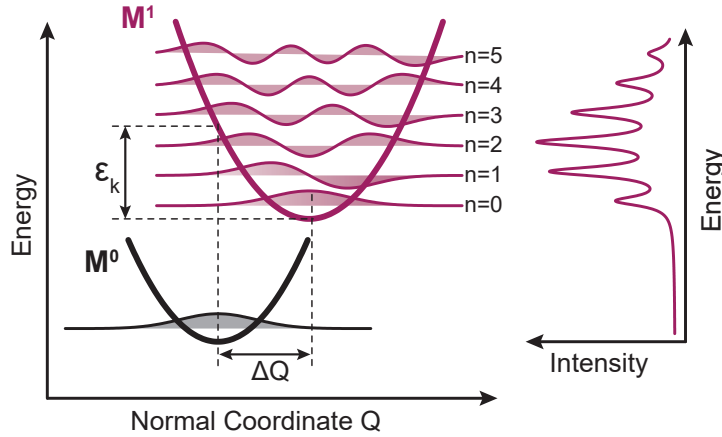
Figure 3.4: Scheme of vibronic excitation in Franck-Condon picture. A neutral molecule (M^0) is shown in its ground state. When adding or removing an electron, the molecule is excited electronically which may couple to vibrational excitations. The Born-Oppenheimer approximation considers the vertical transition between M^0 and M^1. Due to the electronic excitation, the molecule distorts and a shift of the equilibrium position (ΔQ) is displayed in the vibrational normal coordinate. The overlap between the vibrational wave functions of the initial state (gray) and the final state (red) gives rise to the vibronic peaks whose intensities are given by a Poisson distribution sketched in the right panel. Picture taken from [86].

wave function and ψ_ν is a vibrational wave function. In other words, the Born-Oppenheimer approximation does not consider changes in the nuclear coordinates or momentum during the excitation.

$$P = \big| < \psi'_e \psi'_\nu | H | \psi_\nu \psi_e > \big|^2, \tag{3.6}$$

The total Hamiltonian (H) is the sum of electronic Hamiltonian (H_e) and vibrational Hamiltonian (H_ν). Using $H = H_e + H_\nu$, we get:

$$P = \big| < \psi'_e \psi'_\nu | H_e | \psi_\nu \psi_e > \big|^2 + \big| < \psi'_e \psi'_\nu | H_\nu | \psi_\nu \psi_e > \big|^2. \tag{3.7}$$

Because of the orthogonal electron wave function ($< \psi'_e | \psi_e > = 0$), we obtain:

$$P = \big| < \psi'_\nu | \psi_\nu > \big|^2 \big| < \psi'_e | H_e | \psi_e > \big|^2. \tag{3.8}$$

The first term ($< \psi'_\nu | \psi_\nu >$) is called Franck-Condon factor which describes the overlap of the vibrational wave functions of the ground state and excited state and therefore the probability to excite a vibrational state. The second term is the probability to excite the molecule electronically.

The vibronic excitation within the Franck-Condon model is depicted in Fig. 3.4.

M^0 is the neutral molecule in the ground state and M^1 is the charged molecule in the excited state. The higher harmonics of vibrational modes $\hbar\omega_k$ of the excited molecule are also shown. Considering a harmonic oscillator with parabolic potential, the intensities of the nth excited states with vibrational mode k are given by a Poisson distribution [71, 87]:

$$I_{kn} = e^{S_k} \frac{S_k^n}{n!}, \tag{3.9}$$

where S_K is the so-called Huang-Rhys factor of the vibrational mode k as:

$$S_k = \frac{\varepsilon_k}{\hbar\omega}, \tag{3.10}$$

with the energy $(\hbar\omega_k)$ and the relaxation energy ε_k.

In this thesis, we applied the Franck-Condon model to identify and understand the vibronic excitation we observe experimentally in STS. For this purpose, we determine the energy of the vibrational mode as well as the relaxation energy (and the Huang-Rhys factor) that are related to the electronic excitation of a molecule. These parameters are extracted with the following method which has been implemented in previous works [19, 88]. The calculations are carried out by the B3PW91 Functional with the 6-31g(d,p) basis-set implemented in the Gaussian09 code [47].

First, the geometry of the relaxed structure of the neutral state and the charged state of the isolated molecule is calculated with *ab initio* DFT calculation. Comparing those states, we obtain the displacement upon charging (η_α) in mass-weighted coordinates. Then, for each atom (α) the displacement $(l_{\alpha k})$ corresponding to all vibrational modes k for the charged molecule is calculated. There are 3N-6 vibrational modes for a given molecule with N atoms. The relaxation energy for each mode can be determined by:

$$\varepsilon_k = \frac{\omega_k}{2} \left(\sum_\alpha^N \vec{l_{\alpha k}}.\vec{\eta_\alpha} \right)^2. \tag{3.11}$$

When we obtain the Huang-Rhys factors, we can simulate the vibronic spectrum. First, we numerically calculate the convolution (progression) of all vibrational modes. We consider the excitation of all modes due to the coupling of two or more modes and/or the excitation of several harmonics of one vibrational mode. Then, a Lorentzian function with a given half-width-at-half-maximum and the amplitude defined by the Poisson distribution (eq 3.9) is applied to the vibronic spectrum.

In the following chapters, we use the Franck-Condon model and the corresponding calculations to simulate the dI/dV spectra for TCNQ , DCV5T-Me$_2$ and TTF molecules on Sl-MoS$_2$/Ag(111).

Molybdenum Disulfide: Structural and Electronic Properties

The layered transition metal dichalcogenides (TMDCs) are described by the general formula MX_2, where M represents the transition metal (Mo, W, Nb, Ta, Ti, Re) and X stands for the chalcogen (S, Se or Te). The layered structure is formed by three atomic layers covalently bonded, where the transition metal is sandwiched between two chalcogen sheets in the form of X-M-X. In the bulk material, the triple layers are stacked by van der Waals forces similar to graphite. The weakly bound layers make TMDCs appropriate as dry lubricants which have been used for decades.

Due to the weak interlayer interactions, TMDCs are found in several structural polytypes depending on the stacking order of the layers [89]. Fig. 4.1 shows three possible structures of TMDCs and their corresponding unit cells. The numbers and letters are used to label different phases. The number represents the number of the layers to determine the unit cell and the letter defines the chalcogen arrangement, T trigonal, H hexagonal and R rhombohedral. In the 2H phase one layer is rotated by 180° and in 3R the layers are laterally shifted.

Generally, depending on the number of transition metal d-electrons, bulk TMDCs exhibit metallic, half-metallic, semiconducting or superconducting properties [90]. The wide range of electronic properties can be explained by the Wilson and Yoffe model. They suggested that the valence band mainly shows the chalcogen s and p character, while the conduction band arises from the transition metal d states [91]. Thus, the degree of filling of the d orbitals determines whether the TMDC is a metal, semi-metal or semiconductor.

Molybdenum disulfide (MoS_2) is a member of the TMDC family. Like other TMDCs it can be found in 1T, 2H and 3R structure. The 2H phase is more common while the 3R phase is rarely found in nature [92]. Due to the difference in their crystal symmetry, 1T and 2H phases exhibit quite different electronic structures; the 2H phase is a semiconductor while the 1T phase exhibits metallic character. The
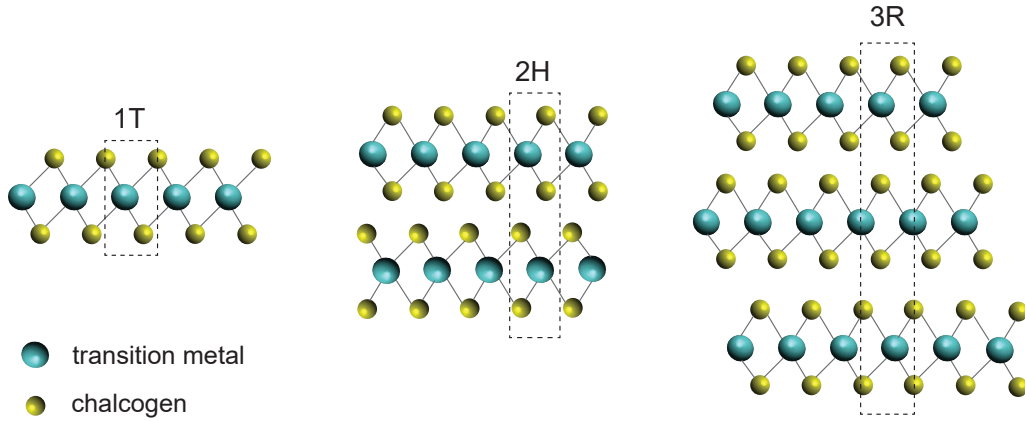
Figure 4.1: Schematic of the three possible stacking configurations of TMDCs and their corresponding unit cells which are shown as rectangular. In 2H phase the layers are rotated with respect to each other and in the 3R phase they are shifted laterally.

electronic structure of bulk $2H$-MoS_2 in Fig. 4.3a shows an indirect band gap of 1.23 eV [93]. The maximum of the valence band is located at the $\bar{\Gamma}$ point and the minimum of the conduction band is located between the $\bar{\Gamma}$ and $\bar{K}$ point. In the following, particularly we focus on single-layer MoS_2, its structural and electronic properties. We show that the band structure for single-layer MoS_2 is different from the bulk due to its 2D nature.

4.1 Single-Layer MoS$_2$: Structure

Single-layer MoS_2 (SL-MoS_2) consists of three atomic layers where molybdenum atoms are sandwiched between two sulfur layers and are bonded covalently [94, 95]. Similar to other single layer TMDCs, SL-MoS_2 is found in two structural types, depending on the position of the chalcogen to the metal element in the X-M-X structure. It can be formed either in 1T (tetragonal symmetry and octahedral coordination) or 1H structures (octahedral hexagonal closed packing and trigonal prismatic coordination) [90, 94]. As shown in Fig. 4.2 in the trigonal prismatic unit cell, sulfur atoms of the upper and lower layer are located on top of each other, whereas in the octahedral unit cell one sulfur layer is rotated by 180° [92]. As we have stated in the previous section, due to the difference in their crystal symmetry these two phases exhibit quite different electronic structure; the 1H phase is semiconducting while the 1T phase is metallic. X-ray diffraction and Raman scattering show octahedral coordination is the metastable structure of single layer MoS_2 [92].
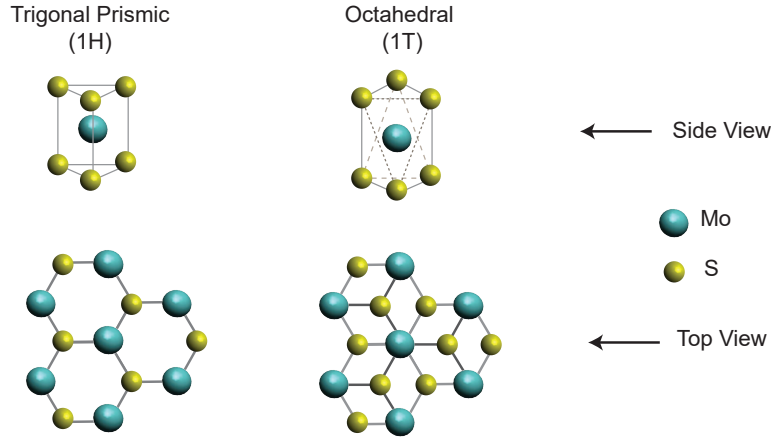
Figure 4.2: Stick and ball model of the single-layer MoS$_2$ unit cell with top view of two phases: trigonal prismic (1H) and octahedral (1T).

4.2 Single-Layer MoS$_2$: Band Structure

The electronic properties of MoS$_2$ depend on the number of layers as depicted in Fig. 4.3a [96, 97]. Decreasing the number of the layers, the indirect band gap increases and SL-MoS$_2$ becomes a direct band gap semiconductor due to quantum confinement [98–100]. The direct band gap of free standing MoS$_2$ has been predicted to be 2.8 eV [101, 102].

Another consequence of the quantum confinement in SL-MoS$_2$ is a high exciton binding energy of $\sim$ 1 eV compared to the bulk MoS$_2$ which is $\sim$ 0.1 eV [101–103]. Therefore, the long exciton lifetime subsequently enhances the luminescence quantum efficiency and makes SL-MoS$_2$ an interesting candidate in photonic devices [99].

In addition, because of the absence of inversion symmetry and a strong spin-orbit interaction, SL-MoS$_2$ exhibits a large spin splitting of the valence band maximum at $\bar{K}$ point (see Fig. 4.3b) by the value of 150 meV [102, 104, 105]. Bana *et al.*[106] experimentally confirmed the spin polarization of the valence band states near the K and -K points of the Brillouin zone for SL-MoS$_2$ on Au(111) surface. The first Brillouin zone is shown in Fig. 4.3c. Hence, the system is promising for spintronic devices with selective access to the spin-orbit split bands at $\bar{K}$ and $-\bar{K}$ by circularly polarized light.

In chapter 3, we have described the application of decoupling layers in STM measurements. There are a wide range of decoupling layers which have been used in STM measurement, such as graphene [27, 28, 108], NaCl [33, 109–111], hexagonal boron nitride (hBN) [67, 112–114] and Al$_2$O$_3$ [115–118]. Although each one has its own advantages and drawbacks, SL-MoS$_2$ is considered a promising candidate in this field. Compared to graphene and hBN, SL-MoS$_2$ with its three atomic layers is
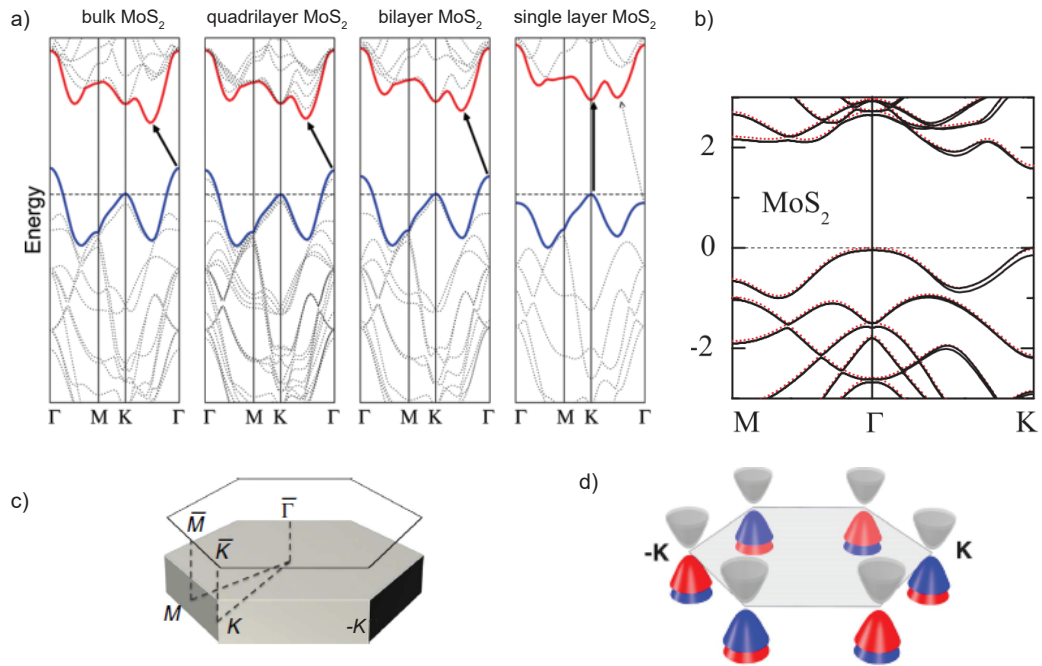
Figure 4.3: **a)** Calculated band structure of bulk, quadrilayer, bilayer and single layer MoS_2. The solid arrows indicate the lowest energy transitions. Bulk MoS_2 is characterized by an indirect band gap. The direct excitonic transitions occur at the K point. With reduced layer thickness, the indirect band gap becomes larger, while the direct excitonic transition barely changes. Hence, single-layer MoS_2 is a direct band gap semiconductor [96], **b)** Electronic band structure calculated for single-layer MoS_2 with (solid line) and without (dotted line) inclusion of the spin-orbit interaction [104], **c)** Corresponding bulk and surface Brillouin zone marked with the high symmetry points [107], **d)** Brillouin zone and schematic band structure for two mirror domain orientations of SL-MoS_2. The colors of the split valence band maximum (blue/red) refer to the different spin orientation of these states [106].

thicker. Hence, in a naive picture the tunnelling barrier induced by a SL-MoS$_2$ should be wider and the decoupling should be more efficient. Nonetheless, this requirement is achieved by Al$_2$O$_3$ and NaCl as their thickness can be tuned. Due to non-ionic character of SL-MoS$_2$ the electron-phonon coupling is less strong compared to the ionic films. This consequently prevents the significant broadening due to the phonon excitation in the decoupling layer [71, 119].

In the following chapter, we explain the growth conditions of SL-MoS$_2$ on Ag(111) surface and we analyze its structural and electronic properties.

Molybdenum Disulfide (MoS$_2$) on Ag(111): Structural and Electronic Properties

The work presented in this chapter was published as:

5.1 Introduction

Besides the interesting property of having a direct band gap explained in the previous chapter, single-layer MoS$_2$ (SL-MoS$_2$) has another fascinating feature. Adsorbing molecules on metal surfaces significantly reduces the life time of the excited state of the molecule due to the hybridization. Semiconducting SL-MoS$_2$ acts as a spacer which decouples molecules from the metal substrate and enables us to observe intrinsic electronic features of molecules [19, 88]. SL-MoS$_2$ on Au(111) has been exploited as a promising decoupling layer [19]. Here, we will explore this potential on Ag(111) surface. Ag(111) is an attractive substrate due to its smaller Schottky barrier height compared to Au(111) in field effect transistor (FET) devices.

In this chapter, I describe the growth and properties of SL-MoS$_2$ on Ag(111).

5.2 Growth of Single-Layer MoS$_2$ on Ag(111)

Single-layer MoS$_2$ can be obtained via various techniques. For instance, single layers can be produced by exfoliation of the corresponding bulk materials. The procedure is similar to graphene exfoliation, because the layers are also held together by weak van der Waals forces. Chemical vapor deposition (CVD) is another approach to synthesize MoS$_2$. To avoid defects, the growth of TMDC layers in ultra-high vacuum (UHV)
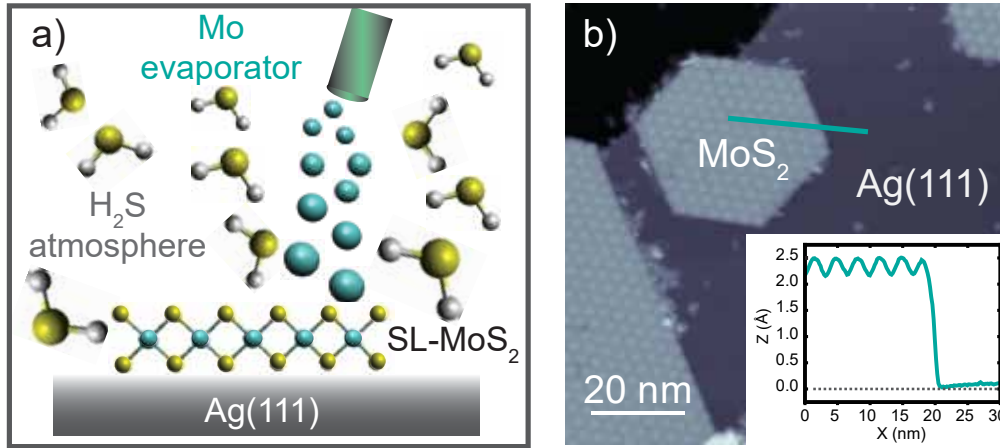
Figure 5.1: **a)** Schematic depiction of growth process of single-layer MoS$_2$ on Ag(111). **b)** STM topography of single layer MoS$_2$ on Ag(111) surface recorded at V = 1.2V, I = 20pA. Inset: Line profile of a single-layer MoS$_2$ island along the green line.

conditions is desirable. The successful growth of several TMDC layers on metal surfaces has been reported earlier [95, 121]. For instance, the growth procedure of MoS$_2$ was reported by S. Helveg, *et al.* [122] using physical vapor deposition (PVD). They synthesized triangular nanoclusters of size 30 Å on Au(111). Then Grøneborg *et al.* [123] changed the temperature and pressure to obtain larger MoS$_2$ islands on Au(111).

In this work, the growth procedure of SL-MoS$_2$ on Ag(111) has been adapted from Grøneborg *et al.* [123]. In order to grow large molecular islands of MoS$_2$/Ag(111) which we will present in the following chapters, we need to grow large MoS$_2$ islands on Ag(111). The Ag(111) surface was cleaned by two cycles of 1-keV-Ne$^+$ sputtering and 500°C annealing under UHV conditions as mentioned in chapter 2.

Following the recipe of Grøneborg *et al.* [123], the synthesis was initiated by back filling the chamber with H$_2$S gas to the pressure of (1×10^{-5}) mbar. The Mo was evaporated for 20 min in the H$_2$S atmosphere (see Fig. 5.1a) while the sample was held at 550°C. The sample subsequently was annealed for 30 min at 550°C in H$_2$S atmosphere and post annealed for 5 min without H$_2$S gas. Afterwards, the sample was cooled down and transferred into the STM chamber. The result of this procedure are small and relatively large high quality MoS$_2$ islands of few hundreds nm large (Fig. 5.1b).
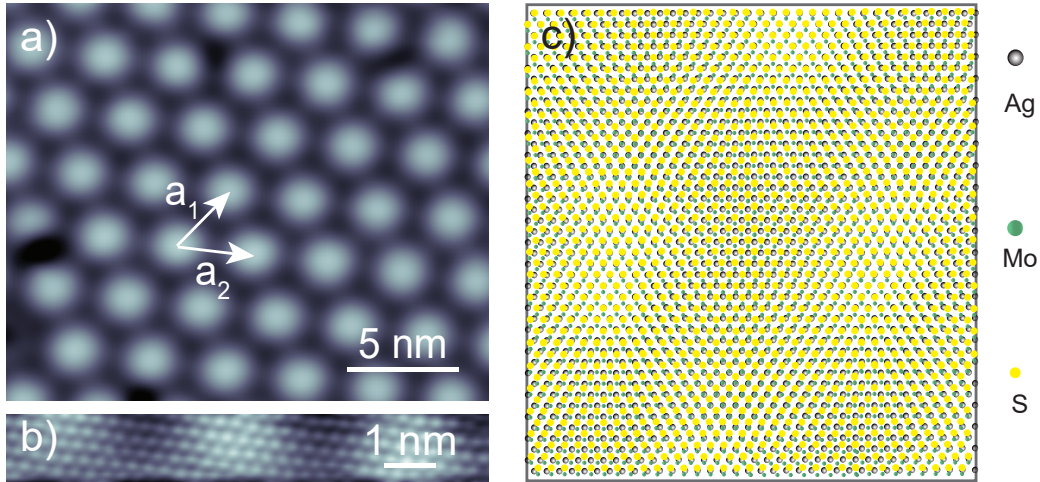
Figure 5.2: **a)** Close-up STM topography view of the moiré superstructure of single-layer MoS$_2$/Ag(111) (V = 1V, I = 20pA). The periodicity of the superstructure is depicted by a_1 and a_2 vectors which $a_1=a_2=(3.3\pm1)$ nm. **b)** Atomically resolved terminating S layer (V = 5mV, I = 1 nA). **c)** A model of single layer MoS$_2$ on Ag(111) showing the lattice mismatch between MoS$_2$ layer and Ag(111) surface.

5.3 MoS$_2$ on Ag(111): Structural Properties

Fig. 5.1a represents the topographic image of Ag(111) surface after growing MoS$_2$ as described in the previous section. MoS$_2$ appears in large islands from tens to hundreds of nanometers. The apparent height of the islands (inset Fig. 5.1a) is (2.3$\pm$0.2)Å which agrees with the result of a single layer of MoS$_2$ on a Au(111) surface [123]. The single layer apparent height is significantly smaller than the layer distance in the bulk structure [124] due to electronic-structure effects. MoS$_2$ islands (Fig. 5.2a) show a hexagonal pattern ascribed to a moiré structure, which arises due to the lattice mismatch between SL-MoS$_2$ and Ag(111) surface as illustrated in Fig. 5.2c. The moiré superstructure appears with the periodicity of (3.3$\pm$0.1) nm on this island. A similar moiré periodicity was also observed for MoS$_2$/Au(111) [95, 123] which can be explained by the comparable lattice constant of Au (4.08Å) and Ag (4.09Å). Investigating about 30 MoS$_2$ islands on Ag(111), we also observe moiré patterns with lattice constants between 3.0 nm to 3.6 nm. The occurrence of different moiré sizes indicates the shallow energetic minima of the lattice orientations. In Fig. 5.2b, atomically resolved STM image depicts the S-S distance of 3.15 Å of the top layer which is in agreement with former works and the expectation of the bulk structure [122, 124, 125].
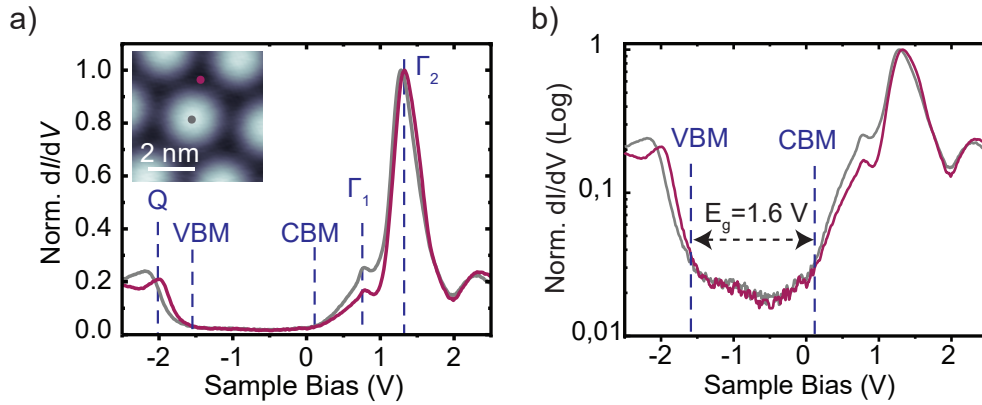
a)

b)

Figure 5.3: **a)** Constant-height dI/dV spectra on MoS$_2$ on Ag(111) surface acquired on top and on hollow region of the moiré structure as shown on the inserted STM topography (feedback opened at V = 2.5 V, I = 0.5 nA, V$_{mod}$ = 10 mV). Dashed lines indicate the conduction band minimum (CBM) at ~ 0.05 V and valence band maximum (VBM) at ~ 1.55 V. The strong features in the dI/dV spectra are associated to the onset of specific bands, which are labeled by Q, Γ_1 and Γ_2 according to their location in the Brillouin zone. The assignment follows Ref.[19]. **b)** Logarithm of dI/dV spectra of **a)** showing the band gap of 1.6 eV.

5.4 MoS$_2$ on Ag(111): Electronic Properties

As mentioned in the previous chapter, MoS$_2$ is exploited as a decoupling layer. It thus needs to provide an electronic band gap. Here we investigate the electronic structure of SL-MoS$_2$ on different locations as the moiré pattern bears a topographic and an electronic modulation [126]. Typical constant-height dI/dV spectra recorded on top and hollow moiré site of MoS$_2$ are displayed in Fig. 5.3a. In the inset of Fig. 5.3a, the local sites are shown as gray and red dots on top and hollow site, respectively. First, I focus on the description of the spectrum on top moiré which shows two pronounced peaks at 0.77 V and 1.28 V and a shoulder at -2 V.

In order to determine the band gap more accurately, the dI/dV spectrum in logarithmic scale is shown in Fig. 5.3b [127–129]. It depicts a gap in the density of states flanked by an onset of conductance at $\sim$ -1.55 eV and $\sim$ 0.05 eV (marked by vertical dashed lines as VBM and CBM, respectively). Hence, the energy difference of 1.6 eV can be associated to the band gap of SL- MoS$_2$ on Ag(111). We note that, the observed band gap is considerably smaller than the calculated value of 2.8 eV for free-standing single-layer MoS$_2$ [101, 102]. This difference indicates a strong hybridization of the electronic states between SL-MoS$_2$ and Ag substrate [105]. Furthermore, we note that the spectral features are similar to those that have been obtained for SL-MoS$_2$ on Au(111) [105, 126, 127].

To compare the spectra, in Fig. 5.4a we plot the spectra on the top sites of the MoS$_2$ moiré on Au(111) and Ag(111). At negative sample bias the onsets of the
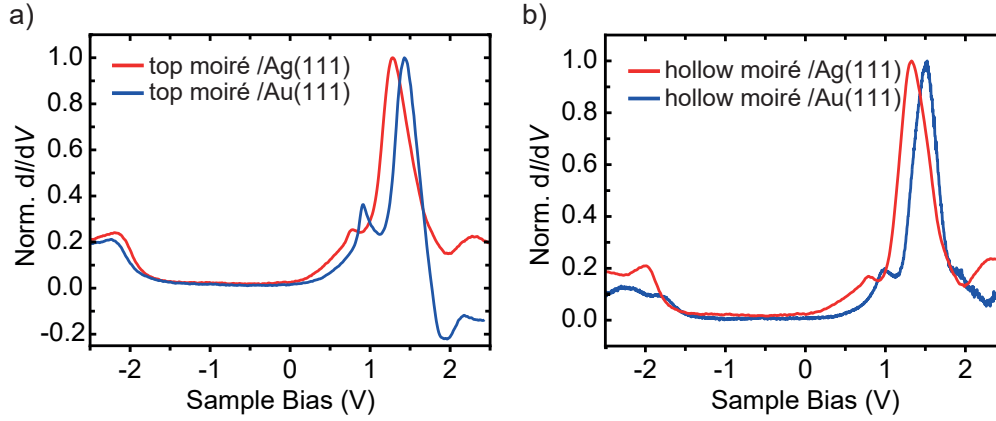
Figure 5.4: constant-height dI/dV spectra acquired **a)** on top and **b)** on hollow site of the moire structure MoS$_2$ on Ag(111) (red curves) and on Au(111)(blue curve). Feedback opened at V = 2.5 V, I = 0.5 nA, V$_{mod}$ = 10 mV (all spectra, except for hollow site on Au(111): V$_{mod}$ = 5 mV).

conductance are the same, whereas at positive sample bias the feature is $\sim$ 140 mV closer to Fermi level on Ag(111) compared to Au(111). Before discussing the difference between SL-MoS$_2$ on Ag(111) and Au(111) in more details, we inspect the electronic properties at the different stacking locations of the interface of MoS$_2$ and Ag. The dI/dV spectra shown in Fig. 5.3a are recorded on top and hollow site of MoS$_2$. The spectrum on the hollow site (Fig. 5.3b) shows a shift of $\sim$ 130 mV toward the Fermi level (E$_F$) at negative bias, while the shift at positive bias is slightly away from the Fermi level by $\sim$ 50 mV. On Au(111), there are also variations between hollow and top sites with the strongest shift at negative bias voltage [126] (see Fig. 5.4). Before elucidating the impact of the substrate and the moiré top or hollow site on the electronic features, we discuss about the origin of the spectroscopic features. As the MoS$_2$ spectrum on Ag(111) resembles the one on Au(111), we can attribute the peaks at 0.77 V and 1.28 V to the bands at the Γ point [126]. Similarly, the shoulder at -2 V could be assigned to the band close to the Q point [126] (in chapter 4, see Fig. 4.3b shows Γ and Q of the first BZ).

It is expected for the CBM to lie at the $\bar{K}$ point for free-standing as well as metal-supported single-layer MoS$_2$ [96, 99, 105, 130]. However, STS is not able to detect states at the $\bar{K}$ point (such as CBM and VBM) of the Brillouin Zone. This failure is due to the large k$_\parallel$ value which results in a large tunnelling decay constant [126, 131]. The tunnelling current depends on the distance according to I(z)$\propto$ exp(-2zκ) where κ is the decay constant. For an electronic state with parallel momentum (k$_\parallel$) and the energy barrier ϕ, the decay constant is $\kappa=(2m\phi/\hbar^2+k_\parallel^2)^{1/2}$. Therefore, the states at the edge of the BZ like VBM and CBM of MoS$_2$ having large k$_\parallel$ values are not detectable at the expected location ($\bar{K}$ point) via constant-height STS.

Now we compare conductance spectra in Fig. 5.4 on different sites on Ag and Au

to explain the influence of the substrate on the electronic features. Spectra on both top and hollow sites of the moiré structure (Fig. 5.4a and b) reveal a rigid shift in the conduction band on Ag compared to Au substrate. The lower work function of Ag(111) (4.50 eV) than Au(111) (5.25 eV) [132] can be a straightforward explanation for the down shift of the unoccupied state on Ag. Using photoemission, Maciej Dendzik *et al.* [133] have observed a down-shift of ~ 280 meV in the valence band structure of WS$_2$ on Ag(111) compared to Au(111).

Angle-resolved measurements further showed that the shift also included band distortions, such that bands at Q were crossing E$_F$ (instead of at K). The band distortion was explained by hybridization of the WS$_2$ bands with the Ag substrate [133]. As explained earlier that our dI/dV signal is not k$_\parallel$-sensitive, we would not be able to detect band distortions in the MoS$_2$–Ag system. However, the clear shift of the states at Γ can be easily understood by hybridization of S-derived states of mainly out-of-plane character with Ag states in analogy to Ref. [105]. In the occupied states, the bands on the hollow site follow the same trend of a down-shift, suggesting that the states near $\bar{Q}$ are equally affected by hybridization with Ag states [133]. In contrast, the tunnelling spectra on the top sites, seem to coincide for Au and Ag substrate. We also note that the tunnelling conductance close to the Γ point is the most sensitive to the precise location on the moiré pattern. Hence, we suggest that this site is most strongly affected by screening effects, which may vary on the different substrates [134] and partially compensate for hybridization effects.

5.5 Conclusion

In this chapter we explained the growth procedure of SL-MoS$_2$ on Ag(111) via PVD method and we obtained fairly large islands of hundreds nm width. STM images revealed the moiré structure of SL-MoS$_2$ on Ag(111) as a consequence of the lattice mismatch between the layer and Ag(111) substrate.

We studied the electronic properties of SL-MoS$_2$ on Ag(111) and observed the band gap of 1.6 eV. As expected the band gap was significantly smaller than the band gap of free-standing MoS$_2$ due to the hybridization of the electronic states with metal substrate. Moreover, the band gap was similar compared to the one on Au(111) with a shift in energy of ~ 140 mV at positive bias while the onset of conductance at negative bias stays the same. To investigate the impact of different stacking at the interface on the electronic features, we recorded dI/dV spectra on top as well as the hollow site of the moiré. At negative bias of the hollow site the spectrum exhibits a shift toward the Fermi level relative to the top site, while at positive bias much smaller shift away from Fermi level is observed.

Decoupling properties of Monolayer MoS$_2$ on Ag(111): Resolving Electronic and Vibronic States of TCNQ

The work presented in this chapter was published as:

Monolayers of MoS$_2$ on Ag(111) as decoupling layers for organic molecules: resolution of electronic and vibronic states of TCNQ, Asieh Yousofnejad, Gaël Reecht, Nils Krane, Christian Lotze and Katharina J. Franke. Beilstein J. Nanotechnol. **2020**, 11, 1062–1071 [120]

The chemical structure of the prototype organic acceptor molecule tetra-cyano-quino-dimethane (TCNQ) is shown in Fig. 6.1a. TCNQ consists of two dicyanomethylene termination groups (C$_3$N$_2$) with a strong electrophilic character [135–137] and a central quinonoid ring that stabilizes the anionic system, because it allows an efficient charge delocalization [138]. The central ring can accommodate up to two electrons upon charge injection which increases its aromaticity and gains energy [138, 139]. As a consequence of this particular chemical structure, TCNQ exhibits a high electron affinity measured between (2.8 ± 0.1) eV by collisional ionization technique [140–142] and (3.383 ± 0.001) eV by means of vibrationally resolved photoelectron spectroscopy [143], the latter value is also obtained via DFT calculation [138]. This prototype electron-acceptor molecule has been extensively investigated by STM on different substrates [26, 144–148]. TCNQ can form charge transfer compounds with both organic and inorganic donors and exhibit a wide range of electrical, optical and magnetic properties [149, 150], particularly in optoelectronic organic devices, including organic light-emitting diodes or field-effect transistors [151]. Because of its strong acceptor character, TCNQ has been exploited as a p-dopant in organic semiconductors.

Here, we use TCNQ molecule as a model system to understand the fundamental aspects of energy level alignment at SL-MoS$_2$-organic interfaces. TCNQ is also implemented here as a test molecule to explore the decoupling properties of SL-MoS$_2$ on Ag(111), whereas it has already been studied on SL-MoS$_2$ on Au(111) [19].

In this chapter, we focus on the adsorption of TCNQ molecules on SL-MoS$_2$ on Ag(111) and we characterize the electronic energy level of the molecule. Due to its electron accepting character, we detect a negative ion resonance within the MoS$_2$ band gap. Tunnelling spectra exhibit a reproducible fine structure which we attribute to the excitation of vibronic states. The decoupling properties of MoS$_2$ reduces the fast relaxation into the metal surface which would otherwise leads to a lifetime broadening [71, 119].

6.1 Structural Properties of TCNQ on MoS$_2$ /Ag(111)

In this work, TCNQ molecules are evaporated on a single layer of MoS$_2$/Ag(111) (preparation is described in chapter 5) while the sample is held at 230K. At this temperature, TCNQ molecules adsorb on both, the MoS$_2$ layer as well as on the Ag surface, but form different arrangements. On Ag(111), the TCNQ molecules form small and disordered islands (Fig. 6.1b) whereas on MoS$_2$ they organize in densely-packed islands like those shown in Fig. 6.1c.

Deposition at lower sample temperature (150K) decreases the molecule diffusion which eventually prevents the formation of well-organized islands (see Fig. 6.1d). Before describing different molecular arrangements, we need to identify individual molecules and their arrangements within an island. Scanning at low bias voltage (0.3 V), the molecules appear as homogeneous elliptical protrusions as depicted in Fig. 2a. Fig. 2b shows the STM image of the same area as in Fig. 2a, scanned with a higher bias voltage (0.8 V). Here, the TCNQ molecules appear as back-to-back double U-shapes separated by a nodal plane at the middle. As we will discuss later and based on the previous works on TCNQ [26, 144, 148, 152], this U shape appearance resembles the spatial distribution of the LUMO resonance of the free molecule. The moiré pattern of SL-MoS$_2$ remains intact (Fig. 6.1c and 2b) and can be seen through the molecular island. This is an indication of the weak interaction between the molecules and the MoS$_2$ layer.

Through closer inspection of the TCNQ islands, we are able to determine the lattice parameters of the molecular self-assembly defined by vectors a_1=(0.9±0.10) nm, a_2=(1.0±0.10) nm and an angle of (96±2)° between them. A simple model that accounts for these lattice parameters is depicted in Fig. 2b. According to this model all TCNQ molecules take the same orientation with respect to each other in a way that each TCNQ molecule has six neighbours. The corresponding superimposed molecular model suggests strong C $\equiv$ N $\cdots$ H - C intermolecular bonding between the cyano endgroups and the hydrogens in the quinone ring of the neighbouring molecule. All H and N atoms are involved in constructing the intermolecular bonds which leads to the organization of molecular islands on the surface. The structure of
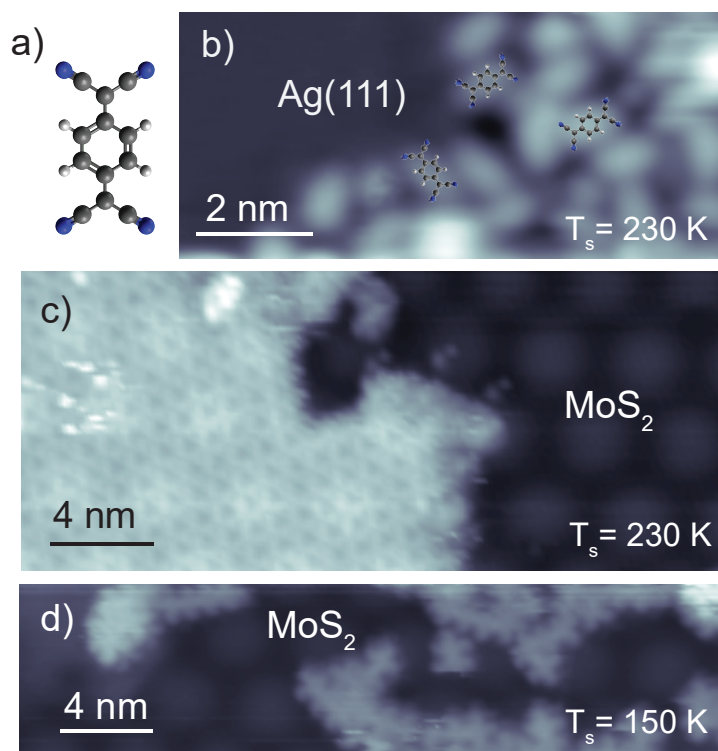
Figure 6.1: STM topography of the surface after depositing TCNQ molecules at a sample temperature of 150 K and 230 K during evaporation. **a)** Stick-and-ball molecular model of TCNQ. Gray spheres represent C atoms white spheres account for H atoms and blue for N atoms. **b)** TCNQ molecular assembly on Ag(111) recorded at V = 1V, I = 200 pA. **c)** STM topography of the closed-packed molecular island on MoS$_2$/Ag (111) recorded at V = 1V, I = 20 pA. **d)** STM topography of TCNQ molecules at sample temperature 150 K during evaporation (recorded at V=1V and I=10 pA), where molecules take random arrangements at lower sample temperature.
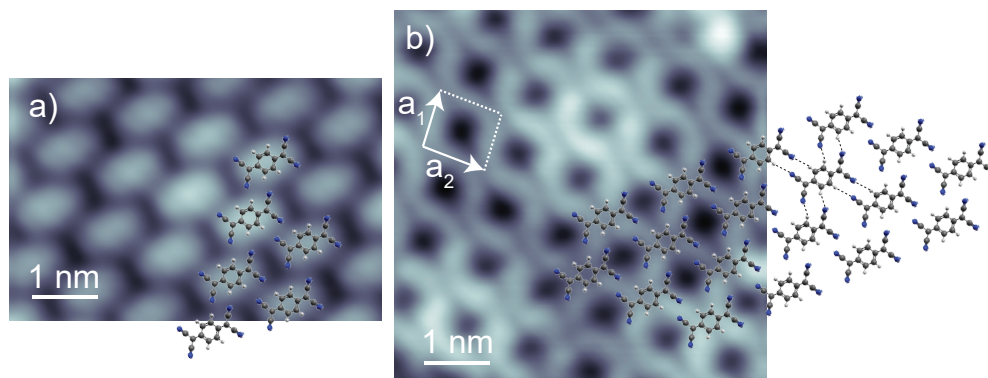
Figure 6.2: **a)** STM topography of a TCNQ island on MoS$_2$ /Ag(111) (V = 0.3 V, I = 40 pA). **b)** STM topography of TCNQ island on MoS$_2$ /Ag(111) (V = 0.8 V, I = 200 pA). Superimposed molecular model suggesting intermolecular bonding (dashed lines). White arrows represent the unit cell of the self-organized TCNQ domain with lattice vectors a_1=(0.9±0.10) nm and a_2=(1.0±0.10) nm and an angle of (96±2)° between them.

such close-packed assembly suggests that the intermolecular attractions are dominant for the formation of such islands and confirms the weak molecule–MoS$_2$ substrate interaction. The formation of highly-organized molecular islands on MoS$_2$ also reflects the low diffusion energy barrier on MoS$_2$ compared to the Ag(111) surface. Similar arrangements have been found for TCNQ deposited on weakly interacting substrates [26, 144–148].

6.2 Electronic Properties of TCNQ on MoS$_2$ /Ag(111)

To characterize the electronic structure, we first perform STS measurements on TCNQ on Ag(111). Fig. 6.3a shows a STM image of the randomly arranged molecules where the spectra were taken. Differential conductance spectra shown in Fig. 6.3b exhibit a fingerprint between 1 V to 2 V which does not exist on bare Ag(111). The energy of the broad resonances varies from molecule to molecule. The variation of the energies is a consequence of the screening from neighbouring molecules. We observe a large energy broadening and an energy discrepancy of the resonance depending on the molecules' environment. According to the TCNQ spectra of the previous works on Au(111) [26] and on Ag(111)[147], we can associate this resonance to tunnelling into the LUMO state of the molecules. At negative sample bias, we do not observe any feature similar to previous work [26].

In the following, we elaborate these observations compared to our measurement
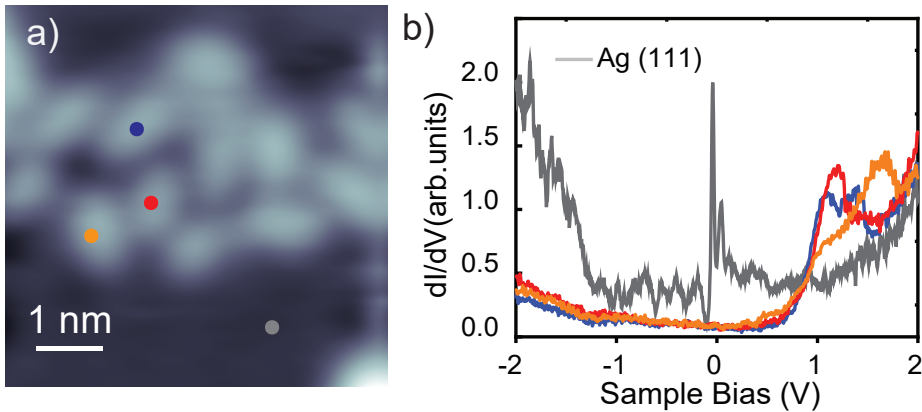
Figure 6.3: **a)** Topography image of TCNQ molecules on Ag(111) scanned at V = 1V, I = 200pA. **b)** dI/dV spectra taken on four TCNQ molecules display resonances at positive sample bias voltage from 1V to 1.7V. Feedback opened at I = 300pA, V = 2V with V$_{mod}$ =10mV. Gray spectrum recorded on Ag(111) as a reference spectrum.

on MoS$_2$/Ag(111). In the previous section, we have shown that there is a strong bias-voltage dependence of the appearance of TCNQ molecule on MoS$_2$ (Fig. 6.2a and b). This could point towards energetically well separate molecular states. To study this in more detail, we perform STS measurement on top of the molecules. At first glance and in contrast to TCNQ on Ag(111), the dI/dV spectra of TCNQ on MoS$_2$/Ag(111) in Fig. 6.4b exhibit narrow resonances.

The difference between spectra of TCNQ on Ag(111) compared to those on MoS$_2$/Ag(111) (broad vs. sharp resonances) is related to the lifetime broadening of the excited states due to the considerable hybridization on Ag(111) (as we have explained in chapter 3) which also confirms the decoupling properties of SL-MoS$_2$ [19]. The energy of the states vary for molecules on Ag(111) compared to those on MoS$_2$/Ag(111).

This can be explained via screening effect as we mentioned above, where different molecular assembly results in different screening effects. On Ag(111), TCNQ molecules take random arrangements whereas on MoS$_2$ each molecule has the same number of surrounding molecules which all take the same orientation. Beside the screening effect due to the neighbouring molecules, molecule on Ag(111) undergo additional screening effects due to the charges on the metal surface. With the well-decoupled and organized molecular islands on a MoS$_2$ layer, we have an ideal system to investigate the intrinsic properties of TCNQ. For this reason, in the following of this chapter we focus our study on TCNQ molecules on MoS$_2$/Ag(111).

The dI/dV spectra in Fig. 6.4b reveal two pronounced resonances at 470 mV and 640 mV which are not observed on bare MoS$_2$. Another peak is seen at 1.3 V which matches with the Γ resonance of the bare MoS$_2$. The gray spectrum on the nearby bare MoS$_2$ is recorded as a reference spectra with the same tip. At negative bias voltage, we observe an onset of conductance at -1.8 V which is located outside of the
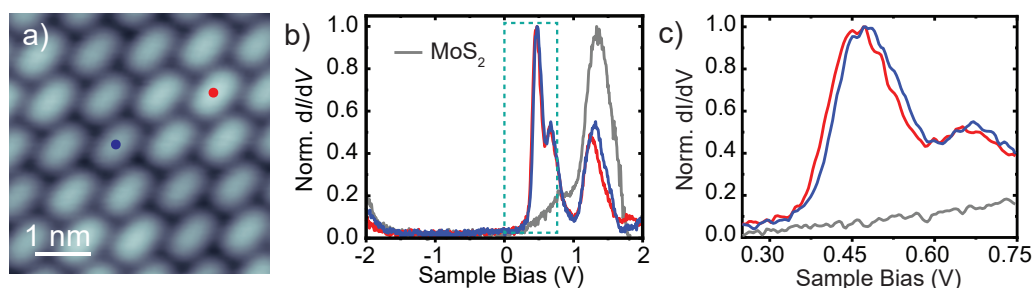
Figure 6.4: **a)** STM topography of a self-assembled TCNQ island on MoS$_2$/Ag(111), recorded at V = 0.2V, I = 20 pA. **b)** dI/dV spectra acquired on TCNQ molecules shown in **a)**, with the location marked by colored dots. The gray spectrum was recorded on bare MoS$_2$ layer for reference. Feedback opened at V = 2V, I = 100 pA, with V$_{mod}$ = 20mV. **c)** Zoomed spectra of **b)** shows 20 mV shift of the onset at positive bias.

MoS$_2$ band gap (see section 5.4).

To trace the origin of each resonance, we record the spatial distribution of the dI/dV signals (dI/dV maps) shown in Fig. 6.5(a-d) in constant-height mode at the energy corresponding to the four resonances. On the map acquired at 470 meV in Fig. 6.5a, we observe the same double U-shape distribution separated by a nodal plane which we observed Fig. 6.2b in the STM topography scanned at 800 mV. Fig. 6.5b shows a map taken at 640 meV corresponding to the second peak which exhibits the same shape as in Fig. 6.5a. As the spatial distribution is similar to the first map we can relate both resonances to the same origin. The map recorded at 1.3 V (the Γ resonance of MoS$_2$) shows only elliptical shapes as the STM topography (Fig 6.2a). The last map in Fig. 6.5d is acquired at -2 V. It shows a quite blurred dI/dV signal over the molecule, which is more localized in the center on the TNCQ compared to the elliptical distribution of Fig. 6.5c. The low-resolution dI/dV map could result from recording at a bias voltage outside of the MoS$_2$ band gap or because the tip is too far away from the surface.

To identify the molecular orbitals, we compare the recorded conductance maps to the calculated shape of the molecular orbitals in gas phase. By comparing our findings with former works, we could attribute the double U-shaped distribution to the LUMO of TCNQ [26, 144, 152]. Here, we simulate constant height dI/dV maps of the free, flat-lying molecule. First, we calculate the gas phase electronic structure using density-functional-theory calculations with the B3PW91 functional and the 6-31g(d,p) basis set as implemented in the GAUSSIAN09 package [47]. The iso-density contour plots of the HOMO, LUMO and two higher unoccupied molecular orbitals are shown in Fig. 6.5e (right panel). The calculations reveal that the HOMO and LUMO resonances are distinguishable by the absence and presence of the nodal plane at the
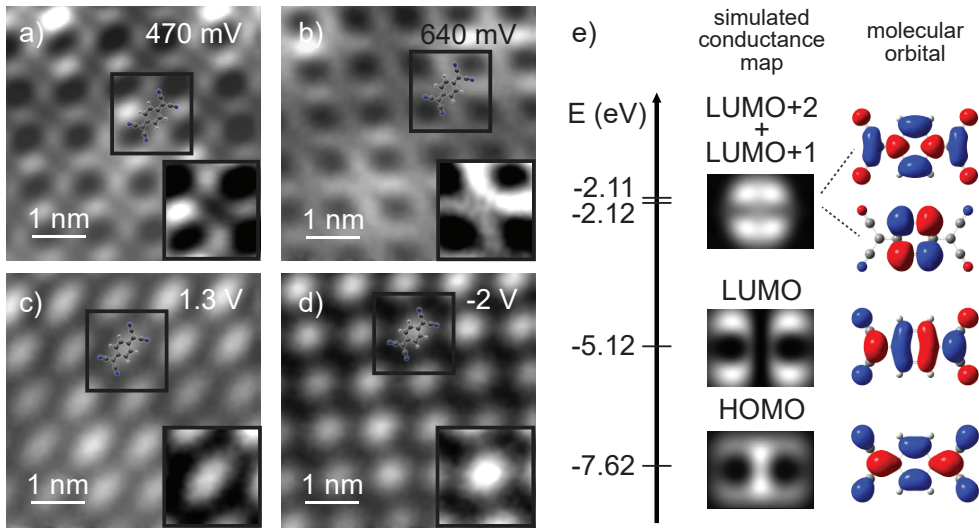
Figure 6.5: **a-d)** Constant-height dI/dV maps of a TCNQ island on MoS_2 recorded at the resonance energies derived in Figure 3d. Feedback opened at **a-c)** V = 2 V, I = 100 pA and **d)** V = -2V, I= 30 pA on the center of molecule with V_{mod} = 20 mV. Close-up images with enhanced contrast on one molecule are shown as inset for each map. **e)** Energy-level diagram of TCNQ determined from gas-phase DFT calculations (left). The isosurfaces of the frontier molecular orbitals are shown on the right. These have been used to calculate the tunnelling matrix element M_{ts} with an s-wave tip at a tip–molecule distance of 7.5 Å, workfunction of 5 eV. The map of the spatial distribution of $|M_{ts}|^2$ is shown in the middle panel.

center of the molecule. For direct comparison, as explained in chapter 2 we calculate the tunnelling matrix elements between the s-wave tip and the spatially-resolved molecular wave function across the molecule [43]. The maps of the square tunnelling matrix elements are depicted in Fig. 6.5e on the left of the corresponding molecular orbitals. Because the LUMO+1 and LUMO+2 resonances are quasi degenerated, we use the sum of their wave functions for the calculation of the tunnelling matrix elements. As expected, the nodal planes of the molecular orbitals dominate the simulated dI/dV maps and can be taken as a robust signature for molecular orbital identification. Additionally, the simulated maps reveal that the dI/dV intensity is not directly proportional to the isosurface density. For instance, there is hardly any intensity within the U shapes of the TCNQ LUMO, and the HOMO is mainly localized at the very center of the quinone moiety. We note that the simulated maps are obtained at a tip–molecule distance (center of the s-wave tip to center of the molecule) of 7.5 Å. This value was chosen because it represents reasonable tunnelling conditions in the experiments. However, variation of the tip height by (± 2 Å) does not have any influence on the observation of the main features within the simulated map (i.e., nodal planes, or intensity maxima) [88].

Now, comparing this to the experimental dI/dV maps, we can identify the origin of the molecular resonances. As mentioned earlier we can attribute the resonance at 470 mV to the LUMO where the double-U shape map is in good agreement with the calculation of the tunnelling matrix element. As the spatial distribution for the resonance at 640 mV is similar to the first map we also can relate it to the LUMO resonance. As the energy difference (170 mV) between these two resonances lies within the typical vibrational energies of the organic molecules we may allocate the second peak to a vibronic excitation. We will clarify this point in the following section.

The dI/dV map recorded at the energy of 1.3 V (Fig. 6.5c) with the elliptical shape is similar to the STM image taken within the MoS$_2$ band gap in Fig. 6.2c. DFT calculations show that the next higher unoccupied molecular orbital lies 3 eV above the LUMO resonance which also exhibits a nodal plane which is not observed in the experiment. Therefore, we cannot attribute the origin of the third resonance (at 1.3 V) to the molecular orbital (LUMO+1) but to direct tunnelling into the MoS$_2$ state at the energy of the Γ point.

Fig. 6.5d presents the conductance map acquired at -2 V. The strong localization of the dI/dV signal on the center of TCNQ agrees with simulated conductance maps of the HOMO (Fig. 6.5e, left panel). DFT estimates the HOMO–LUMO gap of 2.5 eV which fits with our results. However, this value is smaller than what was found in former work of TCNQ on gr/Ir(111) 3.5eV [152]. We note that, our data clearly shows that the HOMO is at or within the valence band of MoS$_2$. Therefore, we refrain from a definite assignment.

Considering the simulation, here we elaborate the energy level alignment. We find the LUMO resonance close to the Fermi level of the substrate, while the HOMO lies far below it. This indicates that TCNQ molecules stay neutral with a negligible amount of charge transfer, in contrast to the strong acceptor nature of TCNQ. Nonetheless, its electron affinity of $\sim$ 3.4 eV [138, 143] is consistent with the LUMO alignment just above E$_F$ when considering the work function of MoS$_2$ /Ag(111) of 4.7 eV [153]. This behaviour has also been observed when a thin layer of TCNQ was investigated on Au(111) surface. Due to the weak interaction of TCNQ molecules with the substrate LUMO resonance in the intramolecular structure is fairly unperturbed [26]. We also observe a $\sim$ 20 mV shift of the LUMO onsets (Fig. 6.4c) between the spectra of TCNQ molecules lying at the top or hollow sites of the moiré structure of MoS$_2$. These shifts are in the same order of magnitude with the moiré-induced energy shifts in unoccupied states of the MoS$_2$ layer (see section 5.4) and thus reflect the different screening properties from the substrate. In turn, we do not observe any modification of the electronic structure of MoS$_2$. This indicates weak interactions of the molecules all along with the MoS$_2$ layer.

We notice that the resonance at 470 mV has a $\sim$ 100 mV widths, which is significantly narrower than the typical resonance width observed on metal surfaces ($\sim$ 500 mV) [26, 147]. This reflects the decoupling properties of MoS$_2$ layer on a metal substrate. The width we observe here is broader than the width of HOMO resonances in other organic molecules on MoS$_2$/Au(111) [19, 88, 154]. It can be due to the locations of the HOMO and LUMO resonances. The HOMO resonance is protected by the MoS$_2$

band gap in those cases, here the LUMO lies right at the onset of the conduction band. This provides relaxation pathways for electrons tunnelling into the LUMO, though still significantly less than on the bare metal.

6.3 Vibronic Excitation of TCNQ on MoS_2/Ag(111)

In the previous section, we associated the origin of both resonances at 470 mV and 640 mV to the LUMO of the TCNQ molecule. Here we analyze it in more detail in Fig. 6.6. The experimental spectrum of TCNQ in a close-up view of the spectral range is shown in Fig. 6.6b (low panel). The LUMO peak is set to zero energy and the peak height has been normalized. We observe satellite peaks which have been attributed to the excitation of the intermolecular vibronics in former works [18, 27, 67, 70, 117, 155, 156]. Vibronic states can be explained upon charge injection, when vibrational excitation of the molecule is coupled to an excited electronic state. The spatial distribution associated to these sidepeaks should obey the same symmetry as the parent orbital state [62, 157, 158]. The origin of the vibrational process observed in Fig. 6.6b is schematically illustrated in Fig. 6.6c. This representation of the vibronic process is also known as the Franck-Condon model. When probing the LUMO in tunnelling spectroscopy, the molecule is transiently negatively charged. Within the Born-Oppenheimer approximation, this process is described by a vertical transition in the energy level diagram from the ground state M^0 to the excited state M^-. Upon charging, the molecule undergoes a geometric distortion, captured by the shift of the potential energy curve of the excited state. Therefore, the electronic excitation allows for an additional excitation of a vibration within the molecule (vibronic state). To confirm the vibronic excitation hypothesis, we use the Franck-Condon model. As we explained in chapter 3, in the Franck-Condon picture the peak intensity I_{nk} of the nth excitation level of the mode k is described by Poisson distribution as [71, 87]

$$I_{kn} = e^{S_k} \frac{S_k^n}{n!}$$

where the S_k is the Huang-Rhys factor ($S_k = \frac{\varepsilon_k}{\hbar\omega}$) which reflects the electron-phonon coupling strength [71] and ε_k is the relaxation energy. From DFT calculations, we obtain ε_k and S_k for all the vibrational eigenmodes in the negatively charged states of the TCNQ molecule.

From the DFT calculation, we extract the geometry of the molecule in the ground state M^0 and the excited state M^- to obtain the displacement of the atoms upon charging. Then we compare it to the displacement of the atoms upon vibration. Thus, we can quantify the Huang-Rhys factor for all the vibrational eigenmodes, (plotted in upper panel of Fig. 6.6b as red dots in the right axis). To each of the vibronic states, we apply a Lorentzian peak with a full width at half-maximum
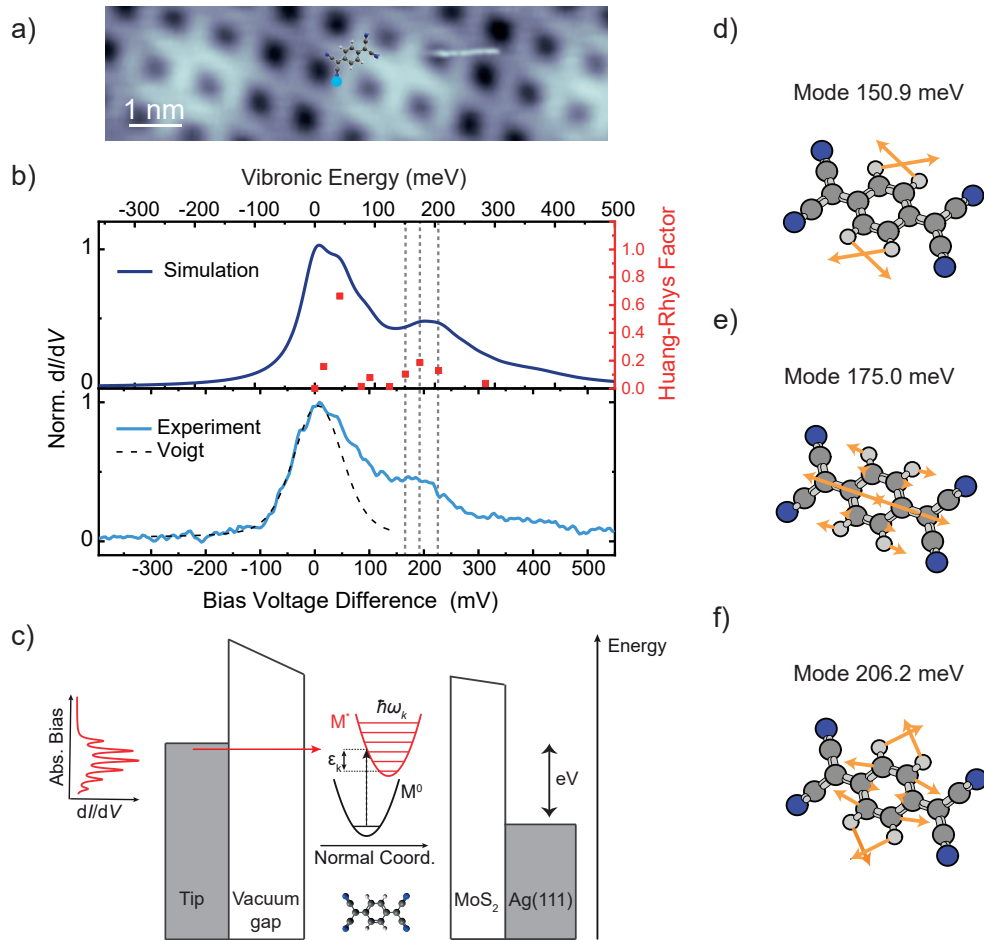
Figure 6.6: **a)** STM topography of a TCNQ island recorded at V = 1V, I = 10 pA. **b)** Simulated (top panel) and experimental (bottom panel) dI/dV spectra at the position indicated by the blue dot in a) with feedback opened at V = 2V, I = 100 pA, with V$_{mod}$ = 10mV. The simulated spectrum is obtained from DFT calculations for all the vibrational mode of the TCNQ$^-$ molecule with a Huang-Rhys factor higher than 0.01 (dots associated with the right axis). A Lorentzian peak of 60 meV broadening is applied to all of these modes. **c)** Schematic representation of electron transport through a TCNQ molecule adsorbed on MoS$_2$/Ag(111): singly charged TCNQ$^-$ is formed upon injecting an electron into a vibronic state of an unoccupied molecular electronic level. **d-f)** Visualization of the vibrational modes contributing to the satellite peaks. The orange arrows represent the displacement of the atoms involved in these vibrations.

(fwhm) of 60 meV and intensity proportional to the Poisson distribution. This leads to a simulated Franck-Condon spectrum shown the upper panel of Fig. 6.6b. We find a good agreement between our calculation and the experimental spectrum as depicted in Fig. 6.6b, which enables us to identify the vibrational modes that are involved in the vibronic excitations. Note that the voltage drop across the SL-MoS$_2$ is scaled by $\sim 10\%$ between the experimental bias voltage axis (low panel) compared to the calculated energy axis (top panel) [19, 77]. As we have explained in chapter 3, implementing the decoupling layer we thus consider the STM junction as a double barrier junction where the applied bias voltage drops both over the vacuum between tip and adsorbate and the decoupling layer (see Fig. 6.6c).

Based on the Huang-Rhys factors ($S_k > 0.1$), five vibrational modes are mainly responsible for the features observed in STS. Two of the modes are lower in energy (14.8 meV and 41.7 meV) than our energy resolution of 60 meV, and three other modes with energies 150.9 meV, 175.0 meV and 206.2 meV are resolved via the simulation. These three modes correspond to the in-plane stretching modes represented in Fig. 6.6(d-f) which are particularly sensitive to the charging. Eventually, we attribute the peak at 640 meV (described in the previous section) to the vibronic peak which consists of three vibrational modes. The mode at 41.7 meV has a large Huang-Rhys factor. The excitation of this mode is not energetically well separated from the elastic onset of the LUMO in experiment. However, this mode contributes to an asymmetric lineshape, which can be seen by comparing the low-energy flank to the high-energy fall-off of the first resonance. The low-energy side can be fitted by a Voigt profile (see the black dashed line in Fig. 6.6b lower panel) and suggests a lifetime broadening of 35 ± 10 meV. This is, however, insufficient for a peak separation from the 40-meV mode.

We note that the experimental spectrum was taken on a cyano group, where no nodal planes exist in the LUMO, as their presence may lead to vibration-assisted tunnelling in addition to the bare Franck-Condon excitation [88]. The dI/dV spectra taken on three different sites of the TCNQ molecule are displayed in Fig. 6.7a. The local sites are shown as blue, red and orange dots in the inset of Fig. 6.7a. The zoomed-in spectra in the unoccupied states reveals the intense (resonance) peak on cyano group (blue dot - blue spectrum). On the other positions, the relative intensities of the vibronic resonances are different compared to the elastic peak.

6.4 Conclusion

We have characterized the adsorption properties of the charge acceptor TCNQ on MoS$_2$/Ag(111). The growth follows the familiar self-assembling process similar to other substrates. Molecules organize in large and highly-ordered molecular islands on MoS$_2$ at 230k, whereas on Ag(111) they formed random configurations. Formation of the highly organized molecular islands on MoS$_2$ is a consequence of the lower diffusion energy barrier on MoS$_2$ than on Ag(111). We have identified the HOMO and
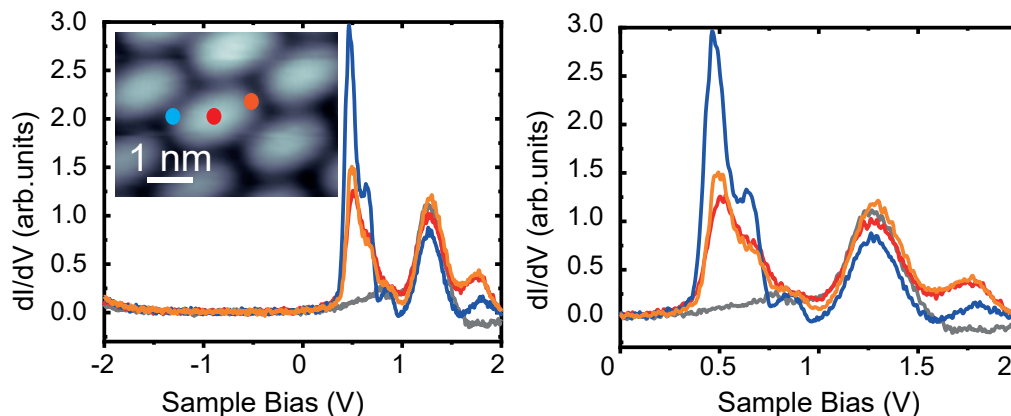
Figure 6.7: **a)** Constant height dI/dV spectra on three different sites on TCNQ on MoS$_2$/Ag(111) (feedback opened at I = 100pA, V = 2V with V$_{mod}$ = 20mV) (inset : topography image scanned at V = 0.2V, I = 10pA). **b)** Zoomed-in spectra of **a)** shows the intense peak on the corner of TCNQ molecule (blue dot) compared to other sites.

LUMO resonances of TCNQ on SL-MoS$_2$. Spectroscopy has revealed that the LUMO resonance lies at the conduction band onset of MoS$_2$, whereas the HOMO lies within the valence band. TCNQ molecules adsorbed on SL-MoS$_2$/Ag(111) also exhibited the vibronic fingerprint within the MoS$_2$ band gap, which is in good agreement with DFT calculations based on Franck-Condon picture. This further confirms that the SL-MoS$_2$ acts as a decoupling layer on Ag(111) similar to Au(111).

Charge Transfer Processes in TTF–TCNQ Compound on MoS$_2$/Ag(111)

After characterizing TCNQ molecule in the previous chapter, we add an electron donor counterpart to our system to investigate charge transfer processes. Over the past years organic charge transfer compounds (donor-acceptor species) have attracted attention due to the various applications in opto-electronic devices particularly in organic solar cells [11, 159] and organic light-emitting diodes [12, 160]. The prototype organic molecules tetrathiafulvalene (TTF) and tetracyanoquinodimethane (TCNQ) are widely used as donor and acceptor species in charge transfer complexes (CTC), due to the low ionization potential (IP) $\sim$ 6.83 eV [141, 161] of TTF and the high electron affinity (EA) of TCNQ mentioned in the previous chapter.

Since its discovery in 1973 [162], the TTF-TCNQ compound has been established as a one-dimensional organic metal with high conductivity at room temperature [162, 163]. In bulk TTF-TCNQ compound, donor and acceptor molecules are stacked in rows. Thus, charge delocalization due to π overlap of molecular orbitals along the stacks, leads to metallic conductivity [164]. The CTC shows a charge transfer (CT) of 0.6 e/molecule [165, 166] between the highest occupied molecular orbital (HOMO) of the donor TTF and the lowest unoccupied molecular orbital (LUMO) of the acceptor TCNQ. The molecular structures, the HOMO of TTF and the LUMO of TCNQ are shown in Fig. 7.1. TCNQ can accommodate up to two electrons [138, 139], on the other hand TTF can donate two electrons [167].

The electronic properties of a monolayer of the TTF-TCNQ compound on a metal surface can be influenced by the underlying substrate. Depositing TTF-TCNQ on a Au(111) surface enhances the CT to 1e/molecule compared to the bulk CTC due to the CT with the metal substrate [168, 169]. To reduce the impact of the metal and being able to study the CT between the donor and acceptor species, here we utilize SL-MoS$_2$ as a decoupling layer like in the previous chapter.
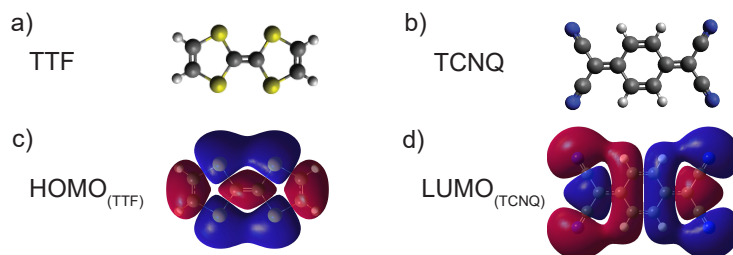
Figure 7.1: Chemical structure of **a)** TTF and **b)** TCNQ with the corresponding DFT calculation of the iso-density of the frontier molecular orbitals for isolated molecules. **c)** TTF HOMO and **d)** TCNQ LUMO.

7.1 Electronic Properties of TTF on MoS$_2$/Ag(111)

With evaporation of TTF-TCNQ salt at 200 K and annealing at 250 K for 15 min, we obtain pure TTF molecular islands on MoS$_2$/Ag(111). Fig. 7.2a displays a self-assembled TTF molecular island and a corresponding spectrum on a TTF molecule. TTF molecules appear as round and featureless protrusions in Fig. 7.2a (inset). At positive bias, the dI/dV signal reveals two resonances at 0.8V and 1.3V (see Fig. 7.2a - purple spectrum) and at negative bias there is an onset around -0.8V followed by several satellite peaks. The resonances at positive bias are attributed to the tunnelling through the conduction band (CB) of SL-MoS$_2$ (gray spectrum in Fig. 7.2a). For a precise investigation of the resonances at negative bias, we present in Fig. 7.2b a better resolved spectrum around the energy of the onset of the dI/dV signal discussed above. Note that this spectrum is recorded with the tip positioned slightly away from the center of the molecule in Fig. 7.2b (inset). We suggest that the state at negative bias (- 0.85 V) is attributed to the tunnelling through the HOMO resonance of the TTF molecule. However, we do not record the dI/dV maps at this energy resolving the shape of the HOMO.

Besides, we observe several additional peaks at - 0.92 V, -1.05 V, -1.12 V and -1.27 V with various intensities. If we assume the first peak to be the HOMO resonance, these additional peaks can not be associated to the other occupied molecular orbitals (HOMO-1, HOMO-2,...). Indeed, from gas phase DFT calculation we estimate an energy difference of 1.7 eV between the HOMO and the HOMO-1. Thus, these peaks should most probably arise from vibronic excitations.

To confirm that, we simulate the vibronic spectrum associated to the positively charged TTF. For that, we applied the Franck-Condon excitation model as described in chapter 3, and thus determine the Huang-Rhys factors for the vibrational modes of the TTF molecules (see red dots in the lower panel in Fig. 7.3). To each vibronic mode, we applied a set of Lorentzian peak with HWHM of 20mV. For one mode, this set of peaks corresponds to different hamonics of this mode and their intensities follow the Poisson distribution associated to the calculated Huang-Rhys factor (Fig.
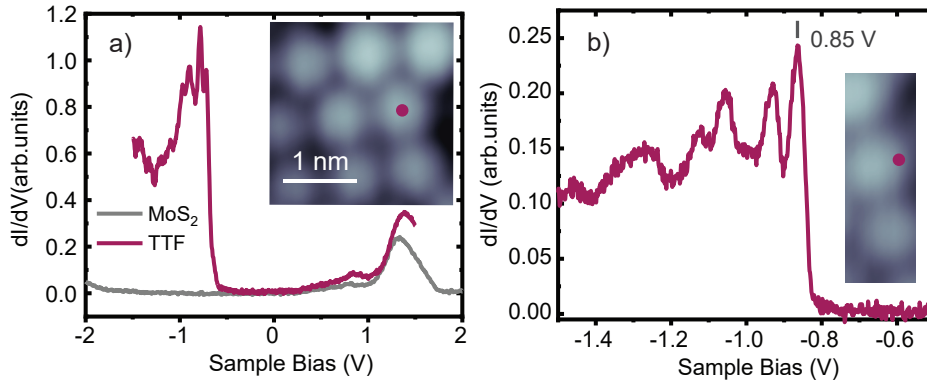
Figure 7.2: **a)** dI/dV spectrum taken on TTF molecule. Feedback opened at V = -1.5V, I = 300pA with V_{mod} = 3mV. Gray spectrum recorded on MoS_2 as a reference spectrum. Feedback opened at V = 2V, I = 75pA with V_{mod} = 10mV. (inset: Topography image of self-assembled TTF on MoS_2/Ag(111) scanned at V = 1.2V, I = 50pA). **b)** dI/dV spectrum recorded for a smaller energy range around the onset at 0.8V. Feedback opened at V = -1.5V, I = 200pA with V_{mod} = 3mV.

7.3 - lower panel). In order to consider the voltage drop in the DBTJ with the MoS_2 layer, we apply a scaling factor ($\sim$ 10%) [19, 77] between the experimental bias voltage axis and the simulated energy axis, as we have explained in chapter 3. We find a good agreement between experimental and simulated spectra (see Fig. 7.3). In the simulation, we mainly resolve two in-plane stretching vibrational modes at the energies of 60 meV and 178 meV. The peak at 120 meV is attributed to the excitation of the second harmonic of the first vibrational mode. We also assign the peak at 238 meV to the coupling of the first and second vibrational modes.

Therefore, via simulation which considers positively charged TTF, we can confirm our assumption that the first peak at negative bias (- 0.85 V) is associated to the tunnelling through the HOMO of the TTF molecule.

7.2 Charge Transfer Processes of TTF-TCNQ on MoS_2/Ag(111)

After growing single-layer MoS_2 on Ag(111) surface as explained in chapter 5, we co-deposit TTF and TCNQ on a cold sample (200K) followed by annealing at 250K for 15 min to obtain highly ordered molecular islands. The result is depicted in Fig. 7.4a, where the STM image shows two different molecular assemblies. The first molecular assembly in Fig. 7.4b depicts a mixed organization consisting of two types of molecules: elongated protrusions and double back-to-back U shapes. The second molecular assembly in Fig. 7.4c, shows a pure self-assembled TCNQ island. The
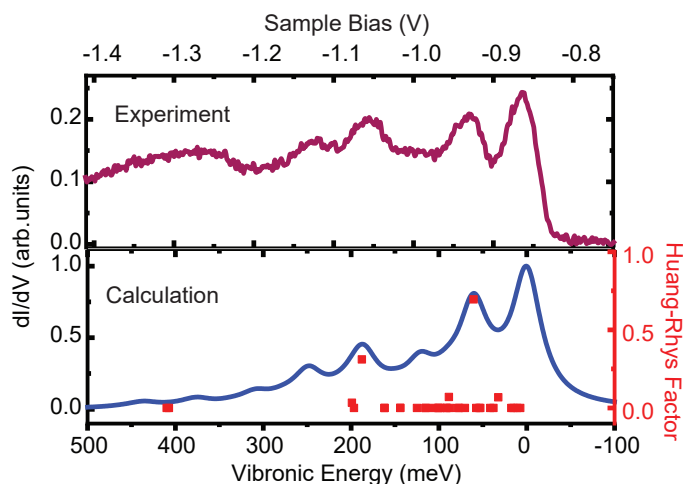
Figure 7.3: Simulated (bottom panel) and experimental (top panel) dI/dV spectra with feedback opened at V = -1.5V, I = 200 pA and V$_{mod}$ = 3mV. The simulated spectrum is obtained from DFT calculations for all the vibrational modes of the TTF$^+$ molecule with a Huang-Rhys factor higher than 0.01 (dots associated with the right axis). A Lorentzian peak of 20 meV of HWHM is applied to all of these modes. In the voltage bias and vibronic energy axes, we account 10% voltage drop for MoS$_2$.

latter is thoroughly studied in chapter 6, and here we investigate the former mixed organization.

In a zoomed-in STM image (Fig. 7.5a), the bright protrusions appear in a butterfly shape which resembles the electron-density distribution of the HOMO of TTF molecules (see Fig. 7.1c). The double back-to-back U shape with a nodal plane in the center resembles the electron-density distribution of the LUMO of TCNQ molecules (see chapter 6 Fig. 6.5). Beside the molecules with a clear orbital shape described above, it seems that there are also molecules in the 'dark' tiles indicated as red and green circles in Fig. 7.5a. We propose two molecular models as overlaid in Fig. 7.5b and 7.5c, which consist of ordered arrays of TTF and TCNQ molecules although there is a doubt for the exact orientation of TTF. In one proposed model displayed in Fig. 7.5b, all TTF take the same orientation in each row. With the second model presented in Fig. 7.5c, we propose that the 'dark' TTF are rotated with respect to the 'bright' TTF neighbours. The reason we propose the second model in Fig. 7.5c is that between the bright and dark TTF, the nodal plane in the center of the molecule may appear with different orientations (see red and orange dashed lines in Fig. 7.5c).

Therefore, we have a mixed structure of TTF and TCNQ which forms arrays of molecules with a (TTF)$_1$(TCNQ)$_1$ stochiometry. A similar structure was also observed in a recent work, for TTF-F4TCNQ adsorbed on a graphene layer [170]. However, the exact orientation of the TTF is still under debate and would require AFM (Atomic Force Microscopy) measurements to resolve the molecular structures

within the island.
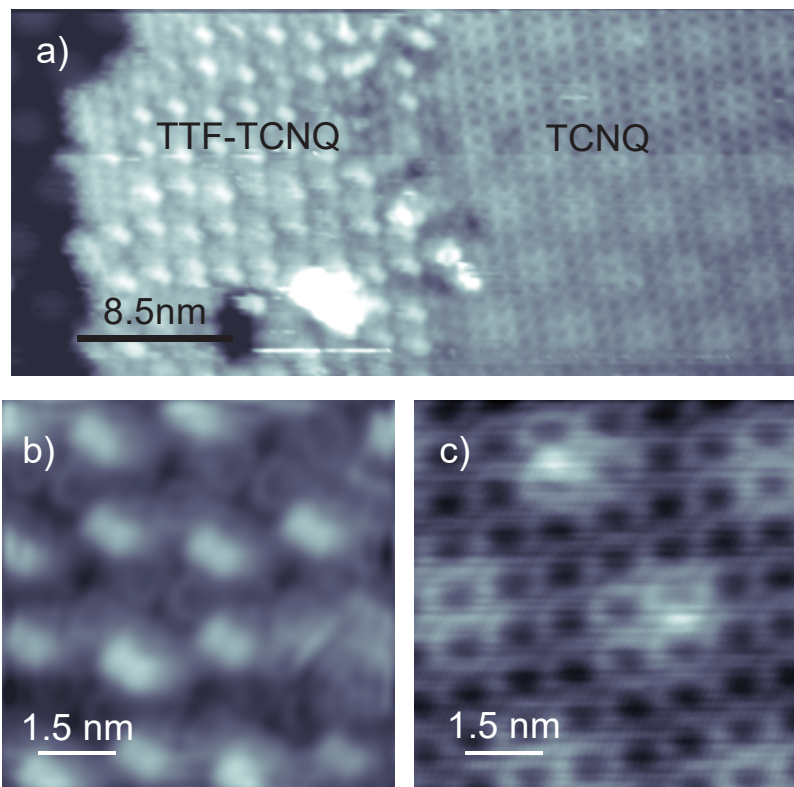
Figure 7.4: **a)** STM topography of self-assembled TTF-TCNQ monolayer next to self-assembled TCNQ monolayer on MoS_2/Ag(111) (V = 1V, I = 20pA). **b)** STM topography of the mixed structure of TTF-TCNQ monolayer on MoS_2/Ag(111) (V = 0.3V, I = 20pA). **c)** STM topography of TCNQ monolayer on MoS_2/Ag(111) (V = 1V, I = 20pA).

7.2.1 Spectroscopy Along TTF-TCNQ Structure

We have determined the electronic features for the pure TTF (see above) and the pure TCNQ (see chapter 6). Now we focus on investigating the electronic properties of these two molecules within the mixed structure. We record a set of dI/dV spectra along different directions in the mixed structure. The line spectra in Fig. 7.6(b and e) represent the stacked spectra along the (molecular) rows where the colors indicate the dI/dV intensities. First, we record dI/dV spectra along a TTF row, then along a TCNQ row and eventually, along the alternating TTF-TCNQ row.

Fig. 7.6 shows the line spectra along TCNQ (Fig. 7.6b) and along TTF (Fig. 7.6e) rows. In both cases we observe two new features: first, there are onsets of
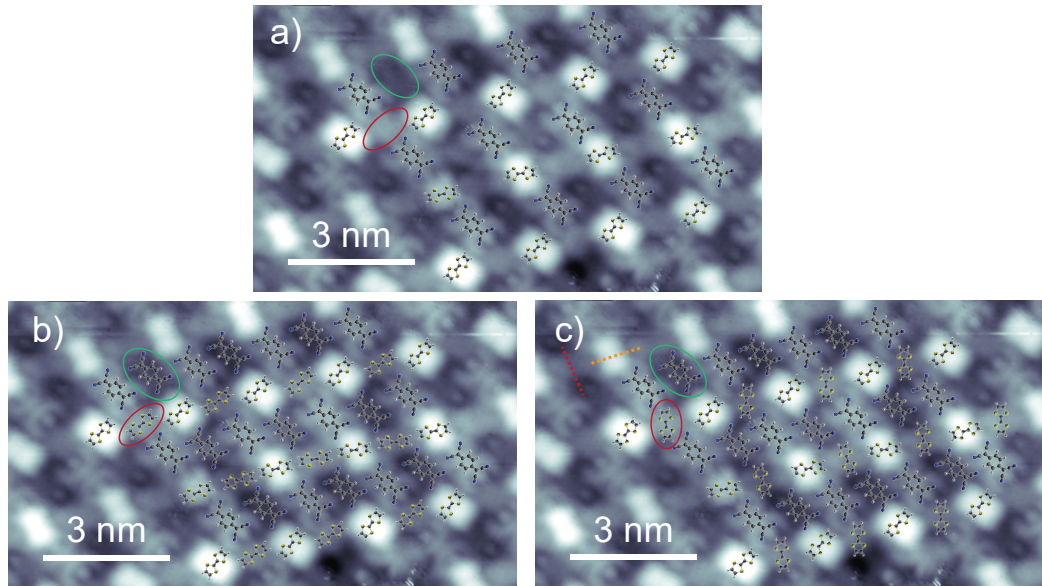
Figure 7.5: STM topography of self-assembled TTF-TCNQ on MoS$_2$/Ag(111) (V = 1V, I = 20pA). The proposed overlaid molecular model displays the arrangement of TTF and TCNQ in the mixed structure. **a)** The dark tiles between TTF and TCNQ are depicted as red and green circles, respectively. **b)** In the first proposed model, all TCNQ molecules take the same orientation and all TTF appear in the same orientations as the neighbours. **c)** In the second proposed model, TCNQ molecule take the same orientation as in **b)** but dark TTFs are rotated with respect to the neighbours TTF. The dashed red and orange lines show the different orientations of the nodal plane in dark and bright TTF.

conductance close to the Fermi energy at both bias polarities. We note that, these resonances slightly vary from molecule to molecule. Secondly, some parabolas appear at various energies in both positive and negative biases. An exemplary parabola is shown as a dashed-line in Fig. 7.6b. In the following section, we clarify the association of the parabolas to the so-called charging peaks as we have explained in chapter 3.

In the line spectroscopy recorded over TCNQ molecules (see Fig. 7.6a), we observe a minimum energy gap of $\sim$ 65 meV in Fig. 7.6b. At positive bias the onset of conductance varies from $\sim$ 20 mV to $\sim$ 280 mV and at negative bias from $\sim$ -45 mV to $\sim$ -150 mV. The vertical dashed lines represent the limits of the onsets variations. Two exemplary spectra from the line spectroscopy are shown in Fig. 7.6c. The blue spectrum shows an onset at -53 mV at negative bias and a sharp resonance at 150 mV at positive bias. The green spectrum shows an onset at -115 mV at negative bias and an onset at 123 mV and a sharp peak at 700 mV at positive bias. Horizontal dashed lines in Fig. 7.6b show the location of corresponding spectra. Here, we remark that the sharp resonances correspond to the parabolas which we have observed in the line

spectra.

Line spectroscopy along the TTF row is depicted in Fig. 7.6e. The minimum energy gap is given by the value of $\sim$ 80 meV. The variation of the onset at positive bias is from $\sim$ 30 mV to $\sim$ 150 mV, and at negative bias from $\sim$ -50 mV to $\sim$ -250 mV. Two spectra are picked up from the stacked spectra and shown in Fig. 7.6f. The red spectrum depicts an onset at $\sim$ - 40 mV at negative bias which is accompanied by a sharp peak at $\sim$ 260 mV at positive bias, whereas the orange line shape shows no sharp peak in the bias window but the onsets of $\sim$ -190 mV and $\sim$ 130 mV at negative and positive bias, respectively. In Fig. 7.6e, the onset variations are depicted at the vertical dashed lines.

Fig. 7.7a depicts an alternating TTF-TCNQ row in the mixed structure. Line spectra along this row are shown in Fig. 7.7b. We observe a variation in the onset at negative bias from $\sim$ -17 mV to $\sim$ -65 mV which is a smaller variation compared to the pure TTF row and TCNQ row. We display two exemplary spectra in Fig. 7.7c. In both spectra, at positive bias we observe sharp peaks at different energies, and at negative bias there are the onsets of conductance near the Fermi level. The blue spectrum shows an onset at -17 mV, and the red one has an onset at -65 mV. The arrows display the sharp resonances at 113 mV and 650 mV for the blue and red spectrum, respectively. The blue spectrum has another resonance at 930 mV. In general, we observe that the closer the stepwise onset of conductance is to the Fermi level at negative bias voltage, the smaller is also the peak energy at positive bias voltage. We will show that both features are inherently related to each other with the sharp peak being a signature of the tip-induced charging.

To resume, within the mixed TTF-TCNQ molecular island we observe some electronic states quite close to the Fermi energy at positive and negative bias voltage. This observation is in strong contrast with the electronic structure of the pure TTF and TCNQ islands, with a large HOMO-LUMO gap. Additionally, we detect some sharp resonances whose energies vary strongly from one molecule to another and that we did not observe within the pure TTF and TCNQ island. In the following, we will explain the particularities of the spectroscopic feature of the mixed structure through two distinct charge transfer mechanisms: **I)** permanent charge transfer, **II)** tip-induced charge transfer.

I) Permanent charge transfer

Here, we explain the origin of the states near Fermi level in the mixed TTF-TCNQ structure. To do that, we investigate two exemplary spectra picked up from the mixed structure: one on TTF and another on TCNQ.

An exemplary dI/dV spectrum recorded on TTF molecule (in the TTF row in Fig. 7.6e) is shown in Fig. 7.8b. At negative bias, we observe the onset of the resonance at -60 meV and at positive bias the onset of the resonance is at 140 meV. Thus, we find a small gap with the value of 200 meV.

In Fig. 7.8d we show an exemplary spectrum on TCNQ (in the TCNQ row in
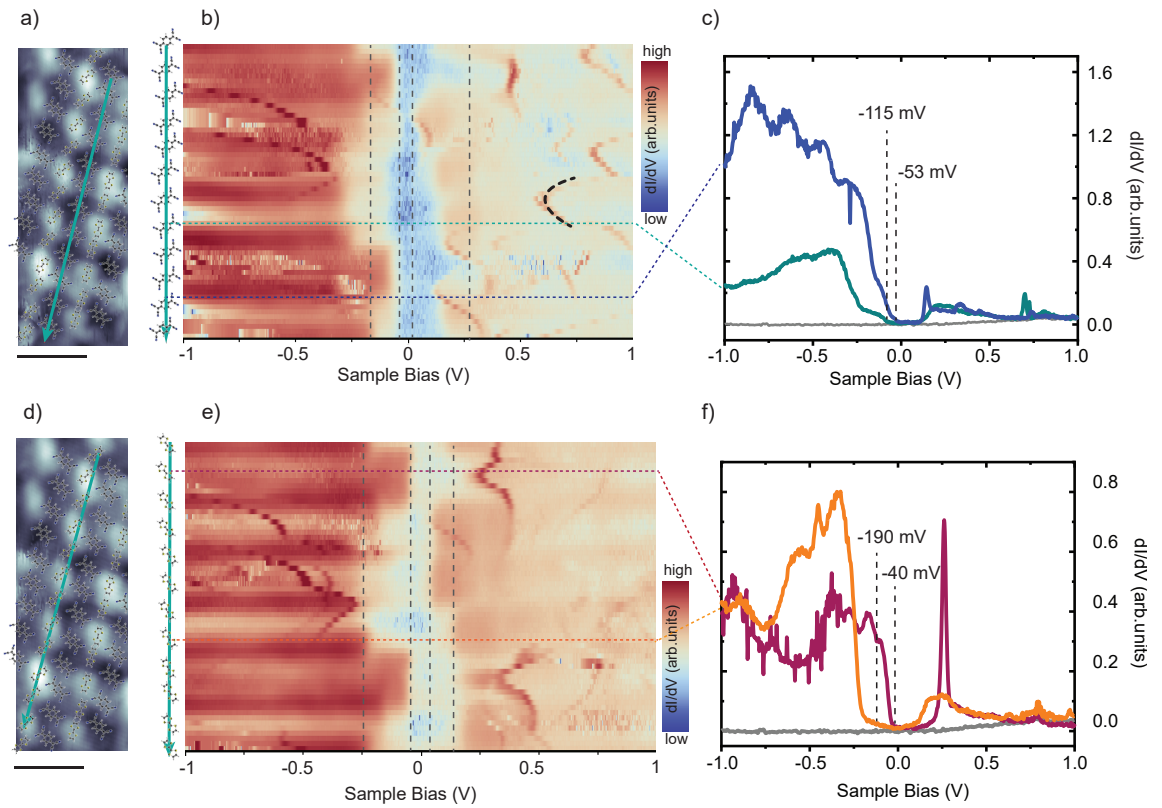
Figure 7.6: **a)** Topography image of TTF-TCNQ mixed structure scanned at V = 1V, I = 20pA. The scale bar is 2.5 nm. **b)** False-color plots of dI/dV spectra taken along TCNQ row (11 nm) shown in the left panel, (feedback opened at V = 1 V,I = 75 pA with V_{mod} = 10 mV). An exemplary parabola is displayed as the black dashed-line parabola. Vertical dashed-lines display the variations in conductance onsets of both polarities. **c)** Two exemplary spectra of the set shown in **b)**, the locations corresponding to the spectra are depicted as blue and green dashed line in **b)**. Gray spectrum is the reference spectrum on MoS_2. **d)** Topography image of TTF-TCNQ mixed structure scanned at V = 1V, V = 20pA. The scale bar is 2.5 nm. **e)** False-color plots of dI/dV spectra taken along TTF row (11 nm) shown in the left panel. (feedback opened at V = 1 V,I = 75 pA with V_{mod} = 5 mV). **f)** Two exemplary spectra of the set shown in **e)**, the locations corresponding to the spectra is depicted as red and orange dashed line in **e)**. Gray spectrum is the reference spectrum on MoS_2.
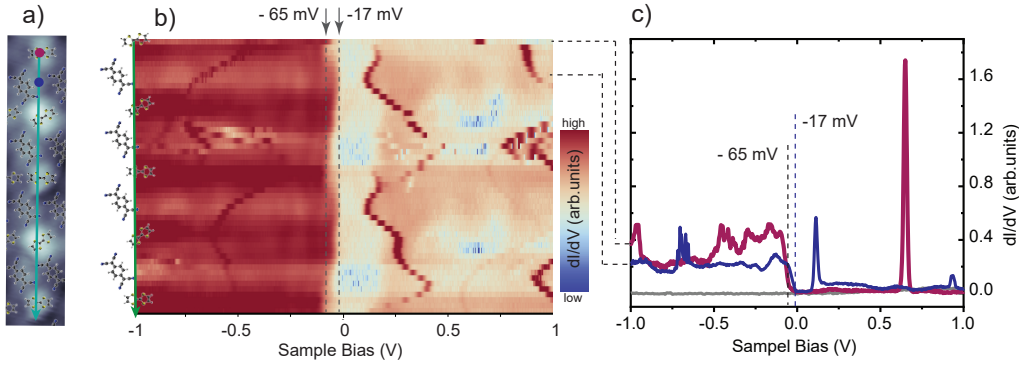
Figure 7.7: **a)** Topography image of TTF-TCNQ mixed structure scanned at V = 1V, I = 20pA. **b)** False-color plot dI/dV spectra taken along the green line (7.8 nm) shown in **a)** (feedback opened at V = 1 V,I = 75 pA with V$_{mod}$ = 10 mV). The variation of the onset at negative bias is $\sim$ 82 mV. The vertical dashed-lines show the variations of the onset at negative bias. **c)** Two exemplary spectra of the set shown in **b)**, the spot correspond to the spectra is shown at red and blue dots in **a)**. Gray spectrum is the reference spectrum on MoS$_2$.

Fig.7.6b). Here, at negative bias the onset of the state is observed at -115 meV and at positive bias the onset is at 145 meV. Similar to the previous case, here we also find a small gap of 260 meV. In both cases, the gap is too small to be assigned to the HOMO-LUMO gap.

In a simple model, we can attribute the modification in the electronic structure to the interaction between (donor) TTF and (acceptor) TCNQ via charge transfer (CT). Due to the charge transfer between TTF and TCNQ, these molecules in the mixed structure are not in the neutral states but the TTF charge state is +1 and the TCNQ charge state is -1. As a consequence of this CT, TTF gives an electron to TCNQ. Then, the HOMO state of TTF and LUMO state of TCNQ split into singly occupied molecular orbital (SOMO) and singly unoccupied molecular orbital (SUMO), respectively (see Fig. 7.8a and c -left panels). Therefore, we attribute the resonances at negative and positive bias to the SOMO and SUMO, respectively.

The molecular orbitals corresponding to these states are shown in Fig. 7.8a and c (right panels). The energy gap between SOMO and SUMO is determined by the Coulomb repulsion energy [171, 172]. DFT calculates the SOMO-SUMO gap of 1.4 eV and 1.5 eV for TTF$^+$ and TCNQ$^-$, respectively. Moreover, for other systems the SOMO-SUMO gap were also found in similar range of values [154, 170]. The small value of SUMO-SOMO gap in our experiment can be explained via electronic delocalization over the molecular island that significantly leads to the smaller Coulomb repulsion energy.

The SUMO and SOMO can be observed in our experimental results in the topography images. The observation of TCNQ LUMO shape and TTF HOMO shape at 0.3V (Fig. 7.1c) is in agreement with Fig. 7.8(a and c) and SUMO/SOMO picture.
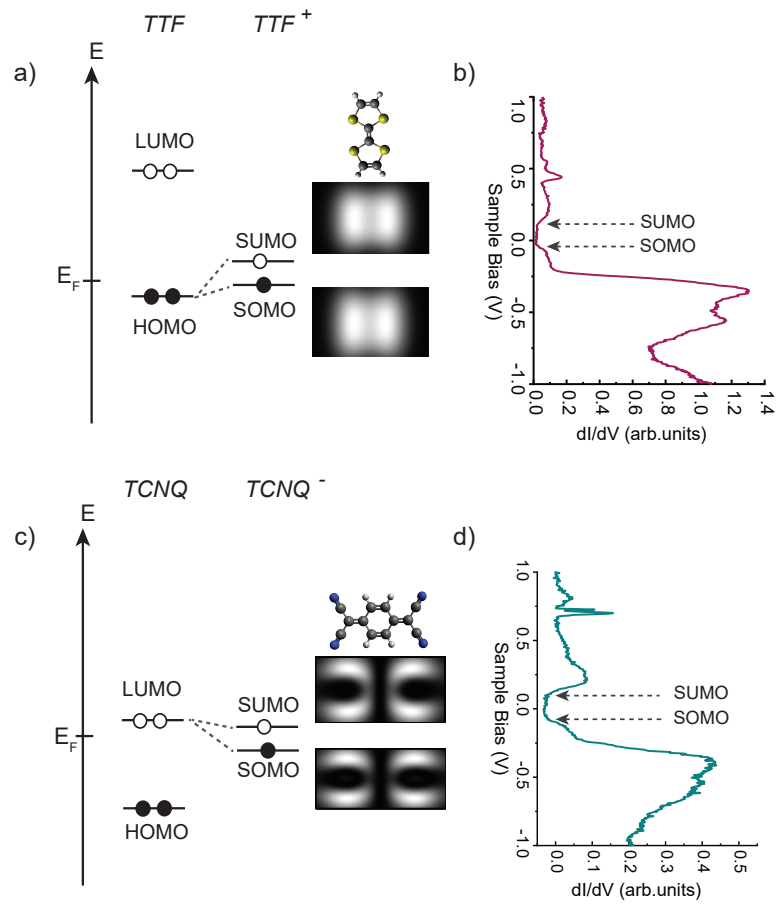
Figure 7.8: Energy level diagram of molecular orbitals for TTF and TCNQ. **a)** Donating one electron, TTF HOMO converts to one singly occupied and one singly unoccupied molecular orbitals. **b)** An exemplary spectra of the set shown in Fig. 7.6e (feedback opened at V = 1V, I = 75 pA with V$_{mod}$ = 10 mV). The SOMO and SUMO states are located at - 60 mV and 140 mV, respectively. **c)** Gaining one electron, TCNQ LUMO splits into one singly occupied and one singly unoccupied molecular orbitals. **d)** An exemplary spectra of the set shown in Fig. 7.6b (feedback opened at V = 1V, I = 75 pA with V$_{mod}$ = 10 mV). The SOMO and SUMO states are located at - 115 mV and 145 mV, respectively. The simulated constant-height conductance maps are shown on the right panels of **a)** and **c)**. These have been used to calculate the tunnelling matrix element M$_{ts}$ with an s-wave tip at a tip-molecule distance of 7.5 Å and a workfunction of 5 eV.

For a complete proof, we would need to see the same feature at negative bias, but we lack a nicely resolved image.

Generally, we may attribute the variation of the SOMO and SUMO energies (the variation of the onsets) to the effect of the SL-MoS$_2$ moiré pattern. In chapter 5, the dI/dV spectra taken on top and hollow site of MoS$_2$ moiré showed a shift of $\sim$ 130 mV toward the VB and a shift of $\sim$ 50 mV away from the CB of MoS$_2$. However, because we cannot identify the moiré pattern through the mixed structure (see Fig. 7.4b), we cannot completely correlate the variation of the SOMO and SUMO to the variation of the MoS$_2$ band gap on top and hollow site of the moiré.

For the smaller variation of the onsets in the case of alternating TTF-TCNQ rows, we may anticipate that the CT between TTF and TCNQ will become more dominant over the influence of MoS$_2$. Moreover, the intermolecular interaction (in the form of CT) between the alternating TTF-TCNQ row seems stronger than the interaction between the row consisting of only TTF molecules or TCNQ molecules.

II) Tip-induced charge transfer

To investigate the origin of the observed sharp peaks, we consider the tunnelling via a double-barrier tunnelling junction (DBTJ). As we studied in chapter 3, in the DBTJ the applied voltage drops between tip - adsorbate and between adsorbate-metal across MoS$_2$. Molecular levels are not fixed and they can shift with respect to the Fermi level of the tip or sample depending on the applied bias voltage. We note that in our DBTJ, the biggest part of the voltage drop is still between the tip and the molecule. In such a junction, the sharp resonance occurs when one of the molecular orbitals is pulled across the Fermi level of the sample due to the voltage drop across the decoupling layer [63, 72]. Depending on which molecular orbital (empty or filled) aligns with the Fermi level of the sample, molecules can be positively or negatively charged.

In our system, the SOMO and the SUMO of both TTF and TCNQ are near the Fermi level and fulfill the conditions for sharp resonance to occur (positively or negatively charged molecule). Fig. 7.9 illustrates the energy diagram of such a DBTJ with SUMO and SOMO levels relative to the Fermi level. The applied voltage drops within the vacuum barrier and MoS$_2$ layer. When no bias is applied (Fig. 7.9a) the Fermi level of the tip and sample are aligned and we have SOMO and SUMO states, singly occupied and unoccupied, respectively. Applying a small positive bias (Fig. 7.9b), the tip's Fermi energy shifts up with respect to the molecular resonances. Consequently, the molecular resonances also shift with respect to the sample states due to the small barrier between molecule and sample. Therefore, at some threshold, tunnelling occurs via the SUMO resonance of the molecule which is detected as a broad resonance in the dI/dV spectrum. By increasing the bias voltage (Fig. 7.9c), the SOMO level is pulled up above the Fermi level of the sample. The electron of the SOMO is transferred to the sample, the charge state of the molecule is increased by +1 (one electron less in the system). In spectroscopy,

this event is observed as a sharp resonance. Due to the smaller tunnelling barrier between the molecule-Ag surface compared to the molecule-tip, tunneling from the molecule to the sample (emptying SOMO) is much faster than the filling of the SUMO.

The situation when the sample bias is negative is depicted in Fig. 7.10. When no bias is applied (Fig. 7.10a) the Fermi level of the tip and sample are aligned. At a small negative bias (Fig. 7.10b), the tip Fermi level and the molecular resonances pull down, tunnelling occurs via the SOMO level and a broad peak will appear in the spectroscopy. When the bias voltage increase (Fig. 7.10c), the SUMO level crosses the Fermi level of the sample, the electron within the SUMO is transferred to the tip and the charge state of the molecule is decreased by -1 (one electron more in the system). In spectroscopy, this event is observed as an abrupt change in the conductance as a sharp resonance. Due to the smaller tunnelling barrier between molecule-surface compared to the molecule-tip, tunneling from sample to the molecule (filling SUMO) is much faster than tunneling through the SUMO state.

As we have mentioned earlier, the observation of sharp peaks (so-called *charging peaks*) in the dI/dV spectra at different energies are linked to the energy position of the onsets in the opposite bias. Here, the voltage drop across the decoupling barrier plays an important role. To find the ratio of the voltage drop (α) which occurs within MoS_2, we apply equations (3.1) and (3.2) to our case in Fig. 7.7c. For the red spectrum, we have $|V_s|=|650$ meV/e$(\alpha$ -1)$|$ and V_s=65 meV/eα, therefore, α=10 %. Similar calculations for the blue spectrum, $|V_s|=|113$ meV/e$(\alpha$ -1)$|$ and V_s=17 meV/eα results in α=15 %. The difference between this two values of voltage drops calculated above, may be due to the precision of the determination of the onsets. In particular, in the latter with an onset at 17 mV and a precision of $\pm$ 10 mV (our energy resolution), the calculated voltage drop may vary from 6 to 18%. Finally the

Figure 7.9: Tunnelling process through double-barrier junction. Here the decoupling layer (MoS_2) is implemented between adsorbate and the sample. **a)** At zero bias, the Fermi levels of sample and tip are aligned. **b)** At positive sample bias, transport occurs via SUMO state of the adsorbate. **c)** At higher bias, SOMO state passes Fermi level of the sample and the adsorbate will be charged.
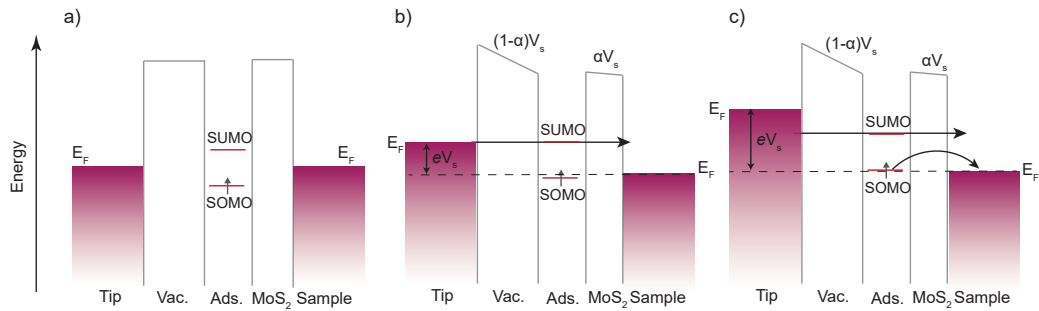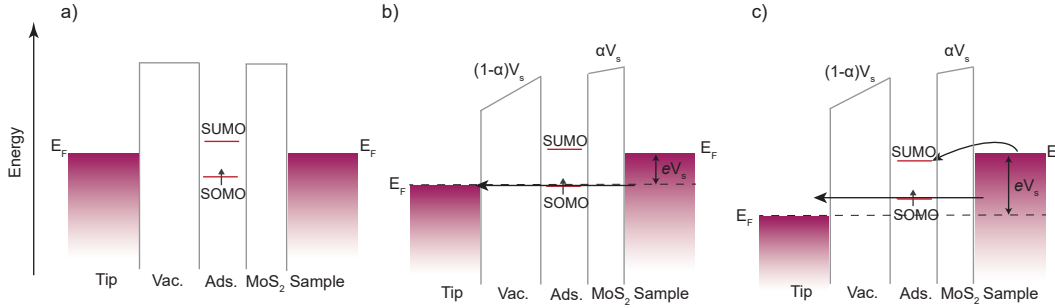
Figure 7.10: Tunnelling process through double-barrier junction. Here the decoupling layer (MoS_2) is implemented between asdorbate and the sample. **a)** At zero bias, the Fermi levels of sample and tip are aligned. **b)** At negative sample bias, transport occur via SOMO state of the adsorbate. **c)** At higher negative bias, when SUMO state crosses tip's Fermi level, the adsorbate will be charged.

range of voltage drop we determine (10-15)%. This range of value has been found for MoS_2 on Au surface in former works [19, 77] as we mentioned in chapter 3. In Fig. 7.6d we mentioned that we observe a sharp peak in red spectrum but not in the orange one. When we take into account the voltage drop of $\sim 10\%$ in Sl-MoS_2 as calculated for the case in Fig. 7.7, we would expect to have a sharp resonance at 1.9 V (which is out of our energy range) when the onset is at -190 mV. Considering the voltage drop of $\sim 15\%$ in Sl-MoS_2, the charging peak would expect to appear at 1.26 V which is also out of our energy window.

We have mentioned above that in the false-color plot dI/dV spectra , the charging events appear as parabola, i.e the (absolute) voltage required to have the tip- induced charging of the molecule increases when the tip is moved away from the molecule. This is a direct consequence of the inhomogenous electric field induced by the tip as we explained in chapter 3. When the tip is located on top of the molecule the iso-contours of the electric field are circles on the surface. As the tip goes far away (at the certain height), the molecule feels less electric field due to the increase of (lateral) distance. However, the molecule still can be charged only if an adequate voltage is applied. When the tip moves above the molecule and the bias sweeps, the dispersion of the tip's field at the molecule will appear as a parabola. Here, in our system we observe several parabolas as shown in Fig. 7.11b as an exemplary case. Because we have a layer of molecular assembly, when the tip moves along the line, it can charge more than one molecule, not only molecules along the line but also neighbouring molecules as shown in Fig. 7.11a. Therefore, due to multicharging (charging more than one molecule) several parabolas appear in our false-color plot. We have noted previously that the charging peaks' energies are associated to the onsets of conductance at opposite bias side. As the onset of conductance in negative bias is closer to the Fermi energy, the charging peak appears closer to Fermi energy at positive bias as well. This can explain having parabolas' vertex at different energies. Another feature of the
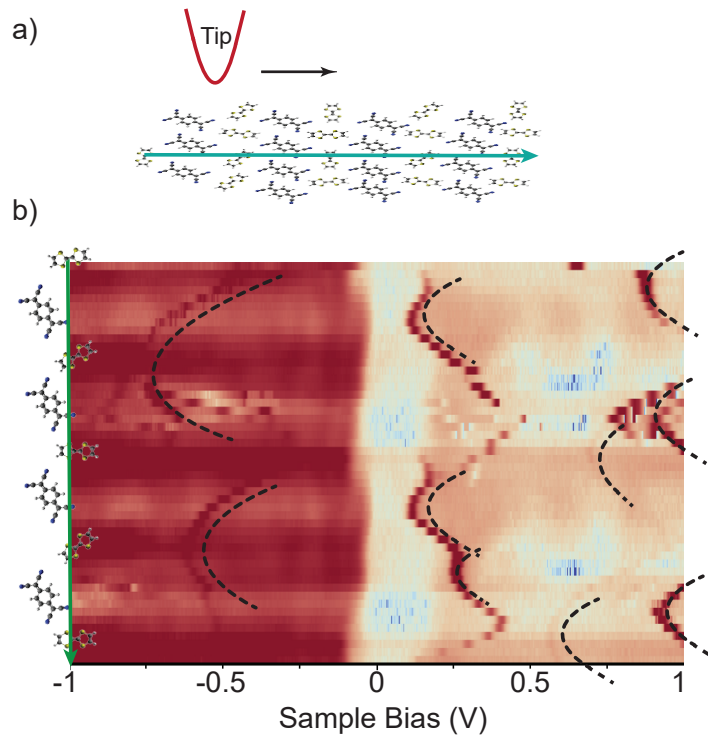
Figure 7.11: **a)** Side view of TTF-TCNQ line, where the tip is sweeping in constant height it affects on molecules along the line as well as their neighbouring molecules. **b)** False-color plot dI/dV spectra taken along the green line (7.8 nm) shown in **a)** (feedback opened at V = 1 V, I = 75 pA with V_{mod} = 10 mV). Dashed-parabolas are displaying different parabolas in the plot.

parabolas here is that they appear asymmetric (or half parabolic). Instead of single molecule, we have some molecular island with a strong intermolecular interactions (through aforementioned permanent CT), which determined the energy levels of the system.

With the tip-induced charging effect, we modify locally the charge states and thus, the energy of the molecular states. Therefore, such processes (the tip-induced charging effect) may also modify the interaction (permanent CT) with the neighbouring molecules. In other words, with such CTC, we have a strong interplay between different charge transfer processes. Therefore, correct physical description of the tip-induced charging may be much more complex than how charging of one single molecule (and the nicely parabolic charging dispersion) is usually described. At negative bias, the parabolas are associated to the states near Fermi at positive bias. However, their direction is not in agreement with the explanation of enlarging parabola (or charging ring) size with increasing the bias voltage for the case of one molecule. Here, we also suggest that having molecular island could affect the

dispersion of parabolas for one molecule which has different neighbours.

7.3 Conclusion

We explained the deposition of TTF-TCNQ compound on MoS_2/Ag(111) surface. The result was the formation of pure TCNQ island, mixed structures composed of alternating arrays of TFF and TCNQ and occasionally pure TTF island. First, we resolved the HOMO resonance of the TTF molecule in the pure self-assembled island. Using Franck-Condon picture, we find a good agreement between experimental and simulated spectra to find the fingerprints of the vibronics of the TTF molecule on MoS_2/Ag(111).

Then, we have characterized the electronic properties of a charge transfer complex (CTC) composed of TTF and TCNQ on MoS_2/Ag(111). Due to the donor character of TTF and acceptor character of TCNQ, one electron was transferred from TTF to TCNQ. We performed dI/dV spectra along both TTF and TCNQ lines in the mixed structure. Two features were found that were not observed neither on pure TTF nor on pure TCNQ islands. First we observed states close to Fermi level, secondly some parabolas were detected at both polarities.

Two charge transfer mechanisms could explain the observation of the narrow energy gaps and the sharp peaks. The narrow energy gaps are the consequence of the static charge transfer. Due to the small energy gap of TTF (HOMO) and TCNQ (LUMO) the charge transferred from the donor TTF to the acceptor TCNQ. This shifts up the TTF (HOMO) and shifts down the TCNQ (LUMO), these states crossed the Fermi level and split into two states: singly occupied and unoccupied molecular orbitals, SOMO and SUMO respectively. The experimental identification of the SOMO and the SUMO is the topography image scanned at 0.3 V, where we observed HOMO of TTF and LUMO of TCNQ.

The other mechanism is tip-induced charge transfer which requires two conditions: having a double barrier tunnelling junction and a state near the Fermi level. In our case, employing SL-MoS_2 on Ag(111) fulfills the first condition and having SOMO and SUMO states fulfills the second requirement.

Structural and Electronic Properties of DCV5T–Me$_2$ and C$_{60}$ on MoS$_2$/Ag(111)

In this chapter we aim to study another electron donor and acceptor molecules. Using scanning tunnelling microscopy (STM) and scanning tunnelling spectroscopy (STS), we investigate the electronic interaction between methyl-substituted dicyanovinyl (DCV5T-Me$_2$) molecule and C$_{60}$ molecule on single-layer molybdenum disulfide (SL-MoS$_2$) on Ag(111). Generally, dicyanovinylene-substituted oligothiophene (DCVnT, where n represents the number of thiophene rings) molecules are extensively used in the field of organic solar cells [173–181]. DCVnT contains both electron donor (thiophene) and acceptor (DCV groups) moieties. The combination of donor and acceptor units in these A-D-A oligothiophenes has been found promising in photovoltaic devices [182]. DCVnTs act as electron donors in organic solar cells when they combine with C$_{60}$, because of their lower electronegativity. DCV5T and C$_{60}$ provide the efficiency of 4% in solar cells which is higher than the value found in DCV3T (1.3%) and DCV4T (2.3%) [182].

Similar to the previous chapters, here we also use SL-MoS$_2$ as a decoupling layer which facilitates investigating the intrinsic electronic structure of molecules [19]. First, we investigate self-assembled two-dimensional islands formed by either C$_{60}$ or DCV5T-Me$_2$ molecules. Spectroscopic measurements within the molecular islands allow us to resolve the electronic structure of both molecules energetically and spatially. Depositing both molecules on the MoS$_2$ layer still leads to homo-molecular islands. However, at their interface, in some cases C$_{60}$ locates on top of DCV5T-Me$_2$ which leads to an upward shift of the resonance compared to C$_{60}$ on MoS$_2$.

8.1 DCV5T-Me$_2$ Molecule

As shown in Fig. 8.1a, DCV5T-Me$_2$ molecule is composed of a central electron-rich quinquethiophene (5T) backbone with two terminal electron deficient dicyanovinyl (DCV) groups linked symmetrically, and two methyl (Me$_2$) substitutions in the central

63

a)   trans-trans-trans-trans (t-t-t-t)

b)   cis-trans-trans-cis (c-t-t-c)
each rotation costs: 8 meV

c)   cis-cis-cis-cis (c-c-c-c)
each rotation costs: 79 meV

d)   two-DCV rotations
each rotation cost: 69 meV
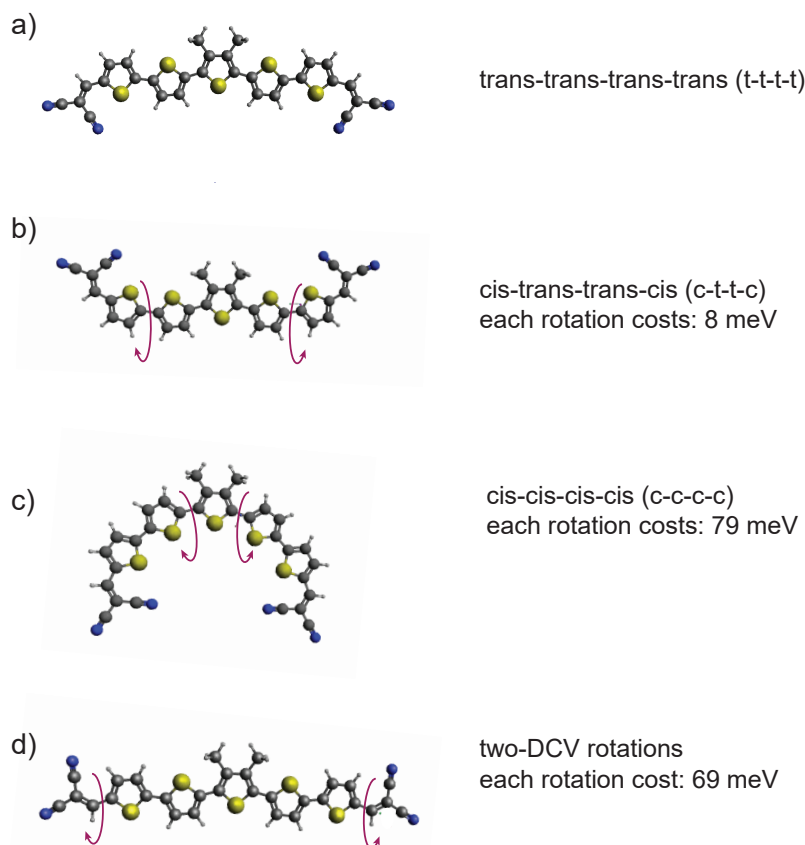
Figure 8.1: Top view of the stick-and-ball DCV5T-Me$_2$ rotamers in gas phase. Gray spheres represent C atoms, white spheres H atoms, yellow S atoms and blue N atoms. **a)** The most favorable conformation due to the minimum energy, **b)-d)** Three different conformations (rotamers) with the cost of each thiophen's rotation. Red arrows show the rotations between C-C bonds. To simulate molecules geometry and calculate their energies we use Universal Force Field (UFF) and Avogadro software.

thiophene ring. The molecule is planar and can adapt different types of rotamers due to the various orientations of thiophene rings and DCV groups. Four of the rotamers are shown in Fig. 8.1(a-d) as trans-trans-trans-trans (t-t-t-t), cis-trans-trans-cis (c-t-t-c), cis-cis-cis-cis (c-c-c-c) and two-DCV rotations, respectively. The latter is basically the t-t-t-t rotamer with the rotation of both DCVs. The notations cis (c) and trans (t) describe the relative positions of S atoms with respect to C-C single bonds. Fig. 8.1(b-d) also shows the calculated energy difference (rotation cost) for each rotamer with respect to the energy of t-t-t-t conformation.

Different rotamers were found in other thiophene-based polymers on Au(111) [19, 183, 184] and in single molecular chains of π-conjugated polymers such as polythiophene and polydiacetylene [185]. Universal Force Field (UFF) and DFT

Figure 8.2: STM image of DCV5T-Me$_2$ molecules on MoS$_2$ and on Ag(111) deposited at 120 K, recorded at V = 0.7 V, I = 20 pA. Molecules mainly distribute on the Ag(111) surface and a small fraction of them remain on MoS$_2$.

calculations suggest the lowest total energy is the t-t-t-t configuration [179] as depicted in Fig. 8.1a. The least favo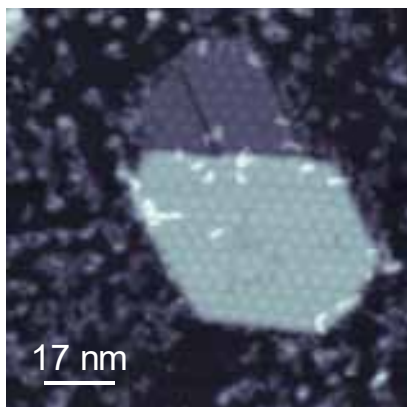rable configuration is c-c-c-c (Fig. 8.1c), because of the highest total energy (maximum energy difference to trans conformation). The energy difference for the c-c-c-c with respect to the t-t-t-t conformation is calculated 97 meV. In the literature, the energy difference between cis-trans conformers in bithiophen is estimated from 8 meV to 50 meV [186]. In our case, from trans (Fig. 8.1a) to c-t-t-c (Fig. 8.1b) the calculated low energy fits with the literature value. However, the rotation costs more from t-t-t-t (Fig. 8.1a) to c-c-c-c (Fig. 8.1c). The reason which makes c-c-c-c the least favorable rotamer (with high C-C rotation cost) can be explained via steric effects. Steric repulsion refers to the arrangement of the atoms in the molecule. It arises due to the fact that each atom within a molecule occupies a certain space and when atoms are brought too close together, overlapping electron clouds (Pauli repulsion) may hinder some conformations and favor others. In the c-c-c-c conformation, hydrogens in the methyl groups (central ring) are reluctant to be close to the hydrogens of the neighbouring thiophene rings, which makes the c-c-c-c conformation less favorable.

8.2 Growth and Structural Properties DCV5T-Me$_2$ on MoS$_2$/Ag(111)

After depositing DCV5T-Me$_2$ molecules on a partially MoS$_2$-covered Ag(111) surface at 120K for 15 minutes, the molecules mostly stick to the Ag(111) surface and a small fraction of them remain on MoS$_2$ islands as shown in Fig. 8.2. The high-resolution STM image in Fig. 8.3a shows that single DCV5T-Me$_2$ molecules disperse on MoS$_2$
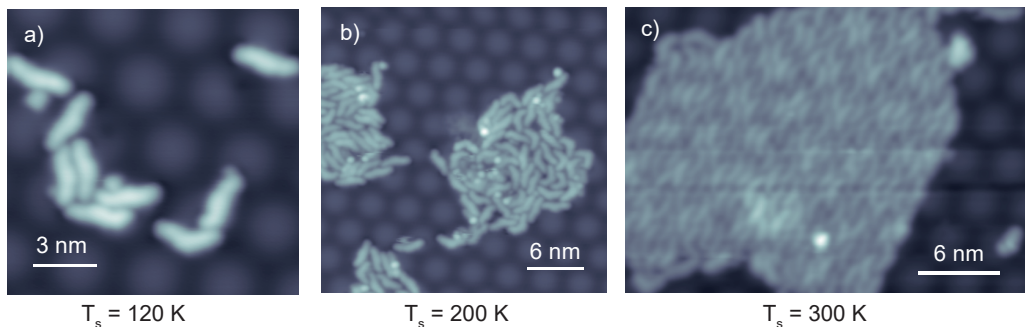
Figure 8.3: STM topography of DCV5T-Me$_2$ molecules on MoS$_2$/Ag(111) **a)** deposited at 120 K sample temperature. **b)** deposited at 200 K sample temperature. **c)** post-annealed at 300 K (all images are recorded at V = 0.7 V, I = 20 pA). Due to the rotation of thiophene rings, molecules appear in various conformations in **a)** and **b)**. Post annealing at room temperature leads to the large island where all molecules take the same conformation.

in various conformations ascribed to different rotations of thiophene rings and DCV groups as mentioned above.

Due to the weak adsorption of molecules on MoS$_2$, the surface temperature during molecular deposition has a determining role in the formation of supramolecular structures. Here, to grow larger molecular assemblies, we have grown large islands of MoS$_2$ on Ag(111) as explained in chapter 5. Adsorption of DCV5T-Me$_2$ on MoS$_2$/Ag (111) at 200K for 15 minutes leads to small disordered assemblies of DCV5T-Me$_2$ (Fig. 8.3b) in which each molecule within the islands adapts a different conformation. Due to the formation of molecular islands and having large MoS$_2$ zones, molecules diffuse less on the metal surface. Post-annealing the sample to room temperature influences the molecular arrangement and results in the formation of large, well-ordered and self-assembled molecular islands as shown in Fig. 8.3c. We have seen a similar behavior in chapter 6, when depositing TCNQ on MoS$_2$/Ag(111): the higher the temperature, the larger are the molecular islands we obtain.

In Fig. 8.4(a-d), we show different molecular shapes with the proposed superimposed conformation of DCV5T-Me$_2$. We observe the most favorable conformation (t-t-t-t) in Fig. 8.4a and the least favorable (c-c-c-c) in Fig. 8.4b. The rotamer with two-DCV rotations is shown in Fig. 8.4c, in Fig. 8.4d the lower molecule is a t-t-t-t and the upper one a c-t-t-c conformation. Although trans rotamer is the most commonly found arrangement, we also observe few cis arrangements. When we compare the rotation energies (see Fig. 8.1) to the thermal energy (~ 50 meV) during evaporation at 260 °C, molecules can take various conformations in gas phase. When they arrive at the cold surface, they stay as they were in vapor.

Post-annealing of the sub-monolayer coverage of DCV5T-Me$_2$ results in predominantly two types of extended self-assembled structures with tens of nanometers in size (Fig. 8.5a and b). Higher resolution STM images of both kinds of assemblies with

the superimposed molecular model are shown in Fig. 8.5c and d, which are labeled as type I and type II, respectively. All molecules appear with the same conformation (t-t-t-t rotamer) in ordered island type I as well as type II. As mentioned above the calculation shows that this conformation (see also Fig. 8.1a) corresponds to the minimum energy for the molecule in gas phase [187].
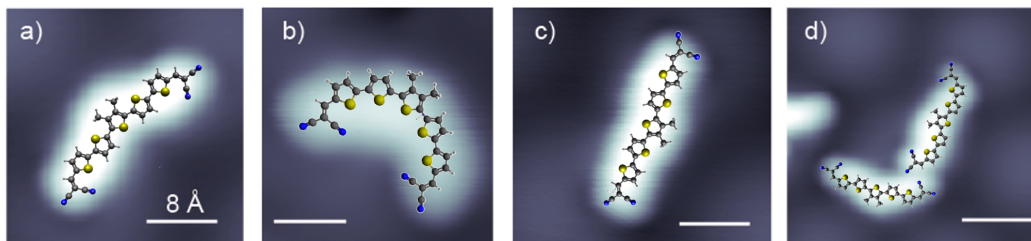

Figure 8.4: STM image of DCV5T-Me$_2$ molecules on MoS$_2$/Ag(111) with different configurations deposited at 120 K sample temperature, recorded at V = 0.7 V, I = 20 pA, all scale bars are 8Å. Models of the different configuration are superimposed. **a)** t-t-t-t conformation, **b)** c-c-c-c conformation, **c)** two-DCV rotations conformation and **d)** (top) c-t-t-c and (low) t-t-t-t conformations.

Island type I (Fig. 8.5c) shows that the DCV moieties contact the center of neighbouring molecules. Fig. 8.5e shows the zoomed-in STM image, where close located CN ligands and CH groups form hydrogen bonds (indicated by the red lines). Another interaction which contributes to the formation of the islands is the intermolecular S-N electrostatic interaction (green lines in Fig. 8.5e). This conformation and assembly of DCV5T-Me$_2$ in islands as well as in chains was already seen on a Au(111) surface in former works [187, 188]. In the island type II (Fig. 8.5d), all molecules take the same conformation as in island type I, albeit in very different bonding motives to the neighbours. All molecules are parallel to each other and each molecule connects to the adjacent molecules via their DCV ends. In addition to the usual intermolecular van der Waals interaction, here the hydrogen bonds between CN ligands and CH groups (red lines in Fig. 8.5f) are also responsible for the molecular assembly. Apart form different bonding motives in the islands type I and II, the islands also have different packing density. The island type I is more densely packed (0.45 molecule/nm^2) compared to the island type II (0.35 molecule/nm^2) which leads to a different total energy. In the next section we compare the electronic features in these islands.

We note that the moiré reconstruction underneath the molecular islands stays intact which indicates weak interaction between molecules and surface, as already observed in chapter 6 for TCNQ molecular islands on MoS$_2$.
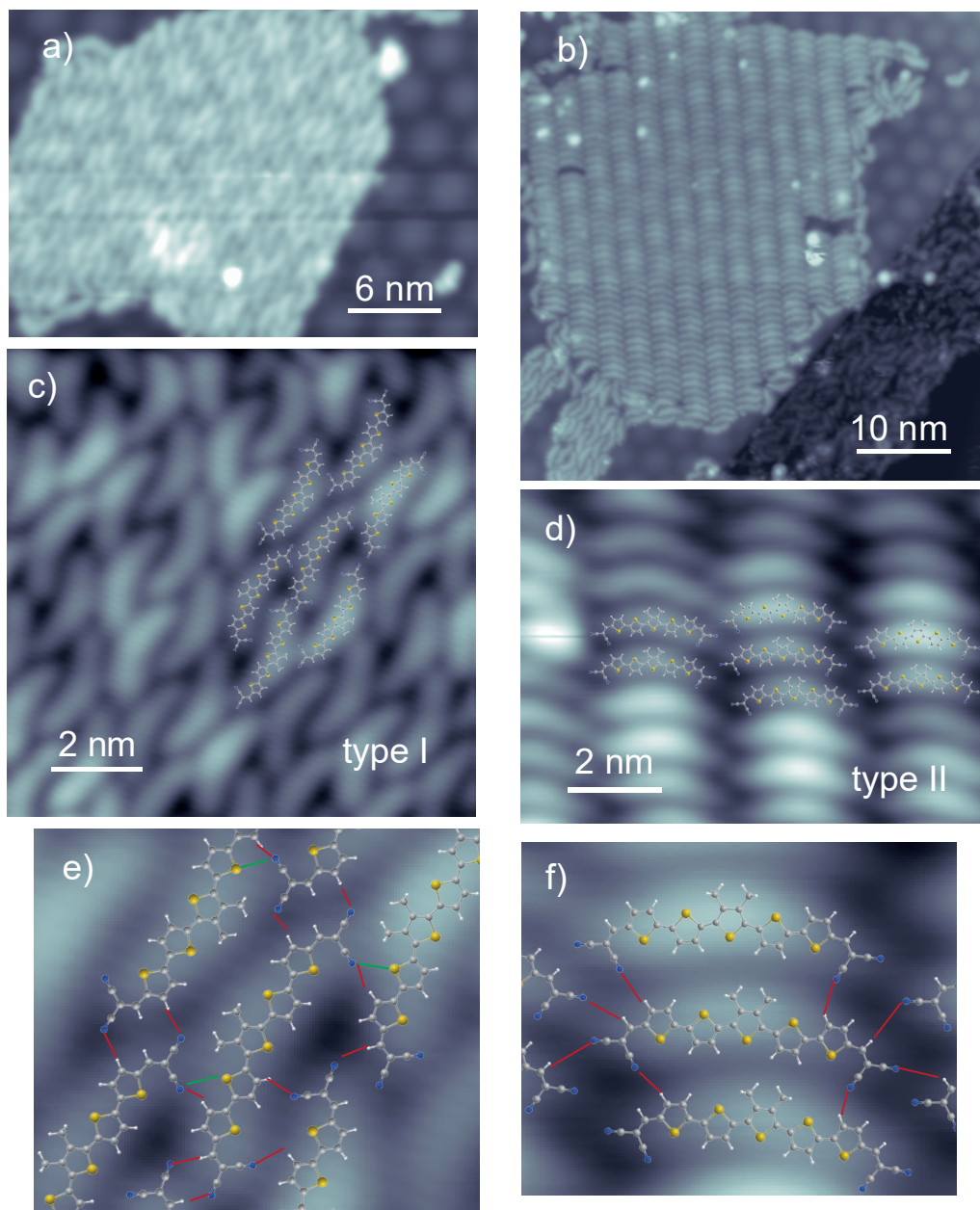
Figure 8.5: STM topography of DCV5T-Me$_2$ on MoS$_2$ deposited at 200 K and post annealed at 300 K. **a)** and **b)** show two types of molecular islands scanned at V= 0.7 V and I= 20 A. **c)** and **d)** show high-resolution images of the islands of **a)** and **b)** with superimposed molecular structures. In **c)** type I, DCV moieties of each molecule connect to the center of neighbouring molecules and in **d)** type II, each molecule connects to the adjacent molecules via their DCV ends. **e)** The bonding model is superimposed and shown hydrogen-bonds (red lines) with bonding length from 0.51 nm to 0.89 nm and S-N bonds (green lines) with the average bonding length of 0.94 nm. **f)** The superimposed bonding is illustrated in CN ligands and CH groups via hydrogen bonds (red lines) with bonding length from 0.71 nm to 1.16 nm.
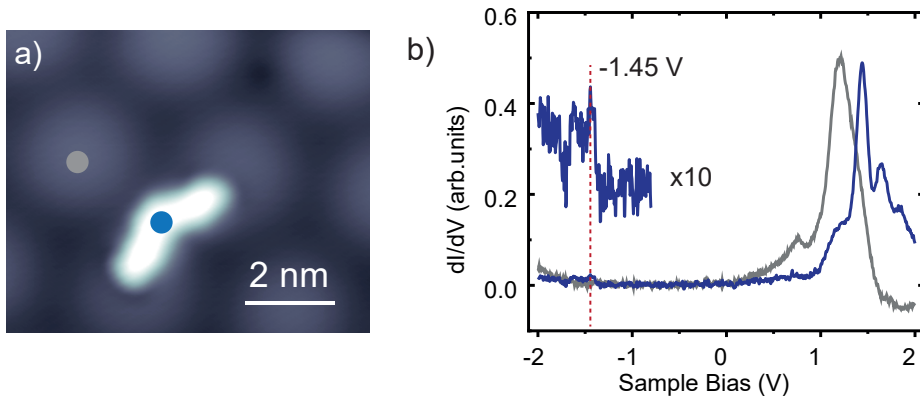
Figure 8.6: **a)** STM image of a single DCV5T-Me$_2$ molecule on MoS$_2$/Ag(111) scanned at V=0.7 V, I=20 pA. **b)** Constant-height dI/dV spectrum acquired on the center of the molecule (blue) and on the MoS$_2$ (gray) (set point: I =75 pA, V =2 V with V$_{mod}$ =10 mV).

8.2.1 DCV5T-Me$_2$ on MoS$_2$/Ag(111): Electronic Properties

As explained in the previous section, different sample temperatures during the deposition, lead to different DCV5T-Me$_2$ assemblies (single molecules, disordered and ordered islands) on the MoS$_2$/Ag(111). This allows us to investigate the electronic properties of DCV5T-Me$_2$ in various environments, using STS. To inspect the electronic properties of DCV5T-Me$_2$ molecules, first we measure spectra on isolated molecule on MoS$_2$. Differential conductance spectra (Fig. 8.6b) acquired on the center of the molecule (Fig. 8.6a- blue dot) reveal several resonances in the unoccupied states outside of the MoS$_2$ gap. At positive sample bias an onset shoulder at 1V and three pronounced resonances at 1.43 V, 1.64 V and 1.81 V are observed. At negative sample bias, the first resonance is seen at -1.45 V. Due to the instability of the single DCV5T-Me$_2$ molecule on MoS$_2$, finding the origin of these resonances via dI/dV map is not possible. Thus, to overcome the instability of single DCV5T-Me$_2$ on MoS$_2$, we measure conductance spectra of molecules which are stabilized by their environment. First, we record spectroscopy on molecules in a disordered island (inset Fig. 8.7a) where the molecules appear in diverse configurations.

Fig. 8.7a (inset) shows a small and disordered molecular assembly with the corresponding STS spectra. In Fig. 8.7b, although other conformations may fit, we propose the conformations of (c-t-t-t) and (one-DCV rotation) for the blue and orange molecule, respectively. At positive bias in Fig. 8.7c, we observe that the orange spectrum has a shoulder at 1.26V and a resonance at 1.46V and the blue spectrum has a resonance at 1.25V. At negative bias (see Fig. 8.7d), there are resonances at -1.28V and -1.41V for the orange and blue spectra, respectively. At positive bias, the shoulder of the orange spectrum seems to fit with MoS$_2$ resonance. Hence, we observe a gap of
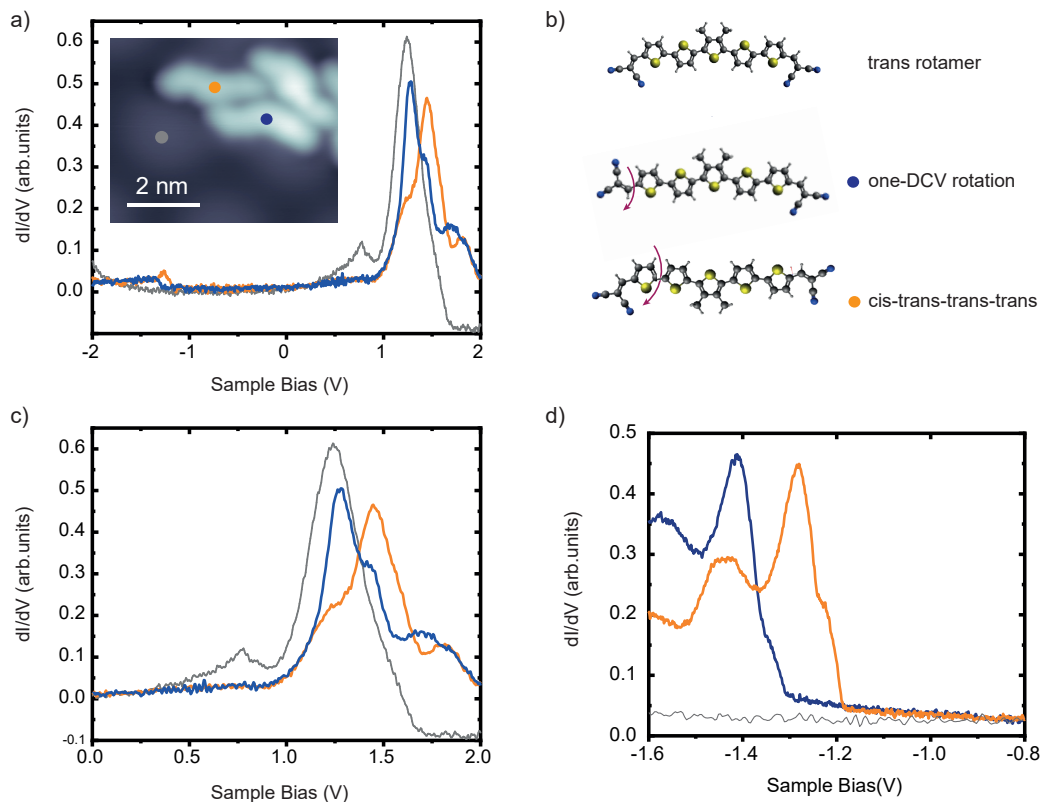
Figure 8.7: **a)** Constant-height dI/dV spectra recorded on the center of randomly oriented DCV5T-Me$_2$ molecules on MoS$_2$/Ag(111), the inset shows the STM topography (set point: V = 2V, I = 75 pA, V$_{mod}$ = 10 mV). STM image of molecules on MoS$_2$/Ag(111) scanned at V = 0.7 V, I = 20 pA, **b)** Molecules with (c-t-t-t) and (one-DCV rotation) configurations. **c)** Zoomed-in spectra from **a)** at positive bias. **d)** Constant-height dI/dV spectra in the occupied states acquired on the center of the molecule (set point: I = 75 pA, V = -1.6 V with V$_{mod}$ = 5mV). The gray spectrum is the reference spectrum on MoS$_2$.

2.73V for the orange molecule and 2.66V for the blue one. We also observe a shift of $\sim$ 200 mV and $\sim$ 130 mV for the orange and blue resonances at positive and negative bias, respectively. Krane *et al.* [19] observed a shift in the resonance at negative bias for two rotamers of 2,5-bis(3-dodecylthiophen-2-yl)thieno[3,2-b]-thiophene (BTTT) molecules on MoS$_2$/Au(111). Therefore, the shift in the resonances could be the signature of the different conformations but cannot be completely disentangled from the effect of the different environments such as different bondings with neighbours and different adsorption site. We also find a smaller gap size compared to the gap of the single molecule (see Fig. 8.6) because of the screening effect of the neighbour molecules [66]. Due to the molecules instability on the surface, investigating the origin of the resonances via dI/dV maps is not achievable. In the following, we discuss

about the origin of the resonances in the large and organized molecular assembly.

Now, we probe the electronic properties of DCV5T-Me$_2$ molecules in an ordered island. We acquire conductance spectra at the center of molecules within the organized island type II (inset Fig. 8.8a). In the unoccupied states, STS reveals resonances at 1.4 V, 1.8 V and an onset at 2.5V (Fig. 8.8a). The constant-height dI/dV spectra in the occupied states (Fig. 8.8b) reveal a sharp onset of conductance at -1.4 V which is accompanied by satellite equidistant (200 mV) peaks.

To elucidate the origin of each resonances, constant-height dI/dV maps (spatial distribution of dI/dV signals) are recorded at the corresponding energies and are shown in Fig. 8.9(a-d). Fig. 8.9a shows the differential conductance (dI/dV) map recorded at -1.4 V. The signals appear intense on the terminations of the molecule and a nodal plane is seen at the center. In Fig. 8.9b, the map recorded at 1.4 V shows no nodal plane and the delocalized distribution is seen over the whole molecule. In the map acquired at 1.8 V (Fig. 8.9c), the spatial distribution is less intense in the center, and lastly the map taken at 2.5 V (Fig. 8.9d) exhibits dI/dV signal mainly located over the center of the molecule.

In order to identify the molecular orbitals, we compare the dI/dV maps with the calculated shape of the gas-phase molecular orbitals. We first calculate the gas-phase electronic structure using density-functional-theory calculations with the B3PW91 functional and the 6-31g(d,p) basis set as implemented in the GAUSSIAN09 package [47]. The calculated energy-level diagram of DCV5T-Me$_2$ molecule with the corresponding iso-density contour plots of the highest occupied molecular orbital (HOMO) and some of the lowest unoccupied orbitals are illustrated in Fig. 8.9e. We also simulate the position-dependent tunnelling matrix elements between the s-wave tip and the spatially-resolved molecular wave function across the DCV5T-Me$_2$ molecule [43]. The maps of the squared tunnelling matrix elements are depicted as insets in Fig. 8.9(a-d). Simulation reveals that the LUMO/LUMO+1 can be distinguished unambiguously by the absence/presence of the nodal plane in the center of the molecule.

Supported by calculations, we assign the peak at -1.4 V to the removal of an electron from the highest occupied molecular orbital (HOMO). The HOMO resonance is accompanied by satellite peaks as we mentioned previously. The peak at -1.6 V cannot be attributed to the HOMO-1 because the DFT calculates the energy distance of 700 meV between HOMO-1 and HOMO, whereas Fig. 8.8c shows the energy distance of 200 mV. Therefore, we suspect the satellite peaks are vibronic peaks and we clarify this in the following. The absence/presence of the nodal plane in the experimental constant-height dI/dV map recorded at 1.4 V and 1.8V is in good agreement with the tunnelling matrix element simulations of LUMO and LUMO+1. Therefore, the peak at 1.4 V corresponds to LUMO and the peak at 1.8 V is attributed to LUMO+1. The last map recorded at 2.5 V agrees with the matrix element simulation where the spatial distribution of the LUMO+2 is mainly localized in the center of the molecule. The width of the LUMO resonances is $\sim$ 200 mV (Fig. 8.8b) which is smaller than the LUMO width on Au(111) [188] as a consequence of less hybridization here with the surface using MoS$_2$.
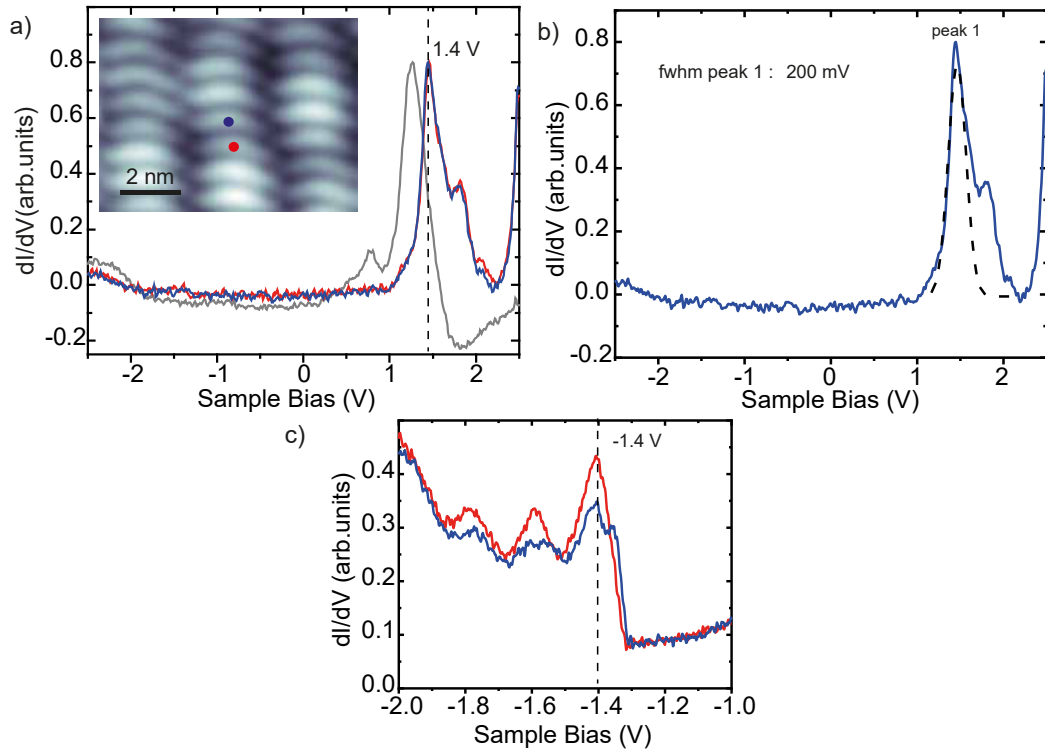
Figure 8.8: **a)** Constant-height dI/dV spectra recorded on the center of DCV5T-Me$_2$ molecules (within a well-ordered island) on MoS$_2$/Ag(111) as shown in the inserted STM topography (set pint: at V = 2.5V, I = 100 pA, V$_{mod}$ = 10 mV). STM image of molecules on MoS$_2$/Ag(111) scanned at V=1 V, I=20 pA. **b)** The spectrum from **a)** with the width of 200 mV for the first peak and 270 mV for the second peak. **c)** Constant-height dI/dV spectra in the occupied states acquired on center of the molecule (set point: 30 pA, -1 V with V$_{mod}$= 2mV).
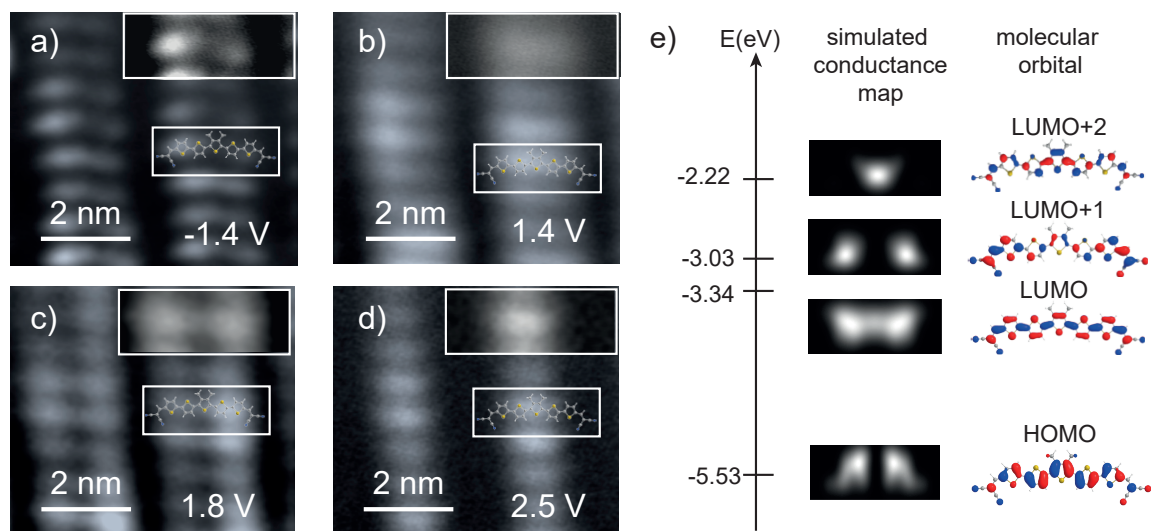
Figure 8.9: **a-d)** Constant-height dI/dV maps of the parallel arrangement DCV5T-Me$_2$ island (type II) on MoS$_2$ recorded at the resonance energies derived in Fig. 8.8. Feedback opened on top of the molecule at **a)** V = -1 V, I = 30 pA; **b)** V = 1.4 V, I = 20 pA; **c)** V = 1.8 V, I = 50 pA; **d)** V = 2.5 V, I = 20 pA with V$_{mod}$ = 5mV. **e)** Energy-level diagram of DCV5T-Me$_2$ determined from gas-phase DFT calculations (left). The isosurfaces of the frontier molecular orbitals are shown on the right. These have been used to calculate the tunnelling matrix element M$_{ts}$ with an s-wave tip at a tip–molecule distance of 7.5 Å, workfunction of 5 eV. The map of the spatial distribution of $|M_{ts}|^2$ is shown in the middle panel.

As mentioned previously, there are two types of self-assembled DCV5T-Me$_2$ molecular islands on MoS$_2$/Ag(111). Although all molecules take the same bent configuration in both islands, the number of neighbours and bonding are different as discussed before. To inspect if this would affect the electronic structure, we compare the dI/dV spectra of two molecules within the two islands. Fig. 8.10a and b illustrate the molecular islands as we described in previous section. A dI/dV spectrum (Fig. 8.10c - orange spectrum) on the molecule in the island type I, shows the HOMO and LUMO resonances at -1.2V and 1.3V, respectively. While the dI/dV spectrum (Fig. 8.10c - red spectrum) on the island type II shows the HOMO and LUMO resonances at -1.4V and 1.4V. Hence, the gap for organized island type I (Fig. 8.10b) is 300 mV smaller compared to the gap in organized island type II (Fig. 8.10a). A plausible explanation could be due to a stronger screening effect in the densely packed island (type I) compared to the island type II.

We have explained in chapter 3 that depositing molecules on the thin decoupling layer of MoS$_2$ reduces the line width and enables us to investigate the intrinsic electronic feature such as vibronic states. Here, we resolve the vibronic state of
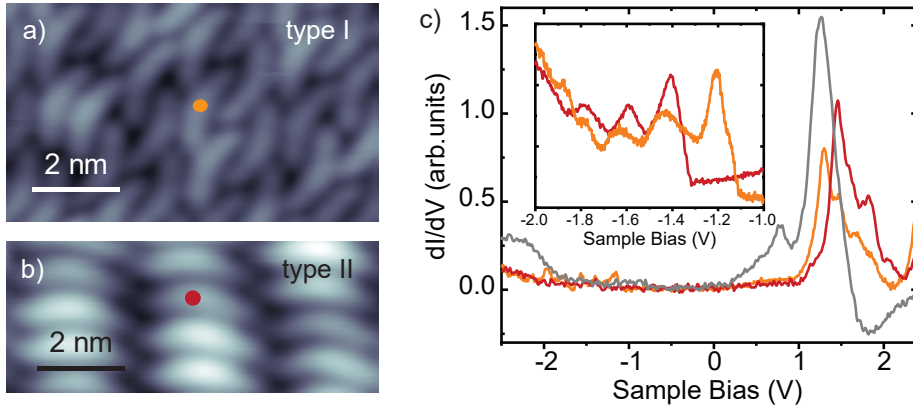
Figure 8.10: **a)** and **b)** STM topography of two types of DCV5T-Me$_2$ molecular islands scanned at 1V, 20 pA. **c)** Constant-height dI/dV spectra measured on the center of two molecules indicated in **a)** and **b)** by red and orange spots corresponding to their spectra. (Feedback opened at 2.5V, 100pA with V$_{mod}$=10 mV). The inset spectra shows the HOMO resonance at -1.2V for type I (orange) and at -1.4V for type II (red), respectively.

charged DCV5T-Me$_2$ as we have done for charged TCNQ and TTF molecules in chapters 6 and 7. Having shown in Fig. 8.9a that the intense resonances of the HOMO appears on the sides of the molecule, STS is measured slightly away from the center of the molecule (blue dot in Fig. 8.11a). Same calculations as explained in chapters 6 and 7 are done here using Franck-Condon model. To simulate the spectrum, a Lorentzian peak with the intensity proportional to the Poisson distribution are applied to each vibronic peak (Fig. 8.11b - lower panel). We note that there is good agreement in Fig. 8.11b between the simulated and the experimental spectra. We also considered the voltage drop of $\sim$ 10% [19, 77] in the bias voltage compared to the energy axis due to the voltage drop in SL-MoS$_2$. We observe few vibrational modes with (Huang-Rhys factor) S$_k$>0.01 which are more dominant (intense) than the other modes in the spectrum. The first three modes with the low energies of 2meV, 8meV, 12meV are not resolvable individually with our energy resolution (30meV). Consequently, they contribute to an asymmetric line shape for the first resonance. We resolve the other modes at energies from 155meV to 180meV with non negligible Huang-Rhys factors. Eventually, with the last modes, we can attribute the peak at -1.4V (described in the previous section) to the vibronic state.

8.3 C$_{60}$ on MoS$_2$/Ag(111): Structural and Electronic Properties

8.3.1 Structural Properties

C$_{60}$ fullerenes were extensively studied on various surfaces by STM. Evaporation at room temperature (RT), results in closed-packed hexagonal molecular islands on metal [13, 61, 66, 189–192] due to the spherical nature of molecule whereby the substrate may influence the orientation of the molecules within the island. On MoS$_2$, only by lowering the sample temperature, fullerenes are trapped on the MoS$_2$/Ag(111) surface. Here, we evaporate C$_{60}$ on the cold sample temperature at 110 K. Fig. 8.12a depicts an overview STM image where molecules mostly stick to Ag(111) and only a small fraction is found on MoS$_2$. The C$_{60}$ molecules easily diffuse on the surface even at low temperature and they appear as single molecules or small clusters on MoS$_2$ (Fig. 8.12a and b).

On metal surfaces there are some preferable orientations regarding the surface crystal structure, but on MoS$_2$ the dependence of the orientation of the molecules to the moiré pattern is not known yet. This orientation can be resolved when scanned at sufficiently large positive bias where we observe the particular symmetry of the
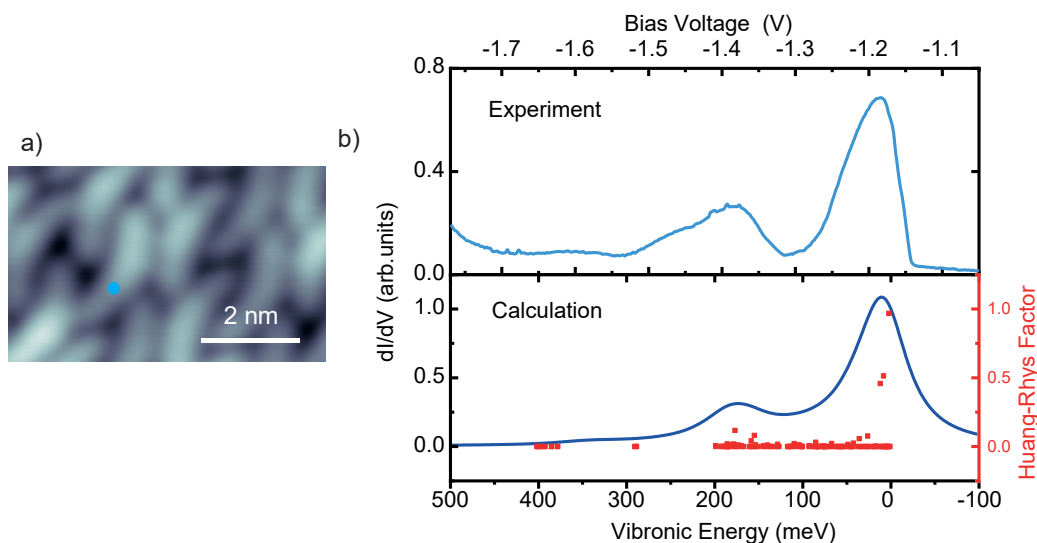
Figure 8.11: **a)** STM topography of a DCV5T-Me$_2$ island recorded at V = 1V, I = 20 pA. **b)** Simulated (bottom panel) and experimental (top panel) dI/dV spectra at the position indicated by the blue dot in **a)** with feedback opened at V = -1V, I = 100 pA, with Vmod = 5mV. The simulated spectrum is obtained from DFT calculations for all the vibrational mode of the DCV5T-Me$_2^+$ molecule with a Huang-Rhys factor higher than 0.01 (red dots associated with the right axis). A Lorentzian peak of 30 meV broadening is applied to all of these modes.

LUMO of the C$_{60}$ [61]. The orientations can be compared to the calculated orbital shapes from former works [193, 194]. At positive sample bias, three different patterns can be distinguished in Fig. 8.13.

In order to detect the various orientations better, Fig. 8.13b depicts the current signal associated to the topography image of Fig. 8.13a. The molecules appear either as one uniform lobe with a dim center (red arrow), with twofold (blue arrow) symmetry or threefold (green arrow) symmetry. Fig. 8.13c (left panel) shows the molecular structure of C$_{60}$ in which the topmost feature is a pentagon ring, a C-C bond and a hexagon, respectively (indicated by red, blue and green frames correspond to the arrows). On the right panel, Fig. 8.13c depicts the calculations of isosurfaces of the squared LUMO of a free C$_{60}$ [194]. Similar features were observed for C$_{60}$ on Ag(110) [194], Au(111)[66, 192], Ag(111)[190] and Cu(110) [13].

8.3.2 Electronic Properties

Due to the high mobility of the C$_{60}$ on the weakly interacting MoS$_2$ layer, spectroscopy on single molecules cannot be recorded in a reproducible manner. For this reason, we focus our study on C$_{60}$ molecules that form small clusters on MoS$_2$/Ag(111).

In order to investigate if the HOMO and LUMO energies are protected by the MoS$_2$ band gap, and to inspect the influence of neighbouring molecules, we acquire conductance spectra on a small molecular assembly depicted in Fig. 8.14a. STS measurements (Fig. 8.14b) are performed on six molecules in the island. We observe that the LUMO resonances vary from 1.0V to 1.45V and the HOMO resonances vary from -2.1V to -2.43V for different molecules. We also observe two other resonances at positive bias in each spectrum which can be attributed either to vibronic states or to additional resonances due to the lifting of the degeneracy of the LUMO. Due to C$_{60}$

Figure 8.12: **a)** Overview STM image of C$_{60}$ molecules on MoS$_2$ and on Ag(111) deposited at 110 K sample temperature, scanned at V=2 V, I=30 pA. **b)** STM image of C$_{60}$ molecules on MoS$_2$/Ag(111) scanned at V=2 V, I=30 pA. **c)** High resolution STM image of C$_{60}$ where molecules take different orientation on MoS$_2$/Ag(111) scanned at V=2 V, I=30 pA. To see the spherical C$_{60}$, here we use a contract in which MoS$_2$ appeared dark.
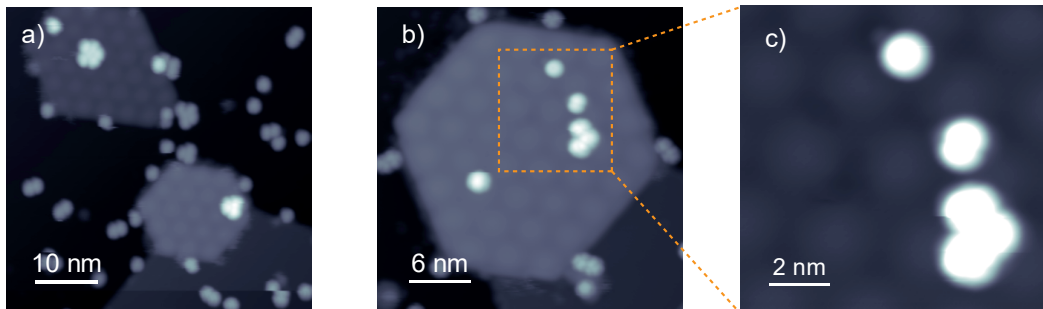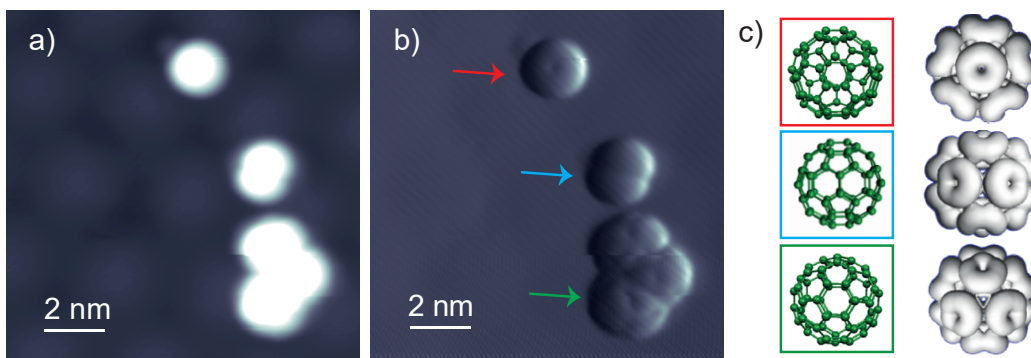
Figure 8.13: **a)** STM image of C_{60} molecules on MoS_2/Ag(111) deposited at 110 K sample temperature, scanned at V=2 V, I=30 pA. **b)** Current signal associated to the topography in **a)** showing different molecular orientations. **c)** Molecular structure of C_{60} of three high-symmetry orientations: top view a pentagon (top panel) a hexagon (middle panel) and a C-C bond (lower panel). Calculated isosurfaces of constant density of states for the LUMO orbital of a free C_{60} molecule. The lobes correspond to the DOS accumulation on the pentagonal faces of the C_{60} cage [194].

symmetry, molecular orbitals are largely degenerate and resolvable via spectroscopic techniques. HOMO and LUMO have degeneracies of 5 and 3, respectively. The variation in HOMO and LUMO resonances, consequently results in the variation of HOMO-LUMO gap from 3.30V to 3.75V. We have several hypotheses to explain this variation; it can be due to the orientation of each C_{60} molecule, however we do not have enough data to evaluate this hypothesis. Molecular orientations are visible in the current signal (Fig. 8.14c) associated to the topographic image. Similar to other molecules on MoS_2 surface, one explanation can be MoS_2 moiré pattern. Conductance spectroscopy in chapter 5, revealed the shifts of the onsets of ~50 mV and ~130 mV on the top and hollow sites away and toward Fermi level at negative and positive bias, respectively. Another explanation could be due to the different screening effect when the number of neighbouring molecules are different. In chapter 3, we have explained that the screening mechanism due to the polarizability of the neighbouring molecules in the molecular island reduces the Coulomb energy and thus the HOMO-LUMO gap size. Here, in Fig. 8.14a the molecule in the center (dotted as violet) which is surrounded by six molecules has the smaller HOMO-LUMO gap of 3.30V. This effect was also seen in C_{60} molecule on Au(111) in former work [66], when the HOMO-LUMO gap of single molecule was found larger than molecule in the molecular island.

The HOMO-LUMO gap is measured 2.4 eV for C_{60} on Au(111) which is smaller than the gap on MoS_2 and can be assigned to the strong screening effect by the metal surface [66].
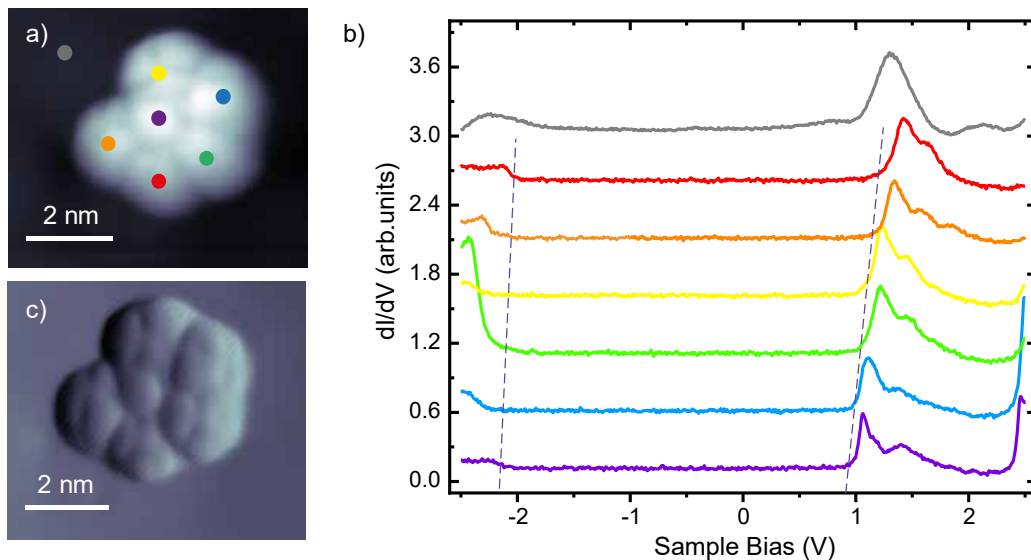
Figure 8.14: Electronic properties of C$_{60}$ molecular island. **a)** STM image of C$_{60}$ molecules on MoS$_2$ with different molecular orientations scanned at V=1 V, I=30 pA. **b)** dI/dV spectra acquired at the centre of C$_{60}$ molecules indicated in **a)** (set point: 30pA, 2.5V with V$_{mod}$ =10 mV). **c)** Current signal associated to the topography image **a)**.

8.4 DCV5T-Me$_2$/C$_{60}$ on MoS$_2$/Ag(111): Structural and Electronic Properties

The energy level alignments of DCVnTs compared with C$_{60}$ obtained from electro-chemical measurements [179] is shown in Fig. 8.15. The energy diagram shows that the HOMO energy of DCVnTs increases with the increase of the number of central thiophene rings whereas the energy of the LUMO is slightly modified because of the electron-withdrawing DCV end groups [182]. The low-lying HOMO energy of the DCV5T compound is beneficial for a high open-circuit voltage (V$_{OC}$) in planar heterojuction solar cells that use C$_{60}$ as an acceptor, because the V$_{OC}$ depends on the difference between the HOMO level of the donor and the LUMO level of the acceptor [178].

We have discussed the structural and electronic properties of DCV5T-Me$_2$ and C$_{60}$ molecules deposited on MoS$_2$/Ag(111). Similar to the growth procedure of DCV5T-Me$_2$ and C$_{60}$ in the previous sections, here we first deposit DCV5T-Me$_2$ at 200 K, then we post anneal the sample at RT, subsequently we deposit C$_{60}$ at 200 K. We obtain self-assembled ordered islands of DCV5T-Me$_2$ and small islands of C$_{60}$ as shown in Fig. 8.16a. We notice there is no mixing of the two types of molecules, but we observe a common interface between two islands. We note that on Ag(111) substrate, there are also no ordered structures of both molecules (see Fig. 8.16b).
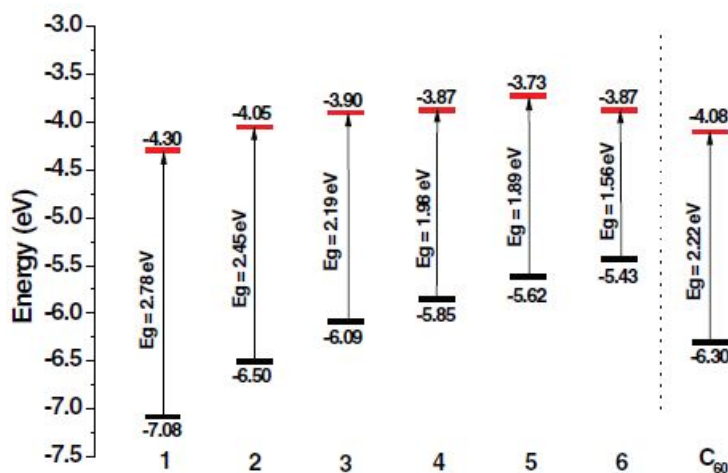
Figure 8.15: Representation of HOMO/LUMO energies of DCVnTs (n:1-6) derived from electrochemical data and compared to HOMO/LUMO energy levels of C$_{60}$. Red lines represent the LUMO and black the HOMO level. The HOMO energy of DCVnTs increases with the number of central thiophene rings while the energy of the LUMO is slightly modified. Image taken from [179].

Co-depositing of these molecules on Au(111) also does not form mixed structures in former work [195].

To understand the non-mixing behavior, we need to consider the possible intermolecular interactions. Between DCV5T-Me$_2$ molecules in the self-assembled islands, we discussed about the formation of hydrogen bonds. Between C$_{60}$, the intermolecular interaction are dominated by π-π interaction (π-stacking). Now, between the C$_{60}$ and the DCV5T-Me$_2$ adsorbed on a surface, neither H-bonding (because of chemical nature of C$_{60}$) nor π-stacking (because the planar configuration of DCV5T-Me$_2$ vs the 3D nature of C$_{60}$) are possible. Therefore, the only possible intermolecular interaction between C$_{60}$ and DCV5T-Me$_2$ are van der Waals forces which are generally not as strong as π-stacking and H-bond.

At some spots on the interface, C$_{60}$ molecules locate on top of DCV5T-Me$_2$ molecules. Fig. 8.17a shows an STM image of DCV5T-Me$_2$ and C$_{60}$ molecular assemblies on MoS$_2$/Ag(111). In Fig. 8.17b, we observe the apparent height of 6Å (the orange line in Fig. 8.17a), whereas in Fig. 8.17c, the initiation of the line profile implies the apparent height of 8Å (see the red line in Fig. 8.17a). This indicates that there is a second layer of C$_{60}$ molecule on top of DCV5T-Me$_2$ molecule. To inspect the electronic properties, we record spectroscopic measurement on single layer C$_{60}$ (C$_{60}$/MoS$_2$) and on second layer C$_{60}$ (C$_{60}$/ DCV5T-Me$_2$/MoS$_2$) shown in Fig. 8.17d. The LUMO resonance for single layer C$_{60}$ is located at 0.9V (orange spectrum) whereas on second layer C$_{60}$ the LUMO resonance is at 1.3V. This shift can imply the good decoupling of the C$_{60}$ on DCV5T-Me$_2$ on MoS$_2$ from the metal surface compared to C$_{60}$ on MoS$_2$. We also note that, here the LUMO energy of C$_{60}$ at the
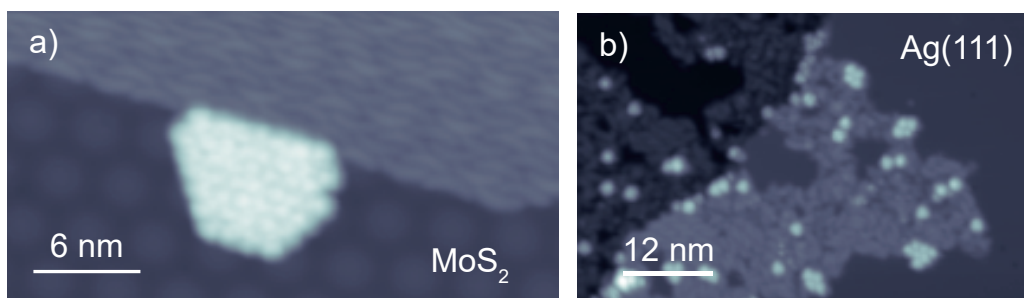
Figure 8.16: **a)** STM image of DCV5T-Me$_2$ and C$_{60}$ on MoS$_2$/Ag(111) recorded at V = 1V, I = 20 pA, Both species organize in ordered molecular islands and eventually form an interface. **b)** STM image of DCV5T-Me$_2$ and C$_{60}$ on Ag(111) recorded at V = 1V, I = 20 pA, DCV5T-Me$_2$ and C$_{60}$ arranged in disordered islands. In both images the preparation is the same, first DCV5T-Me$_2$ is deposited at 200K and post annealed at RT, then C$_{60}$ is deposited at 200 K.

interface is lower in energy than the case of C$_{60}$ within the island which we have studied in the previous section. One possible explanation is the interaction between the acceptor C$_{60}$ and donor DCV5T-Me$_2$ in the form of charge transfer. However, as we did not find HOMO in the considered energy range, we cannot disentangle between screening or charge transfer effect as the origin on the shift of the LUMO.

8.5 Conclusion

In this chapter, DCV5T-Me$_2$ and C$_{60}$ molecules were deposited on MoS$_2$/Ag(111) and investigated separately. On MoS$_2$, DCV5T-Me$_2$ deposited at 200 K formed small disordered islands where molecules took various configurations within the island. Post annealing led to the formation of two types of ordered islands, where the molecules adopt the same bent configuration. Using STS, we resolved the HOMO and the LUMO of the molecule within the islands. In the small disordered island the HOMO and the LUMO resonances vary due to different environment. In the large and ordered island, the HOMO-LUMO gap was found 300 mV larger in the island with less packed structure. The smaller gap size in the densely packed island was attributed to the larger screening effect. Within the Franck–Condon model, we resolved vibronic states of DCV5T-Me$_2$ molecules adsorbed on MoS$_2$/Ag(111). This confirms that the SL-MoS$_2$ is a promising decoupling layer on Ag(111) like Au(111).

Evaporating C$_{60}$ molecules on a cold sample resulted in the formation of small clusters on MoS$_2$, where C$_{60}$ molecules appeared in different orientations. As C$_{60}$ on MoS$_2$ was mobile, we studied them in the islands. Spectroscopy in the molecular island showed the variation in the HOMO-LUMO gap size. The molecule with more neighbours shows smaller gap as a consequence of the higher screening effect.
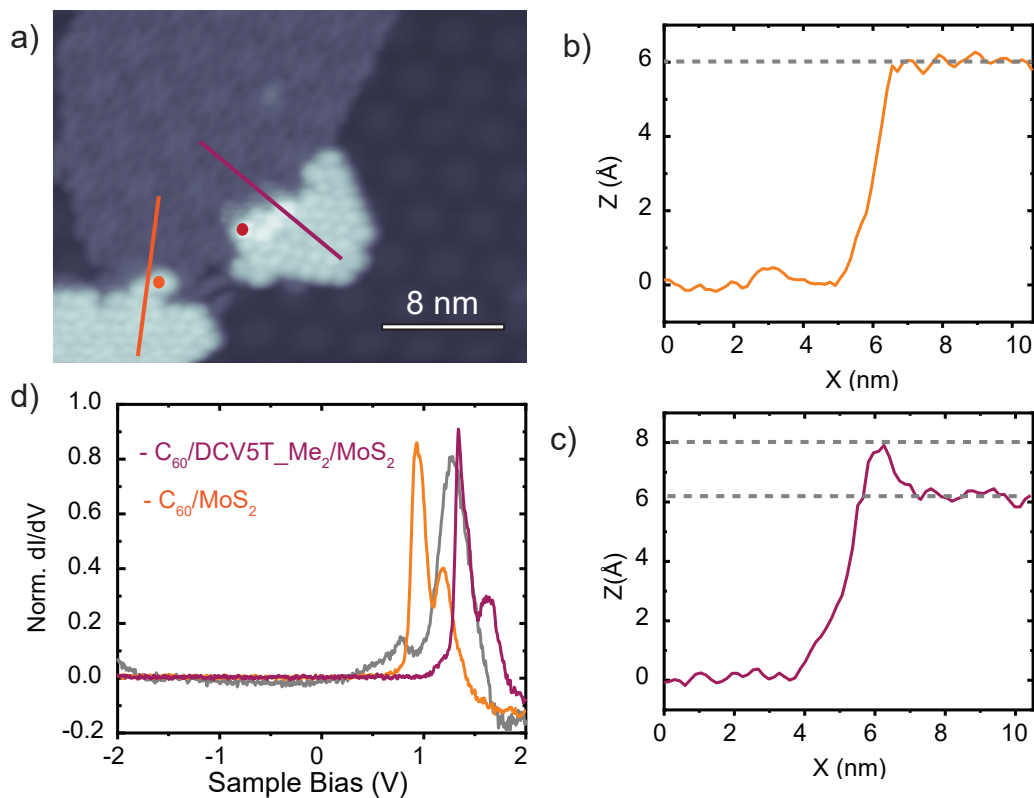
Figure 8.17: **a)** STM image of DCV5T-Me$_2$ and C$_{60}$ on MoS$_2$/Ag(111) recorded at 1V, 20 pA, **b)** and **c)** Line profile along a monolayer C$_{60}$ (orange line) and along a double layer C$_{60}$ on DCV5T-Me$_2$ (red line). **d)** Spectroscopy on C$_{60}$ on monolayer (orange dot) and on double layer C$_{60}$ (red dot) feedback opened at 2V, 100pA with V$_{mod}$=10 mV.

Following the growth procedure of DCV5T-Me$_2$ and C$_{60}$, we grew both molecules on the MoS$_2$ surface which led to the formation of homo-molecular islands. At the interface, some C$_{60}$ lay on DCV5T-Me$_2$ and show a shift away from Fermi level.

Summary and Outlook

In this thesis, we have investigated structural and electronic properties of organic molecular assemblies on single-layer molybdenum disulfide (SL-MoS$_2$) on Ag(111) surface, using combined STM/STS measurements. We have used SL-MoS$_2$ as a decoupling layer to characterize adsorbates on Ag(111) surface. The SL-MoS$_2$ reduces the hybridization and screening effects and facilitates investigating of the intrinsic electronic properties.

First, we investigated the structural and electronic properties of SL-MoS$_2$ on the Ag(111) surface. We observed a smaller band gap than the band gap of free-standing MoS$_2$ as a consequence of hybridization with the underlying metal substrate. Moreover, SL-MoS$_2$ displays a moiré pattern due to the lattice mismatch between MoS$_2$ and the Ag surface. SL-MoS$_2$ on Au(111) and Ag(111) exhibit very similar gap structure. However, we found the bandgap was down-shifted in energy probably due to the lower work function of Ag compared to Au.

In the next part, we have exploited SL-MoS$_2$ as a decoupling layer to investigate the intrinsic electronic properties of tetracyanoquinodimethane (TCNQ) molecules. We found self-assembled molecular islands, which were stabilized by CN-HC bonds between the cyano endgroups and the quinone center of neighboring molecules. We have identified the resonances derived from the highest occupied molecular orbital (HOMO) and lowest unoccupied molecular orbital (LUMO). The LUMO resonance lies at the conduction band onset of MoS$_2$, whereas the HOMO lies within the valence band. We have found a rather narrow width for the LUMO resonance which was significantly smaller than the observed resonance on a metal surface where hybridization is much stronger as compared to the MoS$_2$ layer. Furthermore, due to the decoupling properties of SL-MoS$_2$, TCNQ also exhibited a vibronic fingerprint, which was in good agreement with DFT calculations and Franck-Condon based excitations.

We did similar investigation to characterize electronic properties of tetrathiafulvalene (TTF) molecules. We identified the HOMO resonance of the pure TTF molecular island on MoS$_2$/Ag(111) and the vibronic states using Franck-Condon model. We also investigated charge transfer (CT) processes in the charge transfer complex (CTC) composed of TTF and TCNQ. In the CTC of TTF-TCNQ, STS revealed two states

close to the Fermi level at both bias polarities which were not seen in the pure TTF and pure TCNQ assemblies. We have assigned these states to the singly occupied molecular orbital (SOMO) and singly unoccupied molecular orbital (SUMO) of both TCNQ and TTF, due to CT between the donor (TTF) and the acceptor (TCNQ). Another charge transfer process can be induced by gating by the STM tip when the molecule has a state near Fermi level. This charging event was detected in our STS result as sharp peaks.

In the last part of this thesis, we have investigated the adsorption of methyl-substituted dicyanovinyl (DCV5T-Me$_2$) and C$_{60}$ on MoS$_2$/Ag(111) individually and also at their interface. These are prototype electron acceptor C$_{60}$ and donor (DCV5T-Me$_2$) molecules in organic solar cell. The adsorption of DCV5T-Me$_2$ leads to the formation of small assemblies of molecules or single molecules at low temperature. Within the assembly, molecules appeared in various conformations due to the rotation of DCV end groups and thiophene rings around their C-C bonds. Post annealing leads to the formation of two kinds of self-assembled islands. Although in both islands the molecular conformation is the same, they have different bonding with the surrounding molecules. Type I is stabilized via CN-HC bonds as well as S-N bonds, whereas in type II, one molecule is in contact with neighboring molecules via only CN-HC bonds interactions. Spectroscopy has shown smaller HOMO-LUMO gap in type I molecular arrangements compared to type II, which we ascribe to different screening. Depositing C$_{60}$ on SL-MoS$_2$/Ag(111) lead to the formation of small clusters with diverse orientations of C$_{60}$ molecules. STS on C$_{60}$ revealed a change in the HOMO-LUMO gap as the numbers and the orientation of molecular neighbors vary. Depositing both DCV5T-Me$_2$ and C$_{60}$, the molecules do not form mixed structures but individual islands. In rare cases we found C$_{60}$ molecules on top of DCV5T-Me$_2$ molecules. These molecules exhibited an up-shift of the LUMO state because the underlying DCV5T-Me$_2$ molecules weaken the interactions with the surface. This explanation however, cannot be disentangled from the partial charge transfer between the donor and the acceptor molecules.

To conclude, this work demonstrates that SL-MoS$_2$ on Ag(111) is a good decoupling layer. It provides insight into electronic characteristics (conductance and vibronics) of self-assembled organic molecules as well as fundamental mechanisms of CT in the CTCs. This can be seen as an efficient way to fabricate molecular-size electronic devices.

As an outlook, atomic force microscopy (AFM) studies on TTF-TCNQ can give better insight into the molecular arrangements in the mixed structure to find whether the orientation of molecules with respect to each other affects the electronic properties. To understand deeper the CT processes between donor-acceptor molecules, knowing molecular orientations helps to know precisely how they interact. Moreover, having good control of surface temperature during deposition of DCV5T-Me$_2$ and C$_{60}$ may result in the formation of mixed structure that could exhibit CT properties. However,

our experimental results are in agreement with previously findings on the same donor-acceptor molecular assemblies on Au(111) [195]. Therefore, in order to achieve CTC with C_{60}, we propose co-deposition of non-planar molecules [66, 196].

Bibliography

[1]   G. E. Moore et al. "Cramming more components onto integrated circuits." In: *Electronics* 38.8 (1965) (cit. on p. 1).

[2]   A. Aviram and M. A. Ratner. "Molecular rectifiers." In: *Chemical Physics Letters* 29.2 (1974), pp. 277–283 (cit. on p. 1).

[3]   O. Y. Kim and J. Y. Lee. "High efficiency deep blue phosphorescent organic light-emitting diodes using a tetraphenylsilane based phosphine oxide host material." In: *Journal of Industrial and Engineering Chemistry* 18.3 (2012), pp. 1029–1032 (cit. on p. 1).

[4]   S. Engmann et al. "Higher order effects in organic LEDs with sub-bandgap turn-on." In: *Nature Communications* 10.1 (2019), pp. 1–10 (cit. on p. 1).

[5]   W. Yang et al. "Simultaneous enhanced efficiency and thermal stability in organic solar cells from a polymer acceptor additive." In: *Nature Communications* 11.1 (2020), pp. 1–10 (cit. on p. 1).

[6]   Y. Huo, H.-L. Zhang, and X. Zhan. "Nonfullerene all-small-molecule organic solar cells." In: *ACS Energy Letters* 4.6 (2019), pp. 1241–1250 (cit. on p. 1).

[7]   N. Wang et al. "Functionalized organic thin film transistors for biosensing." In: *Accounts of Chemical Research* 52.2 (2019), pp. 277–287 (cit. on p. 1).

[8]   J.-M. Kim et al. "A flexible pentacene thin film transistors as disposable DNA hybridization sensor." In: *Journal of Industrial and Engineering Chemistry* 18.5 (2012), pp. 1642–1646 (cit. on p. 1).

[9]   R. Fitzner et al. "Correlation of π-conjugated oligomer structure with film morphology and organic solar cell performance." In: *Journal of the American Chemical Society* 134.27 (2012), pp. 11064–11067 (cit. on p. 1).

[10]   M. A. Green et al. "Solar cell efficiency tables (Version 55)." In: *Progress in Photovoltaics: Research and Applications* 28.1 (2020), pp. 3–15 (cit. on p. 1).

[11]   J.-L. Brédas et al. "Molecular understanding of organic solar cells: the challenges." In: *Accounts of Chemical Research* 42.11 (2009), pp. 1691–1699 (cit. on pp. 1, 20, 47).

[12]   K. Walzer et al. "Highly efficient organic devices based on electrically doped transport layers." In: *Chemical Reviews* 107.4 (2007), pp. 1233–1271 (cit. on pp. 1, 20, 47).

[13]   G. Schulze et al. "Resonant electron heating and molecular phonon cooling in single C_{60} junctions." In: *Physical Review Letters* 100.13 (2008), p. 136801 (cit. on pp. 1, 75, 76).

[14]   A. Pecchia, G. Romano, and A. Di Carlo. "Theory of heat dissipation in molecular electronics." In: *Physical Review B* 75.3 (2007), p. 035401 (cit. on p. 1).

[15]   D. R. Ward et al. "Vibrational and electronic heating in nanoscale junctions." In: *Nature Nanotechnology* 6.1 (2011), pp. 33–38 (cit. on p. 1).

[16]   N. Néel et al. "Controlled contact to a C_{60} molecule." In: *Physical Review Letters* 98.6 (2007), p. 065502 (cit. on p. 1).

[17]   F. Pump et al. "Quantum transport through STM-lifted single PTCDA molecules." In: *Applied Physics A* 93.2 (2008), pp. 335–343 (cit. on p. 1).

[18]   X. qiu, G. Nazin, and W. Ho. "Vibronic states in single molecule electron transport." In: *Physical Review Letters* 92.20 (2004), p. 206102 (cit. on pp. 1, 2, 17, 43).

[19]   N. Krane et al. "High-Resolution Vibronic Spectra of Molecules on Molybdenum Disulfide Allow for Rotamer Identification." In: *ACS Nano* 12.11 (2018), pp. 11698–11703 (cit. on pp. 1, 2, 19, 22, 29, 32, 35, 39, 42, 45, 49, 59, 63, 64, 70, 74).

[20]   G. Meyer. "A simple low-temperature ultrahigh-vacuum scanning tunneling microscope capable of atomic manipulation." In: *Review of Scientific Instruments* 67.8 (1996), pp. 2960–2965 (cit. on pp. 1, 12).

[21]   D. M. Eigler, C. Lutz, and W. Rudge. "An atomic switch realized with the scanning tunnelling microscope." In: *Nature* 352.6336 (1991), pp. 600–603 (cit. on p. 1).

[22]   X. Lu et al. "Charge transfer and screening in individual C_{60} molecules on metal substrates: A scanning tunneling spectroscopy and theoretical study." In: *Physical Review B* 70.11 (2004), p. 115418 (cit. on pp. 2, 15).

[23]   K. S. Thygesen and A. Rubio. "Renormalization of molecular quasiparticle levels at metal-molecule interfaces: Trends across binding regimes." In: *Physical Review Letters* 102.4 (2009), p. 046802 (cit. on p. 2).

[24]   S. Braun, W. R. Salaneck, and M. Fahlman. "Energy-level alignment at organic/metal and organic/organic interfaces." In: *Advanced Materials* 21.14-15 (2009), pp. 1450–1472 (cit. on p. 2).

[25]   F. Tautz. "Structure and bonding of large aromatic molecules on noble metal surfaces: The example of PTCDA." In: *Progress in Surface Science* 82.9-12 (2007), pp. 479–520 (cit. on p. 2).

[26]   I. F. Torrente, K. J. Franke, and J. I. Pascual. "Structure and electronic configuration of tetracyanoquinodimethane layers on a Au (1 1 1) surface." In: *International Journal of Mass Spectrometry* 277.1-3 (2008), pp. 269–273 (cit. on pp. 2, 35, 36, 38, 40, 42).

[27]   S. Wickenburg et al. "Tuning charge and correlation effects for a single molecule on a graphene device." In: *Nature Communications* 7.1 (2016), pp. 1–7 (cit. on pp. 2, 17, 25, 43).

[28]   A. Riss et al. "Imaging and tuning molecular levels at the surface of a gated graphene device." In: *ACS Nano* 8.6 (2014), pp. 5395–5401 (cit. on pp. 2, 17, 25).

[29]   M. Sterrer et al. "Control of the charge state of metal atoms on thin MgO films." In: *Physical Review Letters* 98.9 (2007), p. 096107 (cit. on p. 2).

[30]   F. Donati et al. "Magnetic remanence in single atoms." In: *Science* 352.6283 (2016), pp. 318–321 (cit. on p. 2).

[31]   C. Brülke et al. "Quantitative analysis of the electronic decoupling of an organic semiconductor molecule at a metal interface by a monolayer of hexagonal boron nitride." In: *Physical Review B* 99.12 (2019), p. 121404 (cit. on p. 2).

[32]   S. Koslowski et al. "Adsorption and electronic properties of pentacene on thin dielectric decoupling layers." In: *Beilstein Journal of Nanotechnology* 8.1 (2017), pp. 1388–1395 (cit. on p. 2).

[33]   J. Repp et al. "Molecules on insulating films: scanning-tunneling microscopy imaging of individual molecular orbitals." In: *Physical Review Letters* 94.2 (2005), p. 026803 (cit. on pp. 2, 17, 25).

[34]   G. Binnig et al. "Tunneling through a controllable vacuum gap." In: *Applied Physics Letters* 40.2 (1982), pp. 178–180 (cit. on p. 5).

[35]   G. Binnig et al. "Surface studies by scanning tunneling microscopy." In: *Physical Review Letters* 49.1 (1982), p. 57 (cit. on p. 5).

[36]   G. Binnig et al. "7× 7 reconstruction on Si(111) resolved in real space." In: *Physical Review Letters* 50.2 (1983), p. 120 (cit. on p. 5).

[37]   M. Bode. "Spin-polarized scanning tunnelling microscopy." In: *Reports on Progress in Physics* 66.4 (2003), p. 523 (cit. on pp. 5, 15).

[38]   R. Berndt et al. "Photon emission at molecular resolution induced by a scanning tunneling microscope." In: *Science* 262.5138 (1993), pp. 1425–1427 (cit. on p. 5).

[39]   B. Stipe, M. Rezaei, and W. Ho. "Single-molecule vibrational spectroscopy and microscopy." In: *Science* 280.5370 (1998), pp. 1732–1735 (cit. on p. 5).

[40]   M. F. Crommie, C. P. Lutz, and D. M. Eigler. "Confinement of electrons to quantum corrals on a metal surface." In: *Science* 262.5131 (1993), pp. 218–220 (cit. on p. 5).

[41]   D. M. Eigler and E. K. Schweizer. "Positioning single atoms with a scanning tunnelling microscope." In: *Nature* 344.6266 (1990), pp. 524–526 (cit. on p. 5).

[42]   P. K. Hansma and J. Tersoff. "Scanning tunneling microscopy." In: *Journal of Applied Physics* 61.2 (1987), R1–R24 (cit. on p. 6).

[43]   J. Bardeen. "Tunnelling from a many-particle point of view." In: *Physical Review Letters* 6.2 (1961), p. 57 (cit. on pp. 8, 9, 41, 71).

[44]   J. Tersoff and D. Hamann. "Theory and application for the scanning tunneling microscope." In: *Physical Review Letters* 50.25 (1983), p. 1998 (cit. on pp. 8, 11).

[45]   N. Lang. "Spectroscopy of single atoms in the scanning tunneling microscope." In: *Physical Review B* 34.8 (1986), p. 5947 (cit. on p. 10).

[46]   Y. Hasegawa and P. Avouris. "Direct observation of standing wave formation at surface steps using scanning tunneling spectroscopy." In: *Physical Review Letters* 71.7 (1993), p. 1071 (cit. on p. 11).

[47]   R. A. Gaussian09. "M. J. Frisch, G. W. Trucks, H. B. Schlegel, G. E. Scuseria, M. A. Robb, J. R. Cheeseman, G. Scalmani, V. Barone, G. A. Petersson, H. Nakatsuji, X. Li, M. Caricato, A. Marenich, J. Bloino, B. G. Janesko, R. Gomperts, B. Mennucci, H. P. Hratchian, J. V. Ortiz, A. F. Izmaylov, and et al." In: *Inc., Wallingford CT* 121 (2009), pp. 150–166 (cit. on pp. 11, 22, 40, 71).

[48]   C. Lotze. "Fundamental Processes in Single Molecule Junctions: Interplay of Forces and Electronic Effects." PhD thesis. 2014 (cit. on p. 12).

[49]   K. Besocke. "An easily operable scanning tunneling microscope." In: *Surface Science* 181.1-2 (1987), pp. 145–153 (cit. on p. 13).

[50]   J. Frohn et al. "Coarse tip distance adjustment and positioner for a scanning tunneling microscope." In: *Review of Scientific Instruments* 60.6 (1989), pp. 1200–1201 (cit. on p. 13).

[51]   M. Ruby. "SpectraFox: a free open-source data management and analysis tool for scanning probe microscopy and spectroscopy." In: *SoftwareX* 5 (2016), pp. 31–36 (cit. on p. 13).

[52]   I. Horcas et al. "WSXM: a software for scanning probe microscopy and a tool for nanotechnology." In: *Review of Scientific Instruments* 78.1 (2007), p. 013705 (cit. on p. 13).

[53]   L.-g. Liu and W. A. Bassett. "Compression of Ag and phase transformation of NaCl." In: *Journal of Applied Physics* 44.4 (1973), pp. 1475–1479 (cit. on p. 14).

[54]   R. Musket et al. "Preparation of atomically clean surfaces of selected elements: A review." In: *Applications of Surface Science* 10.2 (1982), pp. 143–207 (cit. on p. 14).

[55] B. Voigtländer. *Scanning probe microscopy: Atomic force microscopy and scanning tunneling microscopy*. Springer, 2015 (cit. on p. 14).

[56] L. Limot et al. "Surface-state localization at adatoms." In: *Physical Review Letters* 94.3 (2005), p. 036805 (cit. on p. 14).

[57] J. Li, W.-D. Schneider, and R. Berndt. "Local density of states from spectroscopic scanning-tunneling-microscope images: Ag(111)." In: *Physical Review B* 56.12 (1997), p. 7656 (cit. on p. 14).

[58] B. Doppagne et al. "Electrofluorochromism at the single-molecule level." In: *Science* 361.6399 (2018), pp. 251–255 (cit. on p. 15).

[59] H. Imada et al. "Single-molecule investigation of energy dynamics in a coupled plasmon-exciton system." In: *Physical Review Letters* 119.1 (2017), p. 013901 (cit. on p. 15).

[60] R. Wiesendanger et al. "Recent advances in scanning tunneling microscopy involving magnetic probes and samples." In: *Applied Physics A* 53.5 (1991), pp. 349–355 (cit. on p. 15).

[61] K. J. Franke and J. I. Pascual. "Effects of electron–vibration coupling in transport through single molecules." In: *Journal of Physics: Condensed Matter* 24.39 (2012), p. 394002 (cit. on pp. 15, 75, 76).

[62] A. Mehler et al. "Exciting vibrons in both frontier orbitals of a single hydrocarbon molecule on graphene." In: *Journal of Physics: Condensed Matter* 31.6 (2018), p. 065001 (cit. on pp. 15, 43).

[63] I. Fernández-Torrente et al. "Gating the charge state of single molecules by local electric fields." In: *Physical Review Letters* 108.3 (2012), p. 036801 (cit. on pp. 15, 18, 19, 57).

[64] R. Hesper, L. Tjeng, and G. Sawatzky. "Strongly reduced band gap in a correlated insulator in close proximity to a metal." In: *EPL (Europhysics Letters)* 40.2 (1997), p. 177 (cit. on p. 16).

[65] J. B. Neaton, M. S. Hybertsen, and S. G. Louie. "Renormalization of molecular electronic levels at metal-molecule interfaces." In: *Physical Review Letters* 97.21 (2006), p. 216405 (cit. on p. 16).

[66] I. F. Torrente, K. J. Franke, and J. I. Pascual. "Spectroscopy of C_{60} single molecules: the role of screening on energy level alignment." In: *Journal of Physics: Condensed Matter* 20.18 (2008), p. 184001 (cit. on pp. 16, 70, 75–77, 85).

[67] F. Schulz et al. "Templated self-assembly and local doping of molecules on epitaxial hexagonal boron nitride." In: *ACS Nano* 7.12 (2013), pp. 11121–11128 (cit. on pp. 17, 25, 43).

[68] S. Wang et al. "Vibronic state assisted resonant transport in molecules strongly anchored at an electrode." In: *Physical Review B* 83.11 (2011), p. 115431 (cit. on p. 17).

[69] N. Pavliček et al. "Symmetry dependence of vibration-assisted tunneling." In: *Physical Review Letters* 110.13 (2013), p. 136101 (cit. on p. 17).

[70] G. Nazin, S. Wu, and W. Ho. "Tunneling rates in electron transport through double-barrier molecular junctions in a scanning tunneling microscope." In: *Proceedings of the National Academy of Sciences* 102.25 (2005), pp. 8832–8837 (cit. on pp. 17, 43).

[71] J. Repp et al. "Scanning tunneling spectroscopy of Cl vacancies in NaCl films: strong electron-phonon coupling in double-barrier tunneling junctions." In: *Physical Review Letters* 95.22 (2005), p. 225503 (cit. on pp. 17, 22, 27, 36, 43).

[72] G. Mikaelian et al. "Atomic scale control of single molecule charging." In: *American Institute of Physics* (2006) (cit. on pp. 18, 19, 57).

[73] N. A. Pradhan et al. "Atomic scale conductance induced by single impurity charging." In: *Physical Review Letters* 94.7 (2005), p. 076801 (cit. on p. 19).

[74] K. Teichmann et al. "Controlled charge switching on a single donor with a scanning tunneling microscope." In: *Physical Review Letters* 101.7 (2008), p. 076103 (cit. on p. 19).

[75] L. Liu et al. "Interplay between energy-level position and charging effect of manganese phthalocyanines on an atomically thin insulator." In: *ACS Nano* 9.10 (2015), pp. 10125–10132 (cit. on p. 19).

[76] M. S. Mohammed et al. "Electronic decoupling of polyacenes from the underlying metal substrate by sp 3 carbon atoms." In: *Communications Physics* 3.1 (2020), pp. 1–8 (cit. on p. 19).

[77] N. Krane et al. "Mapping the perturbation potential of metallic and dipolar tips in tunneling spectroscopy on MoS_2." In: *Physical Review B* 100.3 (2019), p. 035410 (cit. on pp. 19, 45, 49, 59, 74).

[78] B. J. Cafferty et al. "Storage of information using small organic molecules." In: *ACS Central Science* 5.5 (2019), pp. 911–916 (cit. on p. 20).

[79] L. Zhou et al. "Recent advances of flexible data storage devices based on organic nanoscaled materials." In: *Nano.Micro.Small* 14.10 (2018), p. 1703126 (cit. on p. 20).

[80] J. Bernede. "Organic photovoltaic cells: history, principle and techniques." In: *Journal of the Chilean Chemical Society* 53.3 (2008), pp. 1549–1564 (cit. on p. 20).

[81] Y. Cui et al. "Single-junction organic photovoltaic cells with approaching 18% efficiency." In: *Advanced Materials* 32.19 (2020), p. 1908205 (cit. on p. 20).

[82] N. Toyota, M. Lang, and J. Müller. *Low-dimensional molecular metals.* Vol. 154. Springer Science Business Media, 2007 (cit. on p. 20).

[83] R. S. Mulliken. "Molecular compounds and their spectra. II." In: *Journal of the American Chemical Society* 74.3 (1952), pp. 811–824 (cit. on p. 20).

[84] J. Franck and E. Dymond. "Elementary processes of photochemical reactions." In: *Transactions of the Faraday Society* 21.February (1926), pp. 536–542 (cit. on p. 20).

[85] E. Condon. "A theory of intensity distribution in band systems." In: *Physical Review* 28.6 (1926), p. 1182 (cit. on p. 20).

[86] N. Krane. "Investigation and Utilization ofMolybdenumDisulfideas Decoupling Layer on Au(111)." PhD thesis. Freie University Berlin, 2019 (cit. on p. 21).

[87] J. Gadzuk. "Inelastic resonance scattering, tunneling, and desorption." In: *Physical Review B* 44.24 (1991), p. 13466 (cit. on pp. 22, 43).

[88] G. Reecht et al. "Vibrational excitation mechanism in tunneling spectroscopy beyond the Franck-Condon model." In: *Physical Review Letters* 124.11 (2020), p. 116804 (cit. on pp. 22, 29, 41, 42, 45).

[89] N. Podberezskaya et al. "Crystal chemistry of dichalcogenides MX_2." In: *Journal of Structural Chemistry* 42.4 (2001), pp. 654–681 (cit. on p. 23).

[90] D. Jariwala et al. "Emerging device applications for semiconducting two-dimensional transition metal dichalcogenides." In: *ACS Nano* 8.2 (2014), pp. 1102–1120 (cit. on pp. 23, 24).

[91] J. A. Wilson and A. Yoffe. "The transition metal dichalcogenides discussion and interpretation of the observed optical, electrical and structural properties." In: *Advances in Physics* 18.73 (1969), pp. 193–335 (cit. on p. 23).

[92] D. Yang et al. "Structure of single-molecular-layer MoS_2." In: *Physical Review B* 43.14 (1991), p. 12053 (cit. on pp. 23, 24).

[93] K. Kam and B. Parkinson. "Detailed photocurrent spectroscopy of the semiconducting group VI transition metal dichalcogenides." In: *The Journal of Physical Chemistry* 86.4 (1982), pp. 463–467 (cit. on p. 24).

[94] V. Sorkin et al. "Nanoscale transition metal dichalcogenides: structures, properties, and applications." In: *Critical Reviews in Solid State and Materials Sciences* 39.5 (2014), pp. 319–367 (cit. on p. 24).

[95] S. G. Sørensen et al. "Structure and electronic properties of in situ synthesized single-layer MoS_2 on a gold surface." In: *ACS Nano* 8.7 (2014), pp. 6788–6796 (cit. on pp. 24, 30, 31).

[96] A. Splendiani et al. "Emerging photoluminescence in monolayer MoS_2." In: *Nano Letters* 10.4 (2010), pp. 1271–1275 (cit. on pp. 25, 26, 33).

[97] T. Li and G. Galli. "Electronic properties of MoS_2 nanoparticles." In: *The Journal of Physical Chemistry C* 111.44 (2007), pp. 16192–16196 (cit. on p. 25).

[98] B. Radisavljevic et al. "Single-layer MoS_2 transistors." In: *Nature Nanotechnology* 6.3 (2011), p. 147 (cit. on p. 25).

[99]   K. F. Mak et al. "Atomically thin MoS_2: a new direct-gap semiconductor." In: *Physical Review Letters* 105.13 (2010), p. 136805 (cit. on pp. 25, 33).

[100]   R. Neville and B. Evans. "The Band Edge Excitons in 2H-MoS_2." In: *Physica Status Solidi (b)* 73.2 (1976), pp. 597–606 (cit. on p. 25).

[101]   T. Cheiwchanchamnangij and W. R. Lambrecht. "Quasiparticle band structure calculation of monolayer, bilayer, and bulk MoS_2." In: *Physical Review B* 85.20 (2012), p. 205302 (cit. on pp. 25, 32).

[102]   D. Y. Qiu, H. Felipe, and S. G. Louie. "Optical spectrum of MoS_2: many-body effects and diversity of exciton states." In: *Physical Review Letters* 111.21 (2013), p. 216805 (cit. on pp. 25, 32).

[103]   H.-P. Komsa and A. V. Krasheninnikov. "Effects of confinement and environment on the electronic structure and exciton binding energy of MoS_2 from first principles." In: *Physical Review B* 86.24 (2012), p. 241201 (cit. on p. 25).

[104]   Z. Y. Zhu, Y. C. Cheng, and U. Schwingenschlögl. "Giant spin-orbit-induced spin splitting in two-dimensional transition-metal dichalcogenide semiconductors." In: *Physical Review B* 84.15 (2011), p. 153402 (cit. on pp. 25, 26).

[105]   A. Bruix et al. "Single-layer MoS_2 on Au(111): Band gap renormalization and substrate interaction." In: *Physical Review B* 93.16 (2016), p. 165422 (cit. on pp. 25, 32–34).

[106]   H. Bana et al. "Epitaxial growth of single-orientation high-quality MoS_2 monolayers." In: *2D Materials* 5.3 (2018), p. 035012 (cit. on pp. 25, 26).

[107]   N. Alidoust et al. "Observation of monolayer valence band spin-orbit effect and induced quantum well states in MoX_2." In: *Nature Communications* 5.1 (2014), pp. 1–9 (cit. on p. 26).

[108]   J. Cho et al. "Structural and electronic decoupling of C_{60} from epitaxial graphene on SiC." In: *Nano Letters* 12.6 (2012), pp. 3018–3024 (cit. on p. 25).

[109]   C. Bombis et al. "Single molecular wires connecting metallic and insulating surface areas." In: *Angewandte Chemie International Edition* 48.52 (2009), pp. 9966–9970 (cit. on p. 25).

[110]   C. J. Villagomez et al. "STM images of a large organic molecule adsorbed on a bare metal substrate or on a thin insulating layer: Visualization of HOMO and LUMO." In: *Surface Science* 603.10-12 (2009), pp. 1526–1532 (cit. on p. 25).

[111]   L. Gross et al. "High-resolution molecular orbital imaging using a p-wave STM tip." In: *Physical Review Letters* 107.8 (2011), p. 086101 (cit. on p. 25).

[112]   P. Järvinen et al. "Molecular self-assembly on graphene on SiO2 and h-BN substrates." In: *Nano Letters* 13.7 (2013), pp. 3199–3204 (cit. on p. 25).

[113]   S. Joshi et al. "Control of molecular organization and energy level alignment by an electronically nanopatterned boron nitride template." In: *ACS Nano* 8.1 (2014), pp. 430–442 (cit. on p. 25).

[114] F. D. Natterer, F. Patthey, and H. Brune. "Distinction of nuclear spin states with the scanning tunneling microscope." In: *Physical Review Letters* 111.17 (2013), p. 175303 (cit. on p. 25).

[115] A. Heinrich et al. "Single-atom spin-flip spectroscopy." In: *Science* 306.5695 (2004), pp. 466–469 (cit. on p. 25).

[116] S. Li et al. "Rotational spectromicroscopy: imaging the orbital interaction between molecular hydrogen and an adsorbed molecule." In: *Physical Review Letters* 114.20 (2015), p. 206101 (cit. on p. 25).

[117] N. A. Pradhan, N. Liu, and W. Ho. "Vibronic spectroscopy of single C_{60} molecules and monolayers with the STM." In: *The Journal of Physical Chemistry B* 109.17 (2005), pp. 8513–8518 (cit. on pp. 25, 43).

[118] S. Wu et al. "Control of relative tunneling rates in single molecule bipolar electron transport." In: *Physical Review Letters* 93.23 (2004), p. 236802 (cit. on p. 25).

[119] S. Fatayer et al. "Reorganization energy upon charging a single molecule on an insulator measured by atomic force microscopy." In: *Nature Nanotechnology* 13.5 (2018), pp. 376–380 (cit. on pp. 27, 36).

[120] creativecommons. *licenses.* 2020 (cit. on pp. 29, 35).

[121] D. Kim et al. "Toward the growth of an aligned single-layer MoS_2 film." In: *Langmuir* 27.18 (2011), pp. 11650–11653 (cit. on p. 30).

[122] S. Helveg et al. "Atomic-scale structure of single-layer MoS_2 nanoclusters." In: *Physical Review Letters* 84.5 (2000), p. 951 (cit. on pp. 30, 31).

[123] S. S. Grønborg et al. "Synthesis of epitaxial single-layer MoS_2 on Au(111)." In: *Langmuir* 31.35 (2015), pp. 9700–9706 (cit. on pp. 30, 31).

[124] N. Wakabayashi, H. Smith, and R. Nicklow. "Lattice dynamics of hexagonal MoS_2 studied by neutron scattering." In: *Physical Review B* 12.2 (1975), p. 659 (cit. on p. 31).

[125] K. Bronsema, J. De Boer, and F. Jellinek. "On the structure of molybdenum diselenide and disulfide." In: *Zeitschrift für Anorganische und Allgemeine Chemie* 540.9-10 (1986), pp. 15–17 (cit. on p. 31).

[126] N. Krane, C. Lotze, and K. J. Franke. "Moiré structure of MoS_2 on Au(111): Local structural and electronic properties." In: *Surface Science* 678 (2018), pp. 136–142 (cit. on pp. 32, 33).

[127] N. Krane et al. "Electronic structure and luminescence of quasi-freestanding MoS_2 nanopatches on Au(111)." In: *Nano Letters* 16.8 (2016), pp. 5163–5168 (cit. on p. 32).

[128] M. M. Ugeda et al. "Giant bandgap renormalization and excitonic effects in a monolayer transition metal dichalcogenide semiconductor." In: *Nature Materials* 13.12 (2014), pp. 1091–1095 (cit. on p. 32).

[129]   A. J. Bradley et al. "Probing the role of interlayer coupling and coulomb interactions on electronic structure in few-layer MoSe$_2$ nanostructures." In: *Nano Letters* 15.4 (2015), pp. 2594–2599 (cit. on p. 32).

[130]   J. A. Miwa et al. "Electronic structure of epitaxial single-layer MoS$_2$." In: *Physical Review Letters* 114.4 (2015), p. 046802 (cit. on p. 33).

[131]   C. Zhang et al. "Probing critical point energies of transition metal dichalcogenides: surprising indirect gap of single layer WSe$_2$." In: *Nano Letters* 15.10 (2015), pp. 6494–6500 (cit. on p. 33).

[132]   D. Otálvaro, T. Veening, and G. Brocks. "Self-assembled monolayer induced Au(111) and Ag(111) reconstructions: Work functions and interface dipole formation." In: *The Journal of Physical Chemistry C* 116.14 (2012), pp. 7826–7837 (cit. on p. 34).

[133]   M. Dendzik et al. "Substrate-induced semiconductor-to-metal transition in monolayer WS 2." In: *Physical Review B* 96.23 (2017), p. 235440 (cit. on p. 34).

[134]   M. Rosner et al. "Two-dimensional heterojunctions from nonlocal manipulations of the interactions." In: *Nano Letters* 16.4 (2016), pp. 2322–2327 (cit. on p. 34).

[135]   D. S. Acker and W. R. Hertler. "Substituted quinodimethans. I. Preparation and chemistry of 7, 7, 8, 8-tetracyanoquinodimethan." In: *Journal of the American Chemical Society* 84.17 (1962), pp. 3370–3374 (cit. on p. 35).

[136]   D. Acker et al. "7, 7, 8, 8-Tetracyanoquinodimethane and its electrically conducting anion-radical derivatives." In: *Journal of the American Chemical Society* 82.24 (1960), pp. 6408–6409 (cit. on p. 35).

[137]   A. L. Smith and P. Tan. "Creatine synthesis: An undergraduate organic chemistry laboratory experiment." In: *Journal of Chemical Education* 83.11 (2006), p. 1654 (cit. on p. 35).

[138]   B. Milián et al. "On the electron affinity of TCNQ." In: *Chemical Physics Letters* 391.1-3 (2004), pp. 148–151 (cit. on pp. 35, 42, 47).

[139]   E. Faulques et al. "Determination of charge transfer in molybdenum complexes of 7, 7, 8, 8-tetracyano-p-quinodimethane with vibrational spectroscopy." In: *Spectrochimica Acta Part A: Molecular and Biomolecular Spectroscopy* 51.5 (1995), pp. 805–819 (cit. on pp. 35, 47).

[140]   R. Compton and C. Cooper. "Negative ion properties of tetracyanoquinodimethan: Electron affinity and compound states." In: *The Journal of Chemical Physics* 66.10 (1977), pp. 4325–4329 (cit. on p. 35).

[141]   C. Klots, R. Compton, and V. Raaen. "Electronic and ionic properties of molecular TTF and TCNQ." In: *The Journal of Chemical Physics* 60.3 (1974), pp. 1177–1178 (cit. on pp. 35, 47).

[142] A. Farragher and F. Page. "Experimental determination of electron affinities. Part 11.—Electron capture by some cyanocarbons and related compounds." In: *Transactions of the Faraday Society* 63 (1967), pp. 2369–2378 (cit. on p. 35).

[143] G.-Z. Zhu and L.-S. Wang. "Communication: Vibrationally resolved photo-electron spectroscopy of the tetracyanoquinodimethane (TCNQ) anion and accurate determination of the electron affinity of TCNQ." In: *AIP Publishing LLC* (2015) (cit. on pp. 35, 42).

[144] M. Garnica et al. "Long-range magnetic order in a purely organic 2D layer adsorbed on epitaxial graphene." In: *Nature Physics* 9.6 (2013), p. 368 (cit. on pp. 35, 36, 38, 40).

[145] S. Barja et al. "Self-organization of electron acceptor molecules on graphene." In: *Chemical Communications* 46.43 (2010), pp. 8198–8200 (cit. on pp. 35, 38).

[146] S. Ghosh et al. "Selective control of molecule charge state on graphene using tip-induced electric field and nitrogen doping." In: *npj 2D Materials and Applications* 3.1 (2019), pp. 1–5 (cit. on pp. 35, 38).

[147] C. Park et al. "Weak competing interactions control assembly of strongly bonded TCNQ ionic acceptor molecules on silver surfaces." In: *Physical Review B* 90.12 (2014), p. 125432 (cit. on pp. 35, 38, 42).

[148] T.-C. Tseng et al. "Charge-transfer-induced structural rearrangements at both sides of organic/metal interfaces." In: *Nature Chemistry* 2.5 (2010), p. 374 (cit. on pp. 35, 36, 38).

[149] W. Erley and H. Ibach. "Vibrational spectra of tetracyanoquinodimethane (TCNQ) adsorbed on the Cu(111) surface." In: *Surface Science* 178.1-3 (1986), pp. 565–577 (cit. on p. 35).

[150] M. Capitan et al. "TCNQ grown on Cu(001): its atomic and electronic structure determination." In: *The Journal of Physical Chemistry C* 120.47 (2016), pp. 26889–26898 (cit. on p. 35).

[151] G. Sini, J. S. Sears, and J.-L. Brédas. "Evaluating the performance of DFT functionals in assessing the interaction energy and ground-state charge transfer of donor/acceptor complexes: tetrathiafulvalene- tetracyanoquinodimethane (TTF- TCNQ) as a model case." In: *Journal of Chemical Theory and Computation* 7.3 (2011), pp. 602–609 (cit. on p. 35).

[152] D. Maccariello et al. "Spatially resolved, site-dependent charge transfer and induced magnetic moment in TCNQ adsorbed on graphene." In: *Chemistry of Materials* 26.9 (2014), pp. 2883–2890 (cit. on pp. 36, 40, 42).

[153] H. Zhong et al. "Interfacial properties of monolayer and bilayer MoS_2 contacts with metals: beyond the energy band calculations." In: *Scientific Reports* 6 (2016), p. 21786 (cit. on p. 42).

[154] G. Reecht et al. "π-Radical Formation by Pyrrolic H Abstraction of Phthalocyanine Molecules on Molybdenum Disulfide." In: *ACS Nano* 13.6 (2019), pp. 7031–7035 (cit. on pp. 42, 55).

[155] F. Matino et al. "Electronic decoupling of a cyclophane from a metal surface." In: *Proceedings of the National Academy of Sciences* 108.3 (2011), pp. 961–964 (cit. on p. 43).

[156] T. Frederiksen et al. "Dynamic Jahn-Teller effect in electronic transport through single C_{60} molecules." In: *Physical Review B* 78.23 (2008), p. 233401 (cit. on p. 43).

[157] Q. Huan et al. "Spatial imaging of individual vibronic states in the interior of single molecules." In: *The Journal of Chemical Physics* 135.1 (2011), p. 014705 (cit. on p. 43).

[158] F. Schwarz et al. "Electronic and Vibrational States of Single Tin–Phthalocyanine Molecules in Double Layers on Ag(111)." In: *The Journal of Physical Chemistry C* 119.27 (2015), pp. 15716–15722 (cit. on p. 43).

[159] J. Wu et al. "Preparation of Single-Crystalline Heterojunctions for Organic Electronics." In: *Advanced Materials* 29.14 (2017), p. 1606101 (cit. on p. 47).

[160] T. Oyamada et al. "Switching effect in Cu: TCNQ charge transfer-complex thin films by vacuum codeposition." In: *Applied Physics Letters* 83.6 (2003), pp. 1252–1254 (cit. on p. 47).

[161] A. J. Berlinsky, J. F. Carolan, and L. Weiler. "Photoelectron Spectrum and Electronic Structure of Tetrathiofulvalene (TTF)." In: *Canadian Journal of Chemistry* 52.19 (1974), pp. 3373–3377 (cit. on p. 47).

[162] J. Ferraris et al. "Electron transfer in a new highly conducting donor-acceptor complex." In: *Journal of the American Chemical Society* 95.3 (1973), pp. 948–949 (cit. on p. 47).

[163] M. J. Cohen et al. "Electrical conductivity of tetrathiofulvalinium tetracyanoquinodimethan (TTF)(TCNQ)." In: *Physical Review B* 10.4 (1974), p. 1298 (cit. on p. 47).

[164] M. Sing et al. "Electronic structure of the quasi-one-dimensional organic conductor TTF-TCNQ." In: *Physical Review B* 68.12 (2003), p. 125111 (cit. on p. 47).

[165] D. Jérome. "Organic conductors: From charge density wave TTF- TCNQ to superconducting (TMTSF) 2PF6." In: *Chemical Reviews* 104.11 (2004), pp. 5565–5592 (cit. on p. 47).

[166] T. Ishiguro, K. Yamaji, and G. Saito. "Organic Conductors." In: *Organic Superconductors*. Springer, 1998, pp. 15–43 (cit. on p. 47).

[167] M. Bendikov, F. Wudl, and D. F. Perepichka. "Tetrathiafulvalenes, oligoacenenes, and their buckminsterfullerene derivatives: The brick and mortar of organic electronics." In: *Chemical Reviews* 104.11 (2004), pp. 4891–4946 (cit. on p. 47).

[168]   N. Gonzalez-Lakunza et al. "Formation of dispersive hybrid bands at an organic-metal interface." In: *Physical Review Letters* 100.15 (2008), p. 156805 (cit. on p. 47).

[169]   I. Fernández-Torrente, K. Franke, and J. Pascual. "Vibrational Kondo effect in pure organic charge-transfer assemblies." In: *Physical Review Letters* 101.21 (2008), p. 217203 (cit. on p. 47).

[170]   A. Kumar et al. "Electronic Characterization of a Charge-Transfer Complex Monolayer on Graphene." In: *ACS nano* (2021) (cit. on pp. 50, 55).

[171]   S. Wu, N. Ogawa, and W. Ho. "Atomic-scale coupling of photons to single-molecule junctions." In: *Science* 312.5778 (2006), pp. 1362–1365 (cit. on p. 55).

[172]   T. Nguyen et al. "Coulomb energy determination of a single Si dangling bond." In: *Physical Review Letters* 105.22 (2010), p. 226404 (cit. on p. 55).

[173]   F. Demanze et al. "Tuning of the electronic and optical properties of oligothiophenes via cyano substitution: A joint experimental and theoretical study." In: *The Journal of Physical Chemistry B* 101.23 (1997), pp. 4553–4558 (cit. on p. 63).

[174]   J. Casado et al. "Spectroscopic and Theoretical Study of the Molecular and Electronic Structures of a Terthiophene-Based Quinodimethane." In: *ChemPhysChem* 5.4 (2004), pp. 529–539 (cit. on p. 63).

[175]   K. Schulze et al. "Efficient vacuum-deposited organic solar cells based on a new low-bandgap oligothiophene and fullerene C_{60}." In: *Advanced Materials* 18.21 (2006), pp. 2872–2875 (cit. on p. 63).

[176]   R. Schueppel et al. "Optimizing organic photovoltaics using tailored heterojunctions: A photoinduced absorption study of oligothiophenes with low band gaps." In: *Physical Review B* 77.8 (2008), p. 085311 (cit. on p. 63).

[177]   D. Wynands et al. "Correlation between morphology and performance of low bandgap oligothiophene: C_{60} mixed heterojunctions in organic solar cells." In: *Journal of Applied Physics* 107.1 (2010), p. 014517 (cit. on p. 63).

[178]   A. Mishra et al. "Synthesis and Characterization of Acceptor-Substituted Oligothiophenes for Solar Cell Applications." In: *Advanced Energy Materials* 1.2 (2011), pp. 265–273 (cit. on pp. 63, 78).

[179]   R. Fitzner et al. "Dicyanovinyl–Substituted Oligothiophenes: Structure-Property Relationships and Application in Vacuum-Processed Small Molecule Organic Solar Cells." In: *Advanced Functional Materials* 21.5 (2011), pp. 897–910 (cit. on pp. 63, 65, 78, 79).

[180]   S. Haid et al. "Dicyanovinylene-substituted selenophene–thiophene co-oligomers for small-molecule organic solar cells." In: *Chemistry of Materials* 23.20 (2011), pp. 4435–4444 (cit. on p. 63).

[181] R. Fitzner et al. "Interrelation between Crystal Packing and Small-Molecule Organic Solar Cell Performance." In: *Advanced Materials* 24.5 (2012), pp. 675–680 (cit. on p. 63).

[182] A. Mishra and P. Bäuerle. "Small molecule organic semiconductors on the move: promises for future solar energy technology." In: *Angewandte Chemie International Edition* 51.9 (2012), pp. 2020–2067 (cit. on pp. 63, 78).

[183] G. Reecht et al. "Oligothiophene nanorings as electron resonators for whispering gallery modes." In: *Physical Review Letters* 110.5 (2013), p. 056802 (cit. on p. 64).

[184] T. Ohto et al. "Effects of cis–trans Conformation between Thiophene Rings on Conductance of Oligothiophenes." In: *The Journal of Physical Chemistry Letters* 10.18 (2019), pp. 5292–5296 (cit. on p. 64).

[185] H. Kasai et al. "STM observation of Single Molecular chains of π-conjugated polymers." In: *Chemistry Letters* 31.7 (2002), pp. 696–697 (cit. on p. 64).

[186] E. Orti et al. "Ab Initio Determination of the Geometric Structure and Internal Rotation Potential of 2, 2'-Bithiophene." In: *The Journal of Physical Chemistry* 99.14 (1995), pp. 4955–4963 (cit. on p. 65).

[187] Z. Yang et al. "Orbital redistribution in molecular nanostructures mediated by metal–organic bonds." In: *ACS Nano* 8.10 (2014), pp. 10715–10722 (cit. on p. 67).

[188] L. Bogner et al. "Electronic states and exciton dynamics in dicyanovinyl-sexithiophene on Au(111)." In: *The Journal of Physical Chemistry C* 120.48 (2016), pp. 27268–27275 (cit. on pp. 67, 71).

[189] H. Shin et al. "Structure and dynamics of C_{60} molecules on Au(111)." In: *Physical Review B* 89.24 (2014), p. 245428 (cit. on p. 75).

[190] W. Chen et al. "Orientationally ordered C_{60} on p-sexiphenyl nanostripes on Ag(111)." In: *Acs Nano* 2.4 (2008), pp. 693–698 (cit. on pp. 75, 76).

[191] J. Kollamana et al. "Scanning tunneling microscopy study of ordered C_{60} submonolayer films on Co/Au(111)." In: *The Journal of Physical Chemistry C* 120.14 (2016), pp. 7568–7574 (cit. on p. 75).

[192] G. Schull and R. Berndt. "Orientationally ordered (7×7) superstructure of C_{60} on Au(111)." In: *Physical Review Letters* 99.22 (2007), p. 226105 (cit. on pp. 75, 76).

[193] J. Pascual et al. "Seeing molecular orbitals." In: *Chemical Physics Letters* 321.1-2 (2000), pp. 78–82 (cit. on p. 76).

[194] J. I. Pascual et al. "Vibrational spectroscopy on single C_{60} molecules: the role of molecular orientation." In: *The Journal of Chemical Physics* 117.21 (2002), pp. 9531–9534 (cit. on pp. 76, 77).

[195]   Z. Yang. "Structural and Electronic Properties of Thiophene-based Supramolec-
        ular Architectures on Metal Surfaces: A Combined STM and AFM Study."
        PhD thesis. 2014 (cit. on pp. 79, 85).

[196]   X. Peng et al. "Selective Adsorption of C_{60} in the Supramolecular Nanopat-
        terns of Donor–Acceptor Porphyrin Derivatives." In: *Langmuir* 35.45 (2019),
        pp. 14511–14516 (cit. on p. 85).

Acknowledgments

I would like to express my deepest regards and gratitude towards Prof. Katharina Franke for giving me the opportunity to perform my PhD thesis in her amazing research group, and more importantly for putting her trust in me and my work. I am also grateful to the best postdocs ever, *Chris* and *Gaël*. Thanks Chris, for helping me to be a better physicist in the lab and giving me freedom to follow my ideas. Thanks Gaël, for always making me feel comfortable to bring you new questions, and for all of the constructive and helpful discussions that followed.

Working in a pleasant environment, fueled with happy attitude is a blessing, which I had while working with *Ben, Nils.B, Max, Timo, Nils.K, Idan, Jenny, Eva, Lëaitie, Daniela, Lisa, Gelavizh, Olaf, Rika, Martina, Sergey.* There are many instances of pleasant memories of spending time with my colleagues, let it be reminiscences of the extraordinary 25-year-olds club, coffee and cake clubs, or having lunch together. Although the last year of my work in the group was overshadowed by Corona pandemic which converted most of our communications to virtual webex meetings, the warmth of these memories remain unforgettable.

I would like to thank *Jenny* joon for translating my abstract to German and for proof-reading my thesis. I would also like to express my appreciation to *Rika* joon, who on top of proof-reading my thesis, helped me on multiple occasions with LaTeX.

Along with the all of the pleasant memories which I shared with my colleagues in AG Franke, I should also mention the feeling of support and kindness that I received from my Iranian friends in Berlin. Having the chance of celebrating various Persian ceremonies with you guys, not only was a source of happiness for me, but also made me miss my family much less.

Expressing my appreciation cannot be complete, without mentioning my parents, who gave me their unconditional love, and provided me with the courage and confidence for pursuing my interests. Thank you mom and dad, for your support which reached me even with such a long distance from Arak to Berlin.

When I look back at the first day of arriving to Berlin in February of 2017, I remember not knowing many people in town. Today, after a few years from that winter day of arrival in Berlin, I find it difficult to find the right words which are able to show my appreciation towards all of my friends and colleagues whom I got to know through out my PhD journey.

List of Publications

Publication related to this thesis

1. Asieh Yousofnejad, Gaël Reecht, Nils Krane, Christian Lotze and Katharina J. Franke. *Monolayers of MoS$_2$ on Ag(111) as decoupling layers for organic molecules: resolution of electronic and vibronic states of TCNQ*, Beilstein J. Nanotechnol. 2020, 11, 1062–1071

Publications not related to this thesis

2. Gh. Nabiyouni, D. Ghanbari, A. Yousofnejad, M. Seraj. *A sonochemical-assisted method for synthesis of BaFe$_{12}$O$_{19}$ nanoparticles and hard magnetic nanocomposites Journal of Industrial and Engineering Chemistry*, Journal of Industrial and Engineering Chemistry. 2014, 20, 3425-3429

3. Gh. Nabiyouni, D. Ghanbari, A. Yousofnejad, M. Seraj, Z. Mirdamadian. *Microwave-Assisted Synthesis of CuFe$_2$O$_4$ Nanoparticles and Starch-Based Magnetic Nanocomposites* , Journal of Nanostructures. 2013, 3, 155-160

Selbstständigkeitserklärung

Hiermit erkläre ich die vorliegende Arbeit selbstständig und ohne Zuhilfenahme von nicht angegebenen Quellen angefertigt zu haben. Wörtlich oder sinngemäß übernommene Stellen sind als solche gekennzeichnet. Zudem erkläre ich, dass diese Arbeit in keinem früheren Promotionsverfahren eingereicht und dort angenommen oder für ungenügend befunden wurde.

Berlin, den 31.08.2021

_____

Asieh Yousofnejad